Università degli Studi di Palermo

AREA QUALITÀ, PROGRAMMAZIONE E SUPPORTO STRATEGICO
SETTORE STRATEGIA PER LA RICERCA
U. O. DOTTORATI

Denominazione Dottorato - D072 SCIENZE FISICHE E CHIMICHE
Denominazione del Dipartimento di riferimento - DiFC
Settore Scientifico Disciplinare – CHIM/03 Chimica Generale e Inorganica

Design, synthesis, and characterization of the electronic and atomic structure of materials with prospective application in the thermoelectric technology

IL DOTTORE
Federica Ursi

IL COORDINATORE
Marco Cannas

IL TUTOR
Antonino Martorana

CO-TUTOR
Francesco Giannici

CICLO - XXXV
ANNO CONSEGUIMENTO TITOLO 2022/2023

Index

Index of Figures

Index of Tables

List of symbols and acronyms

TE	Thermoelectric
$\boldsymbol{S}$	Seebeck coefficient
$\Delta \boldsymbol{V}$	Voltage gradient
$\Delta \boldsymbol{T}$	Temperature gradient
$\boldsymbol{Q_c}$	Heat absorbed by the junction in the unit of time
$\boldsymbol{\pi}$	Peltier coefficient
$\boldsymbol{I}$	Current intensity
$\boldsymbol{\Gamma}$	Thomson coefficient
$\boldsymbol{\sigma}$	Electrical conductivity
$\boldsymbol{\kappa}$	Total thermal conductivity
$\boldsymbol{T}$	Absolute temperature
$\boldsymbol{PF}$	Power factor
$\boldsymbol{ZT}$	Figure of merit
$\boldsymbol{\kappa_L}$	Lattice thermal conductivity
$\boldsymbol{\kappa_e}$	Electronic thermal conductivity
$\boldsymbol{k_B}$	Boltzmann constant
$\boldsymbol{n}$	Carrier concentration
$\boldsymbol{\tau}$	Relaxation time
$\boldsymbol{e}$	Effective mass of the carriers
DOS	Density of states
pDOS	Projected density of states
vdW	Van der Waals
TMDC	Transition metal dichalcogenide
$\boldsymbol{f_0(E)}$	Fermi-Dirac distribution
$\boldsymbol{\mu(E)}$	Mobility of carriers
$\boldsymbol{\gamma}$	Degeneracy of band extrema
$\boldsymbol{r}$	Scattering parameter
$\boldsymbol{L}$	Lorenz number
$\boldsymbol{k_B}$	Boltzmann constant

$\boldsymbol{h}$	Planck constant
$\boldsymbol{a}$	Lattice parameter
$\boldsymbol{\theta_D}$	Debye temperature
$\boldsymbol{g}$	Grüneisen parameter
PAW	Projector augmented wave method
USPP	Ultra-Soft Pseudopotential
GGA	Generalized gradient approximations
LDA	Local-density approximations
U	Hubbard parameter
DFT	Density functional theory
XRD	X-ray powder diffraction
TGA	Thermogravimetric studies
µRS	Micro-Raman spectroscopy
SEM	Scanning Electron Microscopy
HA	Hexylamine
ADA	Adamantylamine
VB	Valence band
CB	Conduction band
λ(Å)	X-ray wavelength
d(Å)	Spacing between lattice planes
2θ	angle of diffraction

ABSTRACT

The efficiency of state-of–the-art thermoelectric materials remain nowadays inadequate to compete with conventional power generation and to achieve technological implementation. Attempts at maximizing thermoelectric efficiency include the development of new materials and the optimization of the existing ones with suitable strategies. 2D layered materials currently attract a great deal of interest as promising thermoelectric materials. In the vast range of 2D materials, transition metal dichalcogenides (TMDC) with triple-layer structures have received significant attention due to sizable bandgaps and easy intercalation of organic and inorganic species in the van der Waals (vdW) gap between triple layers to tune the thermoelectric performance.

This thesis is focused on the analysis of the atomic and electronic structure of TMDCs intercalated with inorganic and organic guest moieties. After a general overview on state-of-the-art thermoelectric materials, the second part deals with modification of the electronic structure and the structural disorder induced in TMDCs materials as a consequence of the intercalation with Li, Ca, Ag, and Cu. The third part tackles with the insertion of organic species in the vdW gap of TiS_2. The intercalation of hexylamine (HA) is already described in the literature, but in this thesis the issue of long term stability of the HA-TiS_2 adduct is pursued and deeply investigated with both an experimental and computational approach. As a completely original contribution, the prospective intercalation of TiS_2 with adamantylamine (ADA) is investigated as concerns the atomic and electronic structure. The thermoelectric behaviour of this virtually new hybrid material is simulated and results quite similar to HA-TiS_2, allowing to foresee that the library of hybrid TMDCs for thermoelectric application could be extended to non-linear amines.

PART 1: INTRODUCTION AND GENERAL REMARKS

1. Introduction

1.1 Thermoelectric materials

Humankind is facing a seriously increasing demand for energy. The global need for energy production, storage, management, and distribution is a critical point for modern society. At the same time, the use of fossil fuels as an energy source is causing significant environmental and climatic problems [1,2].

For these reasons, developing renewable, sustainable, green energy sources to replace fossil fuels is one of the most challenging issues in energy research [3–7]. In this perspective, energy harvested from ambient sources and directly converted into electrical energy represents an opportunity for the growth of a distributed power generation network [8–11]. Renewable forms of energy such as sunlight, wind, rain, tides/waves, and geothermal heat have been extensively studied and implemented as alternative energy sources [12–14]. However, despite the recent growth, energy from renewable sources still covers less than a quarter of the world's demand for energy, the reason being mainly related to the high cost of these technologies.

In addition to the conversion of the direct sources, taking advantage of waste power recovery can provide a route for energy saving and improve the overall balance of energy production. Among the possible conversion mechanisms, thermoelectricity encompasses a set of physical phenomena that correlate heat or charge fluxes to temperature gradients or electric fields. A thermoelectric (TE) device can directly convert waste heat into electricity [15–18] using the Seebeck effect or, conversely, can also change electrical energy into thermal energy for cooling or heating using the Peltier effect [19].

In principle, any temperature gradient can be exploited by a TE device to generate electricity, and the design of novel highly efficient TE materials for solid-state energy conversion is currently the focus of worldwide research investigations [20].

Pure TE harvesting systems, collecting heat from natural sources, can generate powers from hundreds of μW to mW. However, considering systems based on waste heat recoveries, like industrial processes, engines, or other human activities, the power scale can reach the order of KW [21].

The main applications of TE devices concern high-power generation, focused on wasted heat recovery at intermediate/high range of temperature, and the low-power implementations, based on small-scale devices [22].

The many benefits of this energy conversion procedure include solid-state operation, no toxic residues, wide scalability, maintenance-free operation versus no moving parts or chemical reactions, and long service life reliability [23].

The empirical evidence of the possibility of obtaining an electrical voltage through the application of a temperature difference dates to Alessandro Volta (1794) [24], although it is customary to credit the discovery of the phenomenon to Thomas Johann Seebeck [25], who independently rediscovered it in 1821. The physical principle in the Seebeck effect is described by the Seebeck coefficient, S, defined as the ratio between the open circuit voltage produced at the ends of the material investigated, and the temperature difference applied to it, as shown in Equation (1).

$$S = \frac{\Delta V}{\Delta T} \tag{1}$$

where ΔV is the voltage generated [V], and ΔT the working temperature gradient [K].

Subsequently, Jean Charles Athanase Peltier [26], in 1834, discovered that, by passing an electric current along a circuit composed of a bimetallic junction, the junction cooled or heated depending on the direction of the current. This effect took the name of the Peltier effect and can be expressed by Equation (2).

$$Q_c = \pi I \tag{2}$$

where Q_c is the heat absorbed by the junction in the unit of time [W], π is the Peltier coefficient [V], and I the current intensity [A].

Finally, William Thomson [27], in 1856, demonstrated the correlation between the Seebeck effect and the Peltier effect. A conductive material can produce or absorb heat from its surroundings when subjected to an electric current and a temperature difference at its ends. This effect is called the Thomson effect, as expressed by Equation (3), where the Thomson coefficient $\Gamma\,[V/\mathrm{K}]$ correlates the Peltier coefficient with the S [28]:

$$\pi = S\Gamma \tag{3}$$

The value of S depends on the character of electric charge carriers and it is negative in the presence of electronic conduction and positive if the majority of carriers are holes. Then, leaving aside metals which, as discussed below, do not provide effective TE materials for energy applications, the useful TE are *p* or *n* semiconductors. The operating mechanism of a TE device is shown in Figure 1.

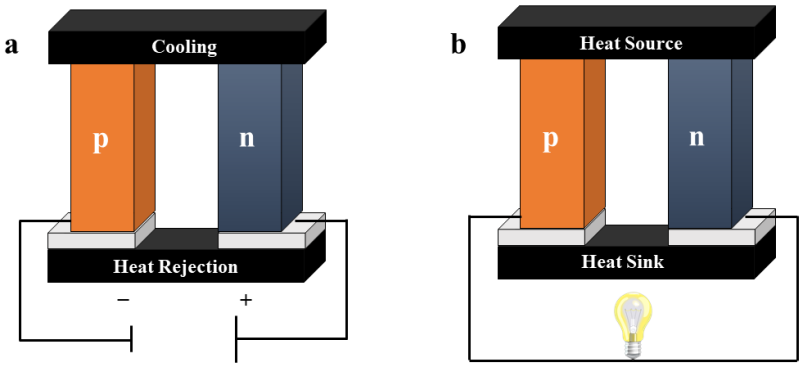

Figure 1. Diagram of a thermoelectric module made of n-type and p-type legs. a) Refrigeration mode; b) Power-generation mode.

The module depicted in Figure 1 is composed of a heat collector, the *p* and *n* legs, and a heat sink, necessary to maintain the thermal gradient in the *p* and *n* materials to prevent uncontrolled heating. A TE device is constituted by several such modules connected electrically in series and thermally in parallel. Both refrigeration and power generation may be accomplished using the same device, as shown in Figure 1.

The temperature gradient applied to the device (Figure 1b) generates, in open circuit condition, a charge carrier density gradient that produces a potential difference,

according to Equation (1). When the *p* and *n* legs are electrically connected, the majority *n* carriers flow into the *p* leg and the holes drift to the *n* leg, giving rise to a net electric current. In the opposite process (Figure 1a), the Peltier heat generated when an electric current is forced through the TE legs by an applied voltage gives rise to a temperature gradient, with heat absorbed on the cold side, transferred through the TE materials, and rejected at the sink [29].

The optimization process for a TE harvester is related to the definition of the conditions for optimal components as well as to the design of a thermal chain that is effective in collecting the heat flux for TE conversion.

The first strategy of device optimization is related to the optimization of the TE materials. Historically, the large-scale implementation of TE materials for energy conversion in commercial applications has been limited due to the low efficiency of converting heat into electricity [18,30]. The efficiency of a TE material is measured by the dimensionless figure of merit ZT, defined by Equation (4).

$$ZT = \frac{S^2\sigma}{\kappa}T \tag{4}$$

where σ is the electrical conductivity, T is the absolute temperature, and κ is the total thermal conductivity. The power factor ($PF = S^2\sigma$) at the numerator characterizes the electron energy conversion capability, while at the denominator κ represents the overall κ, which is the sum of lattice κ_L and electronic thermal conductivity κ_e. Then, an ideal TE material must exhibit high σ, high S, and low κ[31]. However, it is hard to combine all these characteristics in a single material, as the three transport parameters (S, σ, and κ) depend on each other. According to the Drude model [32], the S and the σ, are related to the concentration of charge carriers and to the effective mass by Equations (5) and (6).

$$S = \frac{8\pi k_B^2 T}{3eh^2} m^* \left(\frac{\pi}{3n}\right)^{\frac{3}{2}} \tag{5}$$

$$\sigma = \frac{ne^2\tau}{m^*} \tag{6}$$

where k_B is the Boltzmann constant, n is the concentration of the carriers, τ the relaxation time, and e is the effective mass of the carriers [33]. Figure 2 shows the trend of the transport coefficients as a function of the concentration of the charge carriers. From this plot and Equations (5) and (6), it can be observed that the S is a decreasing function of charge carrier concentration, while σ has, of course, an opposite trend. On the other hand, electric carriers transport also heat, and then we observe a positive slope of κ as a function of carrier concentration. Hence, an optimal ZT is a deal among these contrasting behaviours [34], resulting in a bell-shaped curve of ZT. The maximum of this curve is typically placed at a concentration of about 10^{19} carriers/cm^3, corresponding to heavily doped semiconductors. Insulants and metals are placed on the tails of the ZT curve, so being useless for TE technology.

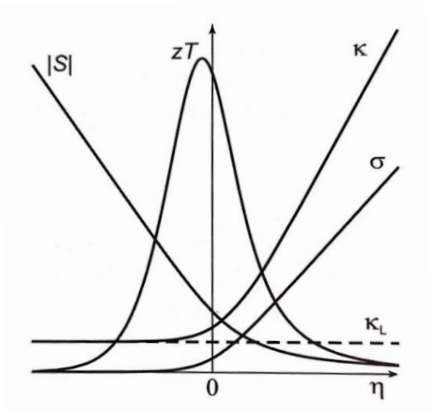

Figure 2. Variation of the transport coefficients as a function of the carrier concentration.

The crucial issues in TE materials research are *i.* how to design materials with a high PF and *ii*. how to improve the TE power of a material without depressing the σ.

The Boltzmann transport theory describes both electronic and thermal transport in most solids [35,36], so allowing to get a general understanding of the thermopower in TE materials. To this concern, the Mott equation, shown in Equation (7), is relevant.

$$S = \frac{\pi^2}{3}\frac{k_B^2 T}{e}\left\{\frac{d\ln\sigma(E)}{dE}\right\}_{E=E_f} \quad (7)$$

It is possible to define the σ as a function of energy with Equation (8).

$$\sigma(E) = D(E)f_0(E)e\mu(E) = n(E)e\mu(E) \quad (8)$$

where

$$n(E) = D(E)f_0(E) \quad (9)$$

$D(E)$, $f_0(E)$, $\mu(E)$, and $n(E)$ are, respectively, the density of state (DOS), the Fermi-Dirac distribution, the mobility of carriers, and the carrier concentration. By comparing Equations (7), (8), and (9), it is possible to see that a high value of the S can be obtained by increasing $\left[\frac{dn(E)}{dE}\right]$, which in turn depends on the local behaviour of $D(E)$.

Figure 3 shows two hypothetical electronic DOS diagrams. One in which the DOS varies rapidly near E_f (Figure 3a), and one in which it does not (Figure 3b). In the general case, the S in the Mott equation is a measure of the variation in $\sigma(E)$ above and below the Fermi surface, specifically through the logarithmic derivative of $\sigma(E)$ with E. Based on Equation 8, the system in Figure 3a with a rapid change of DOS near the Fermi level is expected to have a larger TE power.

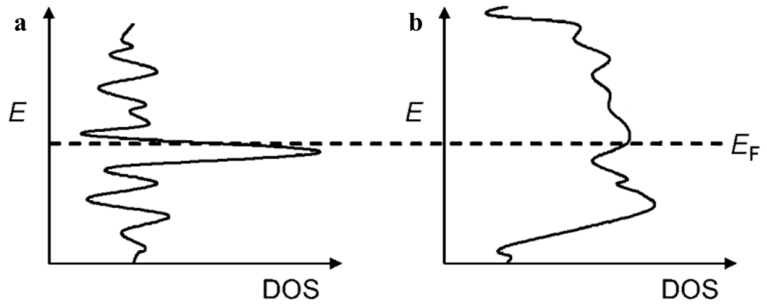

Figure 3. Two hypothetical electronic DOS diagrams.
a) rapid variation of slope near Fermi energy (E_f); b) slow variation of slope near E_f [37].

Another significant equation is the maximum attainable figure of merit, shown in Equation 10.

$$Z_{max} \propto \gamma \frac{T^{3/2}\tau_z \sqrt{\frac{m_x m_y}{m_z}}}{\kappa_L} e^{(r+1/2)} \quad (10)$$

where γ, m_i, τ_z, and r, are the degeneracy of band extrema, the effective mass of the carriers, the relaxation time of the carriers, and the scattering parameter, respectively. In particular, the degeneracy of band extrema (γ) is the number of valleys in the conduction band (*n*-type materials) or peaks in the valence band (*p*-type materials). According to Equation (10), γ needs to be high, because the presence of many such valleys in the band structure could lead to increased ZT. This assumption is reasonable because each band extremum contributes a certain thermopower and σ if occupied by carriers. After all, the total PF for the material derives from the summation of contributions from all extrema.

So, a detailed analysis of the electronic structure of a material can give information about the gap, the degeneracy of the conduction and valence band extrema, and even the effective mass parameters.

As cited above, a further crucial issue in the improvement of TE performance consists in having at the same time a low κ and a high σ. These parameters are correlated by the law of Wiedemann-Franz, shown in Equation (11).

$$\frac{\kappa_e}{\sigma} = LT \quad (11)$$

where L is the Lorenz number ($\sim 2.45 \times 10^{-8}\, W\Omega K^{-2}$) that typically varies moderately for metals and degenerate semiconductors, Equation (11) substantially states that an increase of σ is always matched by a parallel increase of the κ due to electric carriers, no matter of the involved material. So, increasing the σ not only produces an increase in the κ_e but also usually decreases the thermopower; optimizing ZT thus turns out to be a challenge.

An effective way to maximize the ZT is to act on the κ_L, which is related to the transport of thermal energy carried by phonons and is the only parameter not directly determined by the electronic structure.

The κ_L depends on the crystal structure and on the lattice parameters of the material, as shown in Equation (12).

$$\kappa_L = \frac{k_B^3}{h^3}\frac{a^4 \rho \theta_D^3}{g^2 T} \tag{12}$$

where k_B, h, a, θ_D, and g are, respectively, the Boltzmann constant, the Planck constant, the lattice parameter, the material density, the Debye temperature, and the acoustic phonon Grüneisen parameter, which is a measure of the anharmonic nature of lattice vibration. There are two main strategies to achieve low κ_L values, namely the design of materials with low inherent κ and the enhancement of phonon scattering through the control of nano-microstructures [31].

In conclusion, the strategies to be undertaken to increase ZT by acting on κ_L can be many. For example, the use of compounds with complex crystal structures or strong structural anisotropy; the use of heavy atoms; the presence of inclusions, impurities, and defects.

1.2 Strategies for enhancing the performance of thermoelectric

The efficiency of state-of–the-art TE materials remains nowadays inadequate to compete with conventional power generation and in fact, to achieve technological implementation, the novel TE materials should reach efficiencies three times larger than the presently obtained values [38,39].

Attempts at maximizing the PF include the development of new classes of materials and the optimization of existing materials with certain approaches/strategies [40].

The main strategy for optimizing the carrier concentration is doping, such as modulation doping, uniform doping, and gradient doping (Figure 4) [41].

In modulation doping, charge carriers are spatially separated from their parent impurity atoms to reduce the influence of impurity scattering and thereby increase the mobility of the charge carriers [42]. In the case of uniform doping, the carrier concentration is generally independent of temperature, so the best TE performance, cannot be guaranteed in the entire temperature range. One way to deal with this problem is to use gradient doping, for example, taking advantage of the low κ of layered materials in the out-layer direction. The migration of carriers between layers is improved in the out-layer direction by adjusting the symmetry of the crystal structure, thereby promoting electron tunnelling in the inter-layer direction [41,43–45]. However, with prolonged use, the initial carrier concentration gradient in the gradient material may decrease or disappear due to the homogenization effect induced by diffusion, thereby reducing the conversion efficiency. To solve this limitation, using the temperature dependence of the solubility of certain specific dopants and its gradient can be created in a single material [46].

Therefore, for TE material systems with different characteristics, it is important to select an appropriate doping method.

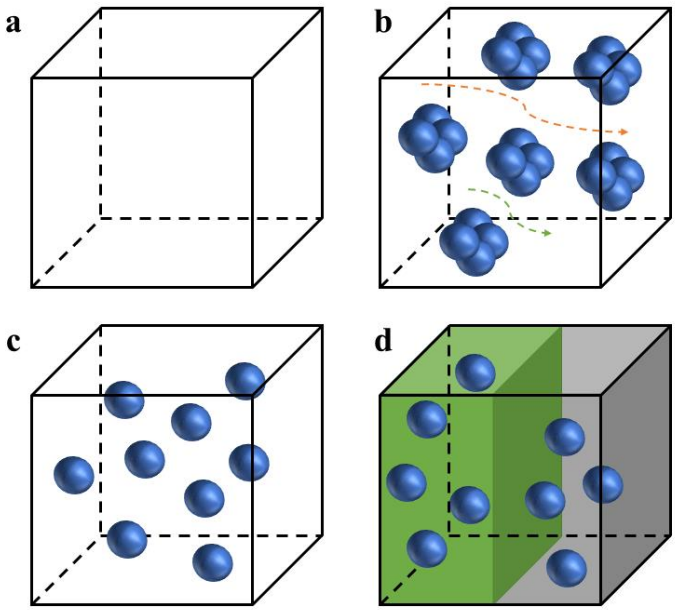

Figure 4 . Schematic diagram of different doping methods.
a) Undoped; b) Modulated doping; c) Uniform doping; d) Gradient doping

Doping elements can enhance the carrier concentration in a TE material by modifying their electronic band structure. Consequently, the DOS is modified as the number of states per energy level is increased. The energy states close to the Fermi level within an order of $k_B T$ can promote electron transport.

Hence, an optimal carrier concentration, a higher S, and a higher ZT, can be obtained for semiconductors and semimetals.

A heavily doped semiconductor exhibits a greater PF than its undoped counterpart [47–53].

Heat in a solid can be transported by different carriers, including phonons, electrons, magnons, etc. In particular, in the case of TE materials, most of the thermal energy is carried by phonons. [54,55].

One strategy for achieving a low κ_L is to strengthen phonon scattering [56]. Introducing lattice point defects into the matrix lattice is an effective way to reduce the κ of the lattice κ_L. In this case, the phonons are more likely to be scattered by point defects rather than electrons, and thus have less impact on carrier mobility.

It is well known that some lattice defects, like vacancies (Figure 5b), interstitials (Figure 5c), and antisite (Figure 5d) defects, are present in materials under various

growth conditions. The presence of these defects in the crystal lattice could affect the electronic and TE properties of materials [57]. Thus, the influence of these defects must be considered when the material properties for various applications are investigated.

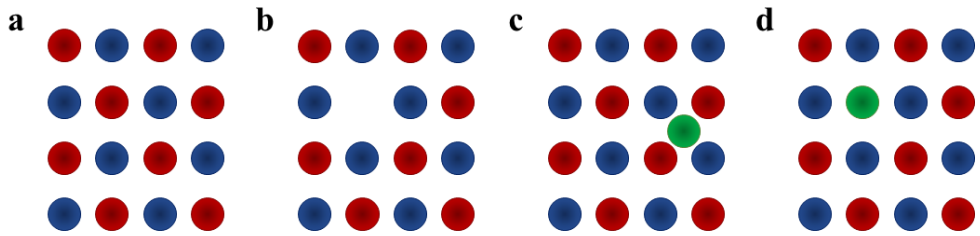

Figure 5. Schematic diagram of lattice point defects.
a) Pure structure, b) Vacancy defect; c) Interstitial defect; d) Antisite defect

Figure 6 shows typical doping methods commonly used in TE materials research. In the case of single doping, the dopant can have the same valence as the regular element, resulting in lattice disorder, or it can be heterovalent, to control the carrier concentration. Cross-substitution, instead, refers to the pair-to-pair substitution of one or more elements from other groups in the periodic table while keeping the total number of valence electrons unchanged [58,59].

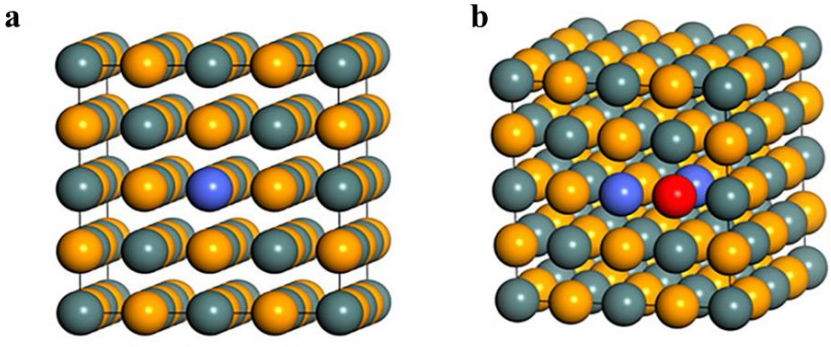

Figure 6. Schematic diagram of typical doping methods.
a) Single doping; b) Cross-substitution [41]

Introducing dislocations, which are typical line defects, is another particularly effective and practical method to reduce κ_L.

Dislocations (Figure 7) and strain fields scatter mid-and high-frequency phonons, so dislocations can effectively reduce the free path of phonons [60,61].

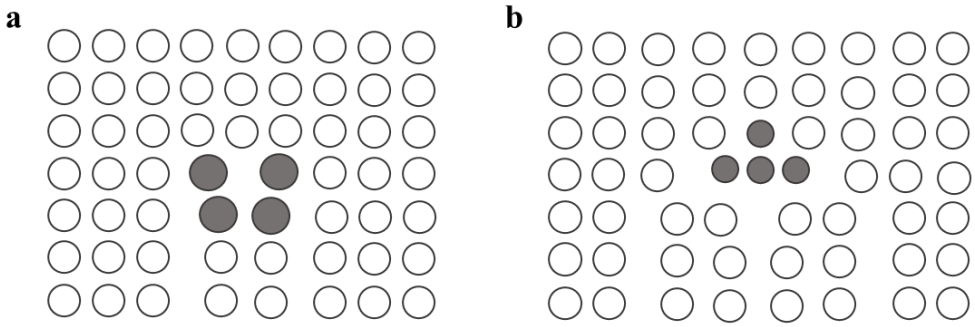

Figure 7. Schematic diagram of dislocation line defects.

Furthermore, in polycrystalline materials, grain boundaries or phase boundaries can effectively scatter low-frequency phonons, and the scattering rate is inversely proportional to the grain size. Therefore, the effective method to scatter long-wavelength phonons is to introduce micro-nano structures.

Dimensionality plays a fundamental role in controlling the properties of materials. A new strategy for designing TE materials by controlling dimensionality was first discussed by Hicks and Dresselhaus [62,63]. Transport properties in micro- and nanostructures differ from that in bulk three-dimensional materials. The κ of nanostructures like super-lattices, composed of nano-metric layers of various elements or substances, is weaker than in bulk materials. This is a positive aspect of TE properties [64,65].

When the dimension of materials decreases and approaches nanometre length scales, it is possible to cause a marked change in the electronic DOS as shown in Figure 8 [66,67].

The origin of the enhancement of TE performance mainly comes from the improved S due to the enhanced electronic DOS.

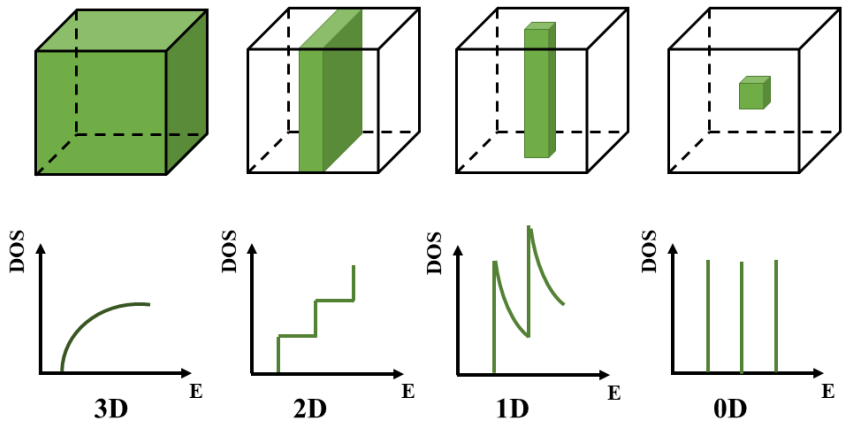

Figure 8. Schematic illustration of the DOS for 3D, 2D, 1D, and 0D materials.

To summarize, in a three-dimensional (3D) material, optimizing all TE parameters together (σ, S, and κ) is a difficult challenge. Instead, in the case of lower dimensions (2D, 1D, and 0D), new possibilities exist to independently adjust them [68]. In addition, new interfaces are created, which can increase the phonon diffusion, leading to an increased value of ZT.

1.3 State of the art

TE materials encompass a broad family of materials, like skutterudites, telluride-based materials (PbTe, Bi_2Te_3, etc.), Si-Ge alloys, Half-Heusler alloys, and clathrates [69,37]. Recently, it has also been shown that some polymers exhibit interesting properties as TE materials.

Figure 9 shows a graphic relating to the materials most used in TE applications [70].

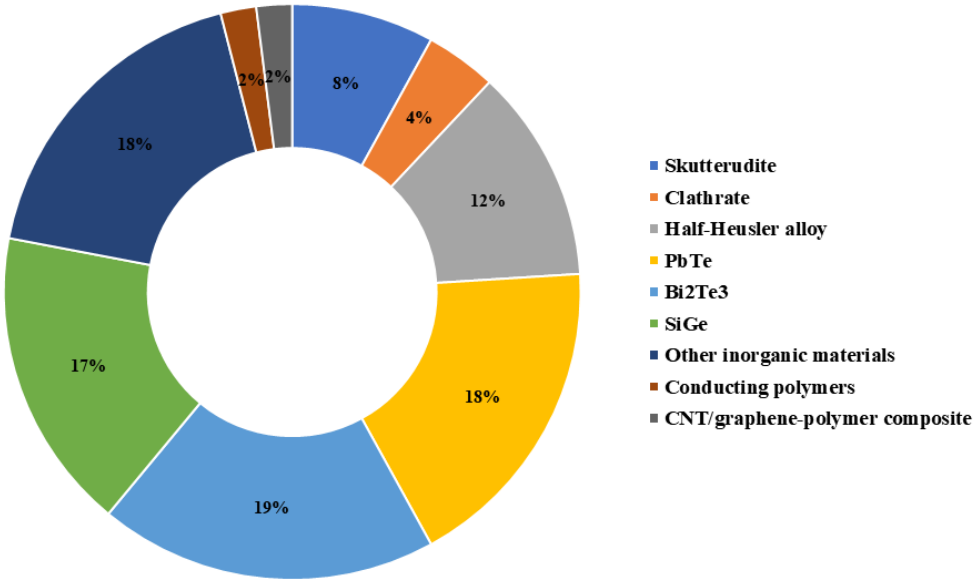

Figure 9. Pie graphic of the different materials used in thermoelectric applications and their percentage contribution.

1.3.1 Skutterudites

The term "skutterudite" refers to the natural mineral $CoAs_3$, which was first discovered in Skutterud, Norway.

Skutterudites are a highly promising and deeply researched class of compounds [71]. They crystallize in the $CoAs_3$-type structure with the cubic space group $Im\bar{3}$, as shown in Figure 10. The general formula is MX_3, where M is a transition metal (Co, Rh, or Ir) and X is a pnicogen element such as P, As, or Si.

The Skutterudites are known for their high electron mobility and the high S. However, they have high κ values.

Among various skutterudites, $CoSb_3$ has received the widest attention as TE material due to its environmentally friendly composition, suitable band gap (0.2 eV), and high carrier mobility. However, the relatively high κ_L (larger than 10 W/mK at room temperature) had become the biggest obstacle to enhancing its TE performance [72–79].

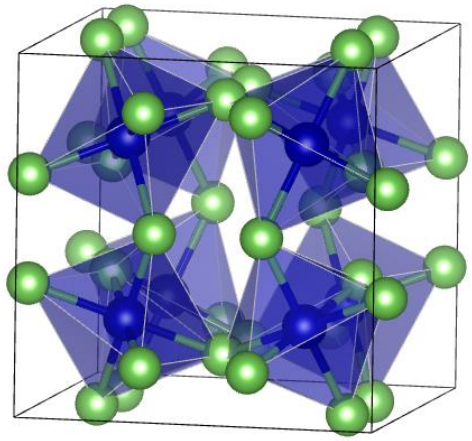

Figure 10. Cubic structure of $CoSb_3$ skutterudite

The insertion of lanthanide, actinide, alkaline earth elements, thallium, or group IV elements into the structure, determines a scattering mechanism of the acoustic phonons within the structure. The smaller and heavier the atom inserted into the lattice, the lower the resulting κ [80]. The investigation of these new skutterudites called filled skutterudites, has led to the observation of large ZT values, such as 1.3 at 800K for $Ba_{0.08}Yb_{0.14}Eu_{0.10}Co_4Sb_{12}$ [81] and 1.7 at 850 K for $Ba_{0.08}La_{0.05}Yb_{0.04}Co_4Sb_{12}$ [82].

1.3.2 Clathrates

"Clathrate" is first used by Powell, coming from the Latin word “Clathratus”, which is the name of a species of compound with a cage structure.

Like skutterudites, inorganic clathrates have a three-dimensional periodic open frame structure. Crystalline clathrates have the distinctive structural motifs of the three-dimensional host frameworks, which contain a variety of polyhedral cages, and encapsulate guest atoms, ions, or molecules. In these structures, encapsulated guests are not connected to their host frameworks by any strong chemical bonds.

There are several ways to classify clathrates. Based on the coordination, this class of compound is subdivided into type I (Figure 11a), type II (Figure 11b), and type III with general formulas A_8E_{46}, $A_{24}E_{136}$, and $A_{30}E_{172}$, respectively, where A = Na, K, or Ba, and E = Al, Ga, In, Si, Ge, or Sn.

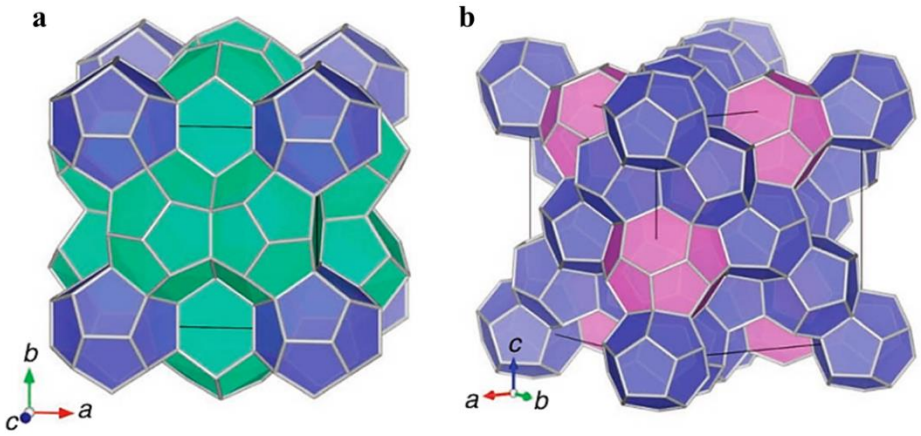

Figure 11. Framework structures of two different type of clathrates.
a) type I clathrate; b) type II clathrate [83]

The characteristic low κ for semiconductor clathrates is attributed to the phonon scattering caused by the guest atoms [84,85]. However, a few studies have investigated clathrate structures, and all have reported $ZT < 1$ [86,87].

1.3.3 Half-Heusler alloy

These compounds were discovered in 1903 by Fritz Heusler. Half-Heusler (HH) alloys constitute the intermetallic class of compounds with potential applications in high-temperature TE devices [88–92]. HH alloys contain a MgAgAs-type cubic structure with three interpenetrating fcc sublattices, each occupied by X, Y, and Z atoms, as shown in Figure 12. Therefore, the general formula is XYZ, where X (Ti, Zr, Hf, V, Mn, or Nb) and Y (Fe, Co, Ni, or Pt) are transition metals and Z (Sn or Sb) is a main-group element [93,94].

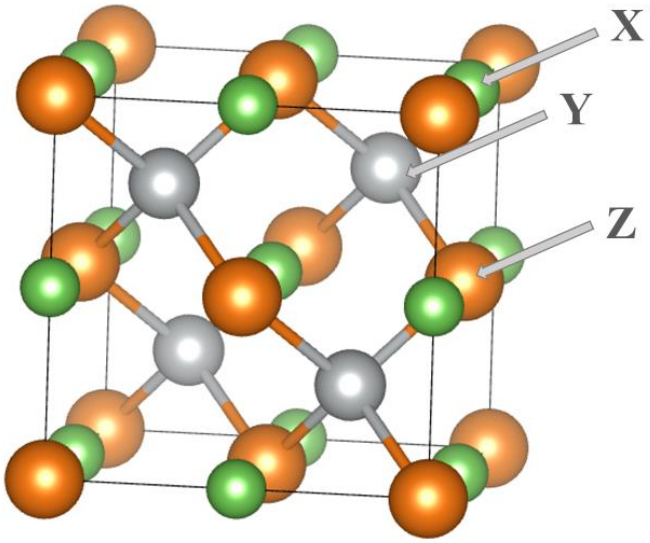

Figure 12. Crystal structure of the Half-Heusler type compounds.

These compounds have a narrow band gap of the order of 0.1-0.2 eV at the Fermi level and have gained the great interest for their potential as TE materials [95]. These materials are associated with large effective masses of lattice vibration associated with several characteristics, including large PF, large S (250 $\mu V/K$), moderate electrical resistivity (1-10 $\mu\Omega m$), and high κ (10 $W/m\ K$) at room temperature [96].

1.3.4 Telluride-based materials

The first materials to be used for TE applications were semiconductors containing heavy metals and, in particular, materials based on tellurium. PbTe (Figure 13a) and Bi_2Te_3 (Figure 13b) are conventional state-of-the-art TE materials that have been used for the past 50 years [97].

Te-based materials exhibit low κ (ca. 2.3 $W/m\,K$ for PbTe and 1.7 $W/m\,K$ for Bi_2Te_3) and a high S of 500 $\mu V/K$ at room temperature.

PbTe is a promising TE material that can efficiently operate at medium temperatures. It crystallizes into the isomorphous cubic NaCl crystal structure with Pb atoms at the cationic sites and Te at the anionic sites. PbTe can be doped either with *n*-type or with *p*-type dopants, causing an increase in the S. Pb-rich PbTe is an *n*-type semiconductor, whereas Te-rich PbTe is a p-type semiconductor [98–102]. Bi_2Te_3 is a low-temperature TE material first proposed in 1954. It crystallizes into a hexahedral-layered structure with five atomic layers Ti(1)-Bi-Te(2)-Bi-Ti(1) stacked by van der Waals (vdW) interaction along the c-axis of the unit cell. Bi_2Te_3 displays unique properties such as a high S (220 $\mu V/K$), good σ (400 S/cm), and low κ (1.5 $W/m\,K$) [103–107].

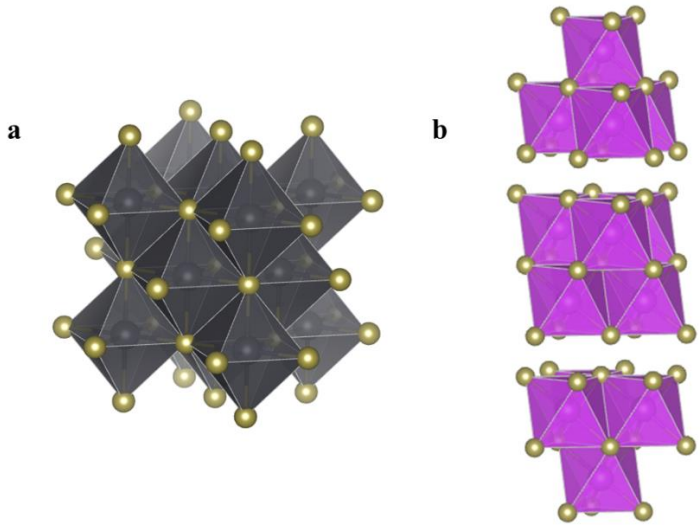

Figure 13. Crystal structure of two materials based on tellurium.
a) PbTe; b) Bi_2Te_3

1.3.5 Metal oxides

An interesting class of compounds for TE applications is constituted by metal oxides [108,109]. Their main advantage as TE materials is their suitability for high-temperature applications. Another advantage is that metals are generally abundant in the earth's crust and cheap.

High values of κ, due to the strong bonding in the metal oxides and the small atomic mass of oxygen are counterbalanced by large carrier mobilities.

It is possible to modify the electrical and κ in metal oxides by doping. By replacing the elements already present with atoms of different sizes but with the same oxidation state (isovalent dopants) it is possible to alter the size of the unit cell and the symmetry of the crystal and lower the κ, while at the same time exerting a limited influence on the σ. On the other hand, by doping with elements of similar size but with different oxidation numbers (aliovalent dopants), it is possible to convert insulating materials into semiconductors, metals and even superconductors [110,111].

1.3.6 Polymers

Conventional TE devices are typically based on inorganic compounds, as they generally show better TE performance and higher stability compared with organic materials [112–117].

However, inorganic semiconductor materials have some disadvantages, including rarity, toxicity, poor processability, a high cost of manufacturing, and cannot be used to collect the waste heat generated at a temperature below 150 degrees.

Among the various categories of TE materials, a great deal of attention has recently been paid to organic TE materials, particularly since the discovery of conducting polymers. In this regard, polymers are very attractive because they are light, flexible, and suitable for room-temperature applications and because they generally require relatively simple manufacturing processes compared to semiconductor-based TE [118–121].

Among the most used polymers, there are Polypyrrole (PPy), Polyaniline (PANI), Polythiophene (PT), Poly(3,4-ethylenedioxythiophene), Polyacetylene (PA), shown in Figure 14, and their derivatives.

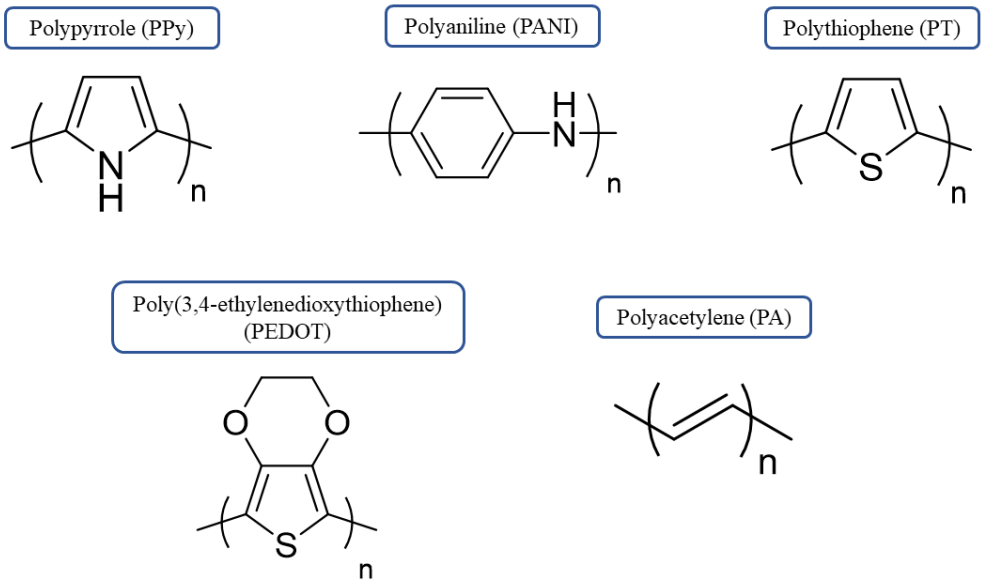

Figure 14. Chemical structures of representative polymers for thermoelectric applications.

1.4 Transition metal dichalcogenides

Despite the vast literature on TE materials, the main drawback of these compounds remains their poor efficiency. However, as mentioned in paragraph 1.2, in the case of lower dimensions (2D, 1D, and 0D), new possibilities exist to optimize all TE parameters [68].

The same chemical compound can exhibit drastically different properties depending on whether it is arranged in a 0D, 1D, 2D, or 3D structure. Although crystalline 0D, 1D, and 3D structures are well studied, 2D hasn't attracted much interest until recently. Since the initial discovery of graphene in 2004, the research interest in these materials has been growing explosively in the last decade's [122–125].

Nanoscale layered 2D materials are emerging for their unique optical [126,127], electronic [128], catalytic [129], and mechanical [130] properties.

In this scenario, the 2D layered materials attract currently a great deal of interest as promising TE materials [131-134]5 In the vast range of 2D materials, transition metal dichalcogenides (TMDC) with lamellar structures similar to that of graphite have received significant attention because some of them are semiconductors with sizable bandgaps [136] and are naturally abundant.

The properties of bulk TMDCs are different, ranging from insulators like HfS_2 to semiconductors like MoS_2 and WS_2, to semimetals like WTe_2 and $TiSe_2$, to real metals like NbS_2 and VSe_2 [136].

The stoichiometry of these materials is MX_2, where M is a central transition metal atom, and X is the chalcogen atom (S, Se, or Te), as shown in Figure 15. These materials are arranged in a sandwich-like structure consisting of covalently bonded X-M-X stacked along the c-direction and weakly stabilized by vdW interaction.

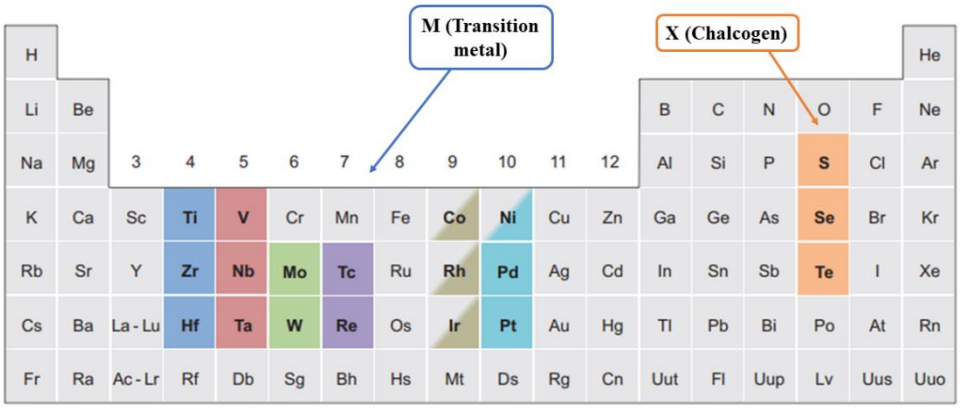

Figure 15. The transition metals (M) and the three chalcogen (X) elements that predominantly crystallize in those layered structures are highlighted in the periodic table [137].

1.4.1 Titanium disulphide

Among the TMDCs, titanium disulphide (TiS_2) has aroused great interest in the field of environmentally friendly TE materials. TiS_2 is a promising candidate as *n*-type TE material due to its advantages including low environmental impact, chemical stability, mechanical stiffness, and the composition of earth-abundant elements Ti and S [138–142].

The unit cell of TiS_2 consists of one atom of Ti and two of S and crystallizes with the 1T type structure of $Cd(OH)_2$ (space group $P\bar{3}m1$) with cell parameters a = b ≠ c. Inside the cell, the Ti coordinates are at (0,0,0), and the two atoms of S a (1/3, 2/3, z) and (2/3, 1/3, -z) with z = 0.25 [143].

TiS_2 is a layered structure consisting of a hexagonally packed layer of metal atoms sandwiched between two layers of chalcogen atoms, as shown in Figure 16. The intralayer M-X bonds are predominantly covalent, which contributes to the low resistivity and high S. On the contrary, the sandwich layers interact through weak vdW forces, which guarantees a low κ [144].

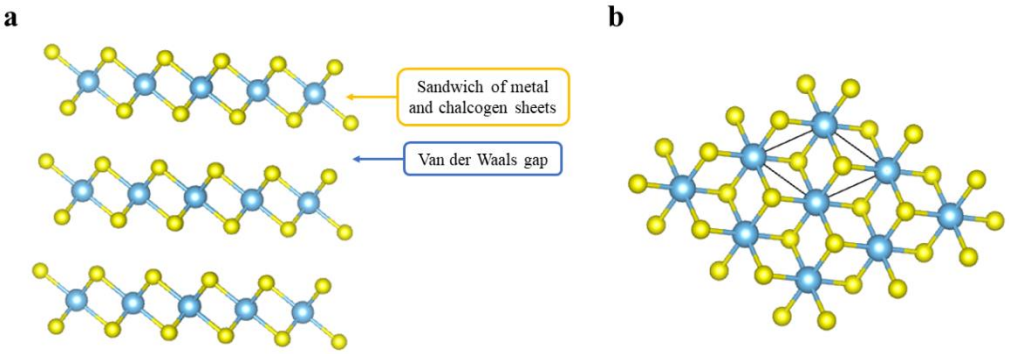

Figure 16. Crystal structure of $P\bar{3}m1$ $-TiS_2$ (blue: Ti, yellow: S)
a) side view; b) top view

Owing to the layered structure with a rather large interlayer gap, intercalation into TMDC is easily achieved for fundamental studies as well as for the technological application [145,146].

1.4.2 Intercalation and Exfoliation Chemistry

As layered materials are weakly bonded by vdW forces, can be cleaved easily to nanosheets to fulfil their full potential, just like a graphite crystal is easily cleaved to form graphene. The resulting monolayer of TiS_2 is called Ti sulphene[147]. The exfoliation of these materials in monolayers or structures with few layers preserves their properties and adds other appealing properties thanks to the quantum effects of confinement [148,149].

The exfoliation can be achieved by mechanical processing [150] or by intercalation of various organic or inorganic molecules followed by suspension of the easily exfoliated phase in a suitable solvent [151,152].

Intercalation is a chemical process to insert foreign species at the crystal gap [153,154], as illustrated in Figure 17.

Over the years, intercalation layered materials have received a lot of attention in the physical and electrochemical energy devices of condensed matter [155-157]. The most well-known electrochemical energy device using intercalation is the Li-ion

battery[158–160], in which Li-ions are intercalated at the vdW gaps reversibly for charging and discharging.

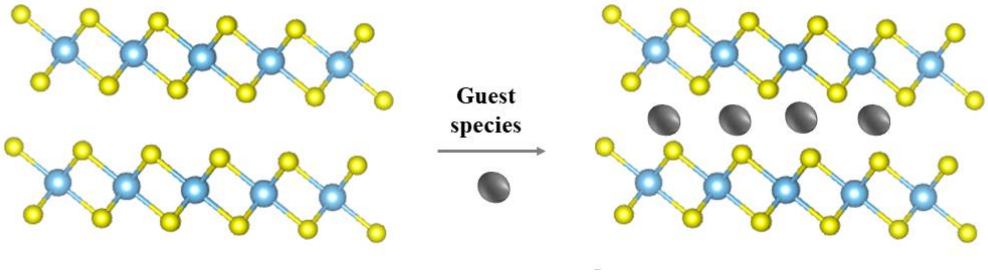

Figure 17. Schematic diagram for intercalation of a guest into TMDC layer materials.

Due to its layered structure, the TiS_2 compound is also prone to host in the vdW gap between S-Ti-S sandwiches a wide range of guest species, like monoatomic cations, molecular ions, and organic molecules [161–163]. This provides a way of improving the TE properties, including the increased phonons' scattering, and the consequent hindering of κ [164]. On the other hand, the fabrication of this type of heterostructure is expected to also affect the electronic transport properties, due to chemical interaction with the matrix and variation of carrier concentration [165]. The S and the σ of the TiS_2 layered compounds can then be optimized through the change in charge carrier concentration, so PF can be potentially increased in a specified temperature range. Also, intercalated layers in the structure can potentially create disorder reducing the κ_L. The overall ZT value of the material can be potentially increased using intercalation.

1.4.3 Inorganic/organic hybrid superlattices

In the wide range of possible hosts, the intercalation with organic molecules has recently been the subject of numerous studies [162,164,166–168].

TE devices in past years have been mostly based on inorganic compounds, yet hybrid TE materials have recently attracted a great deal of attention. The construction of inorganic/organic hybrids provides a lot of advantages. These

materials combine inorganic σ with typically organic flexibility and thermal resistivity [169].

Another interesting feature of hybrid materials is the possibility to recover electrical energy directly from low temperature, a crucial advantage over inorganic ones [170].

The exploitation of hybrid inorganic-organic materials could largely widen the spectrum of everyday applications. TE devices fed by the heat produced during metabolic processes are today considered a promising energy source for wearable electronics, such as fitness trackers, smartwatches, and medical sensors [171–174].

Furthermore, the construction of inorganic/organic hybris produces a lot of advantages in enhancing TE performance through the interlayers as well as the intralayer interactions.

Electronic carriers and phonons are confined in an inorganic layer sandwiched by two insulating organic layers. In particular, the confinement of electrons generates an increase in the DOS caused by the increase in effective mass, consequently generating a large S. Instead, the phononic confinement limits their two-dimensional movement with a consequent decrease in κ.

The inorganic layers and organic layers in a hybrid superlattice could form chemical bonds that are different from the weak vdW bond existing in a pristine compound. This bond formation would affect both electron and phonon transport.

In conclusion, electrostatic interactions between carrier electrons (or holes) in an inorganic layer and cations (or anions) in organic layers would affect electron transport. Long-range interactions between phonons in an inorganic layer and the dipole moment of polar molecules in organic layers would affect the phonon transport [175].

PART 2: INTERCALATION OF 2D CHALCOGENIDES BY INORGANIC SPECIES

2. Electronic properties of 2D transition metal dichalcogenides intercalated with metal interlayers

2.1 Introduction

In this chapter I present the computational investigations about the electronic structure of TiS_2 and MoS_2, two layered dichalcogenides that are widely investigated as promising 2D structures for the development of new TE materials. The adopted strategy is, as discussed in section 1.4, that of enhancing the 2D properties of these structures by intercalation of inorganic or organic species in the vdW gap between S-Me-S sandwiches. In this chapter the intercalation with Li, Ca, Ag, and Cu is investigated.

The organization of the work includes an initial phase aimed at TiS_2 to find the best parameters to be inserted in the Quantum Espresso input file to optimize the use of computing resources. The study continues with the analysis concerning the intercalation of the different species, to predict and understand the performance of the materials and to identify the best candidates for the development of TE devices. In the next chapter this computational study is integrated by a detailed investigation of the structural disorder induced by metal ion intercalation in the pristine host structure of a representative (Li-intercalated MoS_2) dichalcogenide.

2.2 TiS_2

The titanium disulphide TiS_2 is one of the transition metals dichalcogenides that crystallizes in the 1T-type CdI_2 structure (space group *P-3m1*), with nearly ideal octahedral coordination of the sulphur atoms about the titanium. The bulk TiS_2

consists of S-Ti-S sandwiches, separated in the z-direction by the vdW gap, as illustrated in Figure 18.

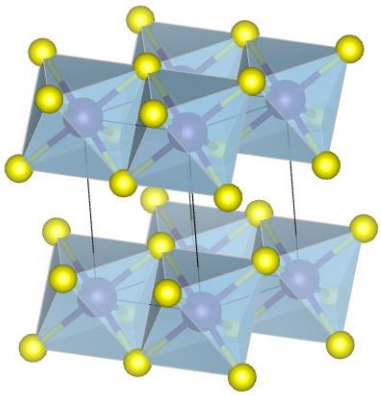

Figure 18. Schematic atomic geometry of layered 1T-TiS_2.

The diffraction pattern of TiS_2 (Sigma-Aldrich), reported in Figure 19, was acquired, and analysed to obtain the crystallographic parameters necessary to have a starting point for the subsequent simulations.

The analysis was performed with the Rietveld method [176,177] using the cif file in the "Crystallography open database" (www.crystallography.net) as a reference for the fitting.

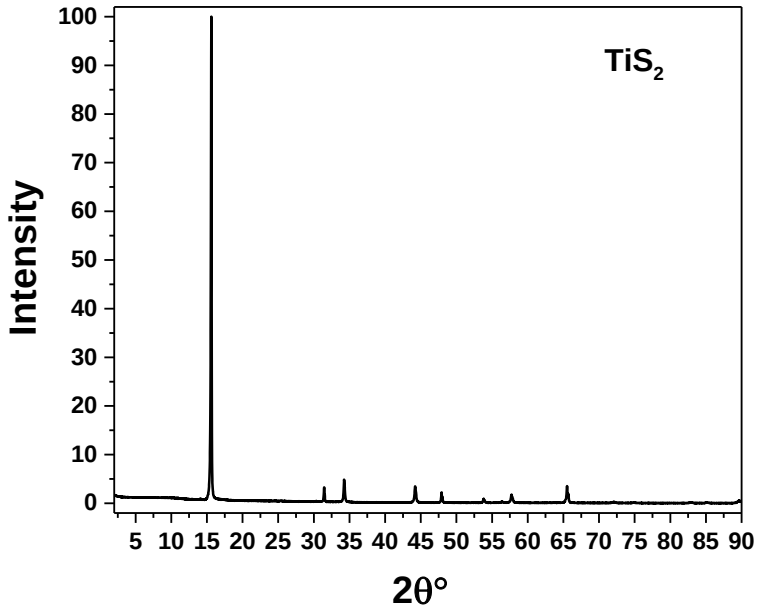

Figure 19 XRD pattern of TiS_2.

The diffraction pattern shows only the peaks relating to the (001) family of TiS_2, while the peaks with Miller indices h and k different from zero are absent or of negligible intensity.

Indeed, the fitting procedure has shown that the diffraction peaks have different relative intensities from those of the reference cif file. This inconsistency is caused by the presence of preferential orientations which, in turn, may be due to the preparation of the sample for measurement, which was placed on a slide and was pressed to obtain a flat surface, as required by the Bragg-Brentano geometry of the diffractometer. This procedure can cause, in the presence of highly anisotropic crystallites, a not completely random distribution of the orientation of the crystallites and the consequent systematic error in the intensity of the diffraction peaks. The Rietveld method made it possible to obtain the lattice parameters and the atomic positions of the atoms, shown in Tables 1 and 2.

Table 1. Lattice parameters, angles, and volume of the TiS_2 cell.

a (Å)	b (Å)	c (Å)	c/a	α	β	γ
3.4076 Å	3.4076 Å	5.6904 Å	1.9434	90º	90º	120º

Table 2. Atomic positions of the atoms inside the TiS_2 cell, in fractional coordinates.

	x	y	z
Ti	0.0000	0.0000	0.0000
S	0.3333	0.6667	0.2500
S	0.6667	0.3333	-0.2500

2.2.1 Determination of pseudopotentials and functionals

To determine the best combination of pseudopotentials (PAW or USPP) and functionals (LDA, PBE, or PBEsol) for TiS_2, a preliminary study was performed using a *vc-relax* calculation. The selection criterion was to favour the combination that produced the lattice parameters closest to those evaluated by the Rietveld fitting procedure.

From the output file processed using XCrysDen, a program that allows you to visualize molecular and crystalline structures, it was possible to obtain volumes and lattice parameters returned by the calculation. These parameters were subsequently compared with the experimental ones reported in Table 2, calculating the percentage error, as shown by Equation 13.

$$Percentage\ error\ (e\%) = \frac{|Experimental\ value - Calculated\ value|}{Experimental\ value}\ x100 \quad (13)$$

The detailed analysis relating to the lattice parameters *c* and *a* returned by the output file are present in Table 3, while the *c/a* ratio and the volume are reported in Table 4.

Table 3. Values of c, a, and the relative e% as the pseudopotential and functional vary.

	c	**e%**	***a***	**e%**
PAW_LDA	5.387	5.33 %	3.31	2.84 %
PAW_PBE	6.131	7.75 %	3.42	0.28 %
PAW_PBEsol	5.76	1.20 %	3.32	2.49 %
USPP_LDA	5.39	5.34 %	3.31	2.83 %
USPP_PBE	6.13	7.73 %	3.42	0.26 %
USPP_PBEsol	5.76	1.22 %	3.32	2.49 %

Table 4. Values of c/a, volume (V), and the relative e% as the pseudopotential and functional vary.

	c/a	**e%**	V	**e%**
PAW_LDA	1.63	2.56 %	51.14	10.63 %
PAW_PBE	1.79	7.45 %	62.00	8.35 %
PAW_PBEsol	1.73	3.79 %	55.06	3.78 %
USPP_LDA	1.63	2.59 %	51.15	10.62 %
USPP_PBE	1.79	7.44 %	61.97	8.30 %
USPP_PBEsol	1.73	3.80 %	55.07	3.76 %

When a PBEsol functional is used, both pseudopotentials show lower percentage errors. As regards the choice of the pseudopotential, it is evident that they do not influence the parameters under examination. Since the PAW pseudopotential is potentially more accurate, the subsequent calculations were performed using PBEsol-type functionals and PAW pseudopotential.

2.2.2 Determination of the Hubbard value for Ti

The same study, seen in the previous case, was carried out to obtain the best Hubbard (U) value for Ti, varying it from 0 eV to 3 eV. The trend of the percentage errors as the Hubbard parameter varies is shown in Figure 20.

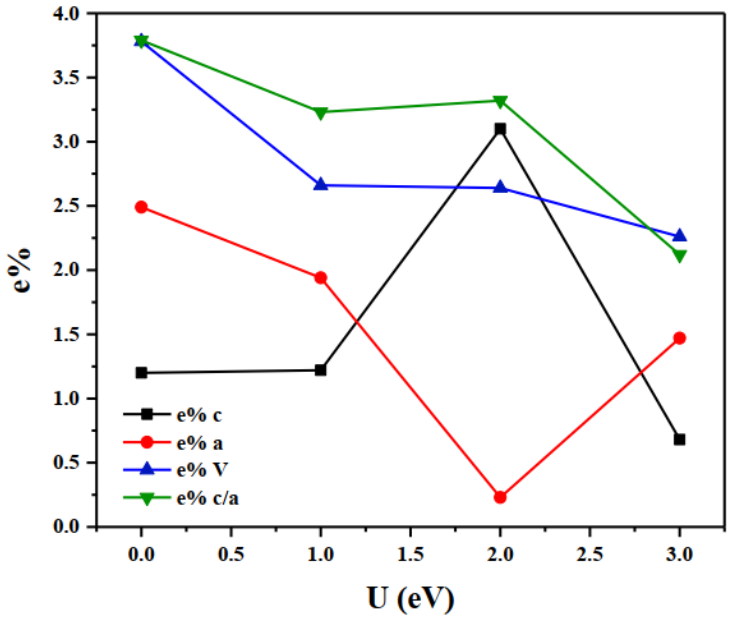

Figure 20. Trend of the percentage errors as the Hubbard parameter.

It is evident that lower e% correspond to U=3 eV for *c*, *c/a*, and V, therefore an in-depth study was carried out for Hubbard values around U=3 eV, which is in the range 2.5 eV and 3.5 eV, as shown in Table 5.

Considering the discordant trends of the lattice parameters *a* and *c*, the values of e% relating to the volume, and considering that the value of e% is minimal when

the Hubbard parameter is set at 2.6 eV, it can be stated that U=2.6 eV is the most suitable choice.

Table 5. Values of c, a, c/a, volume (V), and relative e% varying Hubbard from 2.5 eV to 3.5 eV.

	c	**e%**	***a***	**e%**	***c/a***	**e%**	**V**	**e%**
2.5	5.55	2.5	3.442	1.01	1.612	3.47	56.927	0.52
2.6	**5.649**	**0.73**	**3.444**	**1.06**	**1.64**	**1.78**	**58.021**	**1.39**
2.7	5.649	0.72	3.448	1.18	1.639	1.87	58.154	1.63
2.8	5.65	0.71	3.451	1.28	1.637	1.96	58.278	1.84
2.9	5.651	0.69	3.455	1.38	1.636	2.04	58.404	2.06
3.0	5.652	0.68	3.458	1.47	1.634	2.12	58.518	2.26
3.1	5.66	0.54	3.46	1.54	1.636	2.05	58.677	2.54
3.2	5.662	0.49	3.463	1.63	1.635	2.1	58.813	2.78
3.3	5.674	0.29	3.466	1.71	1.637	1.97	59.027	3.15
3.4	5.677	0.24	3.469	1.81	1.636	2.01	59.173	3.41
3.5	5.678	0.21	3.473	1.91	1.635	2.08	59.303	3.63

2.2.3 Determination of the Cutoff energy

Among the fundamental parameters for a calculation using Quantum Espresso, there are Ecutwfc, which indicates the kinetic energy cutoff of wave functions, and Ecutrho, which means that of charge density.

Ecutwfc is to set the number of plane waves used to calculate the DFT. If the value is high for the calculation of plane waves, the accuracy of the calculation is improved, but it takes a longer time to calculate it. Thus, setting the maximum kinetic energy cutoff to adjust the number of plane waves accurately finds the balance point between the number of plane waves and the calculation time.

To obtain the correct value of the ecutwfc parameter, which defines the cutoff energy for the wave function, a convergence test was performed. A convergence test is a way of optimizing the input script for a simulation to use limited computational resources efficiently. It is essential to find a proper initial setting for research to decide the accuracy and reliability of the simulation.

The values relating to the total energy of the system, as a function of cutoff, are shown in Figure 21.

The system reaches convergence when ecutwfc has a value of 50 Ry. Having chosen pseudopotentials of the PAW type, the energy value of ecutrho, which represents the cutoff for the charge density, is by default equal to 4 times the value of ecutwfc.

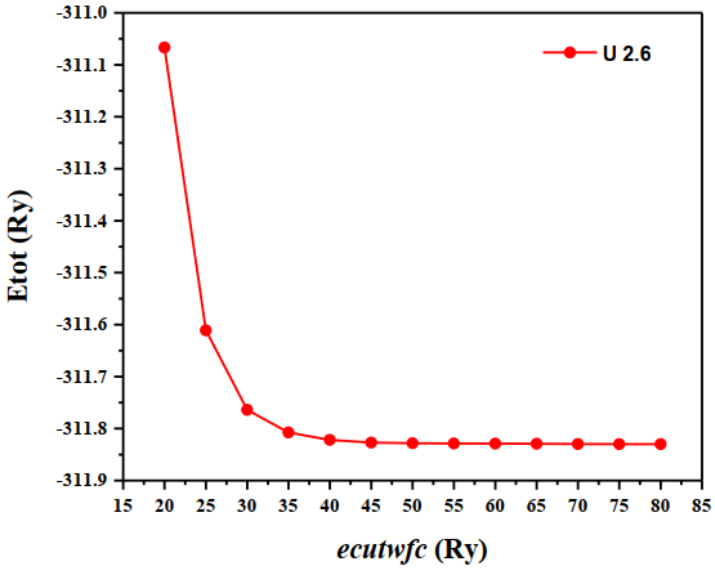

Figure 21. Variation of the total energy of the system as the ecutwfc varies.

2.2.4 Determination of the *Smearing* and *degauss*

DFT codes calculate the ground state electronic density using a scf cycle. Smearing the electronic structure was proposed to deal with band sloshing and to reduce the number of k-points required by accelerating the convergence of the band energy calculation concerning k-point density. Band sloshing typically occurs when there are many states near the Fermi level, that alternately shift above and below the

Fermi level in SCF cycles, resulting in the charge moving back and forth, never settling [178,179].

The most suitable smearing function was then determined, among Gaussian, Fermi-Dirac, Marzari-Vanderbilt, and Methfessel-Paxton, to treat the occupation of the states in the TiS_2.

Scf calculations were performed and the variation of the total energy of the system was studied as the degauss parameter varies, which governs the Gaussian spread for the various smearing functions, as shown in Figure 22.

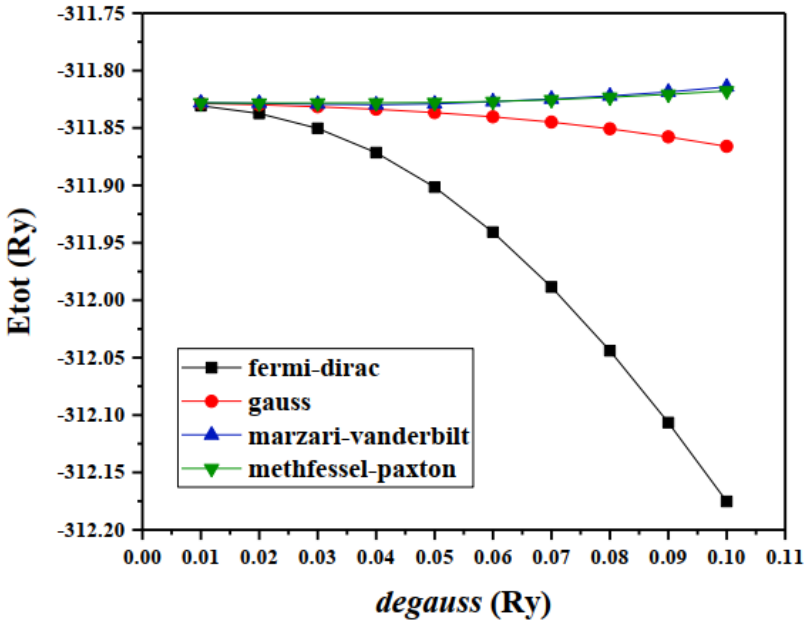

Figure 22. Variation of energy as the value of the Gaussian spread (degauss) varies for the various smearing functions.

From Figure 22 it is possible to see how Marzari-Vanderbilt and Methfessel-Paxton are less dependent on the degauss value than the Fermi-Dirac and Gaussian functions; this ensures a stable trend of the total energy of the system and therefore allows for faster calculations and safer convergence.

To understand which of the two systems was the best, the values and percentage errors of cell parameters *c* and *a*, *c/a*, and volume (V) were studied for Marzari-Vanderbilt and Methfessel-Paxton in the range of degauss parameters between 0.01

and 0.05, where the curves undergo a rapid increase. The results of this study are reported in Tables 6 and 7.

Table 6. Values and percentage errors of c, a, c/a, and V for Marzari-Vanderbilt varying degauss between 0.01 and 0.05.

	c	**e%**	**a**	**e%**	**c/a**	**e%**	**V**	**e%**
0.01	5.649	0.73	3.444	1.06	1.640	1.78	58.022	1.40
0.02	5.567	2.17	3.435	0.82	1.620	2.96	56.906	0.55
0.03	5.604	1.52	3.424	0.47	1.637	1.98	56.882	0.59
0.04	5.623	1.18	3.414	0.18	1.647	1.36	56.753	0.82
0.05	5.625	1.15	3.412	0.13	1.648	1.28	56.714	0.89

Table 7. Values and percentage errors of c, a, c/a, and V for Methfessel-Paxton varying degauss between 0.01 and 0.05.

	c	**e%**	**a**	**e%**	**c/a**	**e%**	**V**	**e%**
0.01	5.699	0.15	3.443	1.05	1.655	0.89	58.520	2.27
0.02	5.652	0.67	3.433	0.75	1.646	1.41	57.696	0.83
0.03	5.637	0.94	3.425	0.50	1.646	1.44	57.253	0.05
0.04	5.644	0.81	3.418	0.30	1.651	1.11	57.095	0.22
0.05	5.653	0.65	3.411	0.11	1.657	0.76	56.973	0.44

From the data appears that the lowest percentage errors are obtained for Marzari-Vanderbilt with degauss 0.01, 0.02, and 0.05 and Methfessel-Paxton with degauss 0.01, 0.03, and 0.05.

Subsequently, it was decided to carry out an in-depth study for both types of smearing. The band gaps relating to the G-G transition, shown in Table 8, were compared with the experimental band gap reported in the bibliography equal to 0.48 ± 0.2 eV [180].

Table 8. Band gap (eV) related to the G-G transition of TiS2 with the Marzari-Vanderbilt smearing function (mv) and Methfessel-Paxton smearing function (mp).

	mv	mp
0.01	0.48	0.59
0.02	0.58	0.53
0.03	0.47	0.73
0.04	0.62	0.60
0.05	0.65	0.63

The table shows that the band gaps closest to the experimental data are Marzari-Vanderbilt with 0.01 and 0.03 degauss and Methfessel-Paxton with 0.02 degauss. Among these, Marzari-Vanderbilt with 0.01 degauss was chosen. The Methfessel-Paxton approach can cause problems in procedures such as displaying the DOS, as it can result in negative occupancy values [181].

2.2.5 Lattice parameters

A study related to the lattice parameters was then performed. Using scf calculations the parameters celldm(1), which corresponds, in Bohr units, to the cell parameter *a*, and celldm(3), corresponding to the ratio *c/a*, were calculated. The total energy of the system as celldm(1) and celldm(3) vary is shown in Figures 23 and 24.

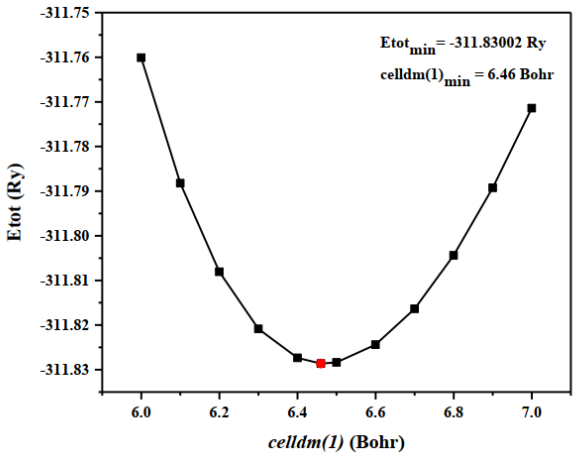

Figure 23. Variation of the total energy of the system as celldm(1) varies.

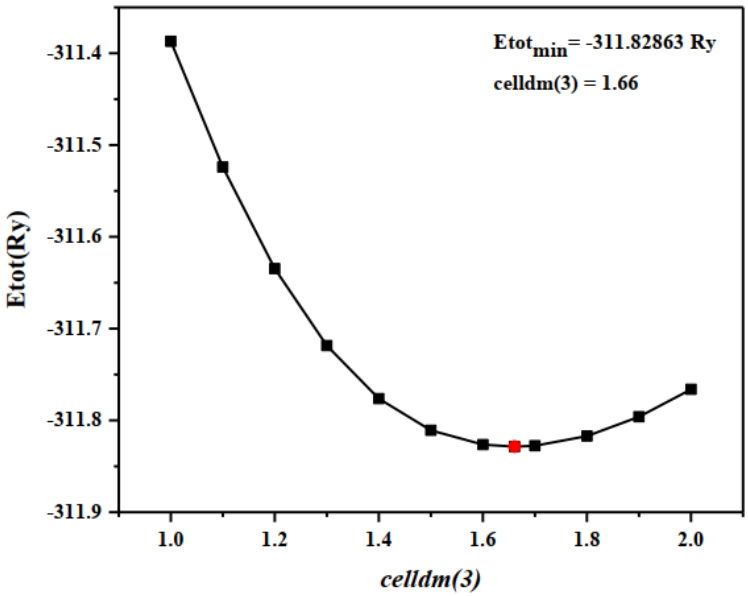

Figure 24. Variation of the total energy of the system as celldm(3) varies.

The outcome of this analysis was that the energy minima occurred at 6.46 Bohr (3.42 Å) for celldm(1) and 1.66 for celldm(3).

Subsequently, a structural optimization was performed, through the vc-relax calculation, which produced a slight modification in the cell parameters and the fractional atomic coordinates. The latter values are shown in Table 9.

Table 9. Atomic positions of TiS_2 resulting from the vc-relax calculation.

	x	y	z
Ti	0.000	0.000	0.000
S	0.333	0.667	0.251
S	0.667	0.333	-0.251

2.2.6 Determination of the electronic structure

With the XCrysDen program, it was possible, using the output file of the vc-relax calculation, to visualize the first Brillouin zone of the *P-3m1* space group, as shown in Figure 25, to identify the k-points with high symmetry, shown in Table 10, and select the reciprocal space path in which to represent the energy bands of TiS_2.

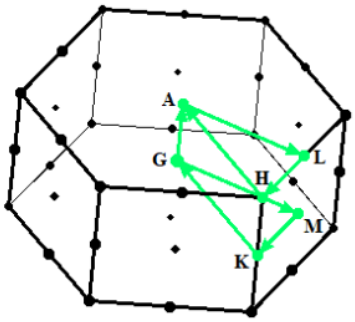

Figure 25. First Brillouin zone of TiS_2, points of high symmetry, and path for the visualization of the bands in k-space.

Table 10. Coordinates of high symmetry k-points in the first Brillouin zone of TiS_2.

	Cartesian coordinates
Γ	0.000 0.000 0.000
M	0.000 0.500 0.000
K	-0.333 0.667 0.000
Γ	0.000 0.000 0.000
A	0.000 0.000 -0.500
L	0.000 0.500 -0.500
H	-0.333 0.667 -0.500
A	0.000 0.000 -0.500

Finally, the electronic band structure and the DOS of TiS_2 were constructed, as shown in Figure 26.

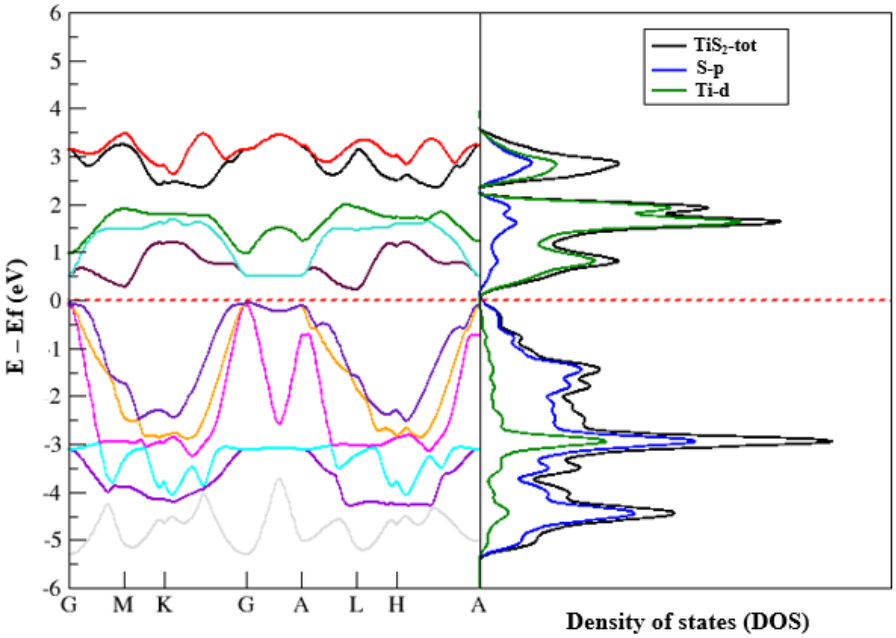

Figure 26. Band electronic structures, the total DOS of TiS2, and the projected DOS on the states specified in the legend.

For both graphs, the ordinate axis shows the values of the difference between the band energy and the Fermi energy expressed in eV, while the abscissa axis for the graph on the left shows the sequence of k points, and for the graph on the right the DOS in relative scale. The absolute maximum of the valence band is in Γ, while the absolute minimum of the conduction band is at points L and M as shown in the graph relating to the electronic band structure.

From the graph relating to the DOS, it is possible to observe that, as expected, the 3p orbitals of sulphur prevail in the valence band while the 3d orbitals of titanium prevail in the conduction band.

2.3 Ti_4S_8 supercell

The TiS_2 supercell (Ti_4S_8), shown in Figure 27, was constructed by doubling the lattice parameters *a* and *b*, obtaining a 2x2x1 supercell. The celldm(1) and the celldm(3) assume the values 12.92 Bohr (6.83 Å) and 0.83 respectively.

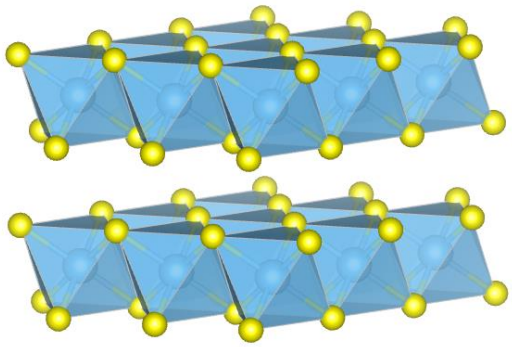

Figure 27. Ti_4S_8 supercell

The electronic band structure and the DOS of Ti_4S_8 are shown in Figure 28.

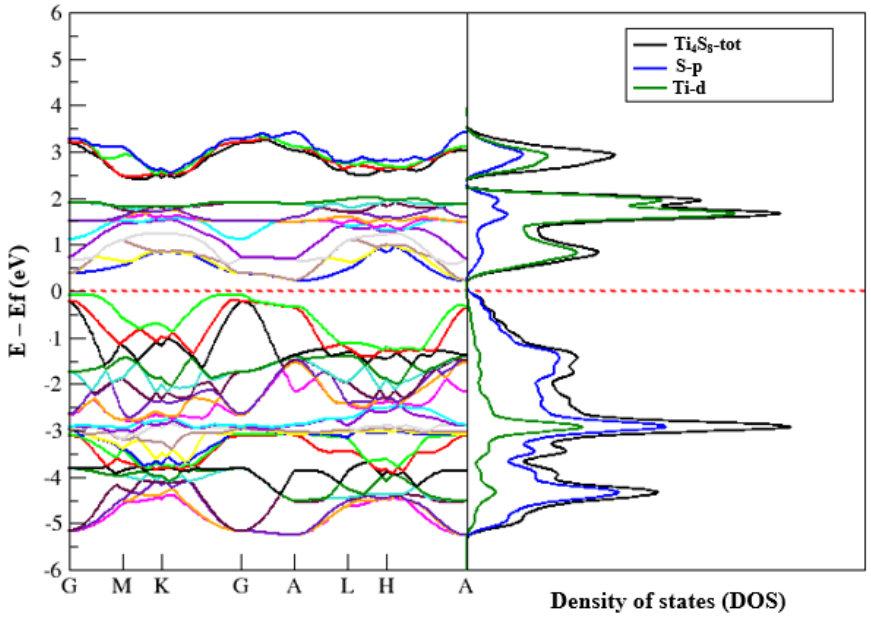

Figure 28. Band electronic structures, the total DOS of Ti_4S_8, and the projected DOS on the states specified in the legend.

Comparing Figure 28 with Figure 26 it is evident that the number of bands of the supercell is greater than that of the single cell of TiS_2, a consequence of the fact that in the case of the supercell, there is a greater number of atoms. The band gaps of the two systems are similar, as well as the DOS.

2.4 Intercalation of metals inside the Ti_4S_8 supercell

The simulation of the doping of a periodic structure requires the introduction in the calculations of a supercell, which will be the larger the smaller the stoichiometric coefficient of the dopant. In the case of TiS_2, the doping takes place by intercalation of the dopant species in the vdW gap between the S-Ti-S triple layers. In the supercell 2x2x1 it is possible to introduce a metal every four titans, obtaining a composition $M_{0.25}TiS_2$, shown in Figure 29a, or two intercalating metals every four titans, of composition $M_{0.50}TiS_2$, shown in Figure 29b.

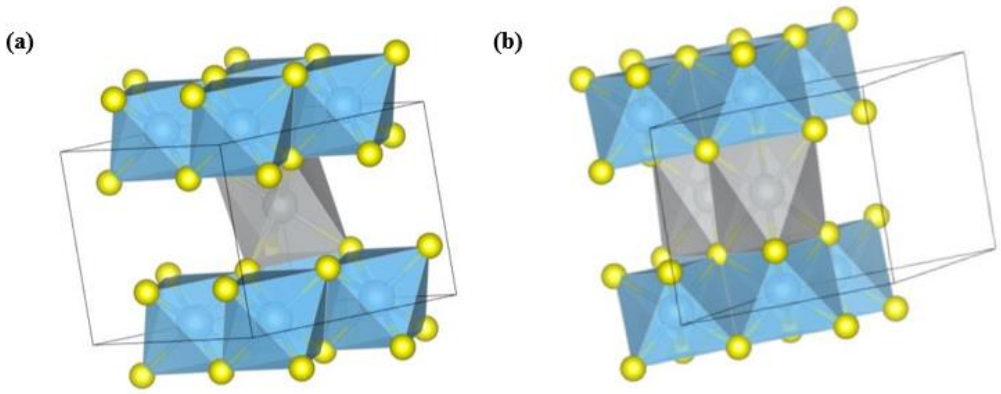

Figure 29. Structure of $M_{0.25}TiS_2$ (a) and $M_{0.50}TiS_2$ (b).

2.4.1 Supercells of $Li_{0.25}TiS_2$ and $Li_{0.50}TiS_2$

Lithium was intercalated between the layers of the 2x2x1 supercell of TiS_2, in a ratio of 1:4 and 1:2 concerning titanium, to obtain supercells of $Li_{0.25}TiS_2$ and $Li_{0.50}TiS_2$ composition.

For both structures, a study concerning the variation of the total energy with celldm(1) and celldm(3) was conducted. In the case of $Li_{0.25}TiS_2$ the celldm(1) and

the celldm(3) assume the values 12.93 Bohr and 0.84 respectively; for $Li_{0.50}TiS_2$ the respective values are celldm(1)=12.92 Bohr and celldm(3)=0.83. The electronic structure and the related DOS of $Li_{0.25}TiS_2$ are shown in Figure 30.

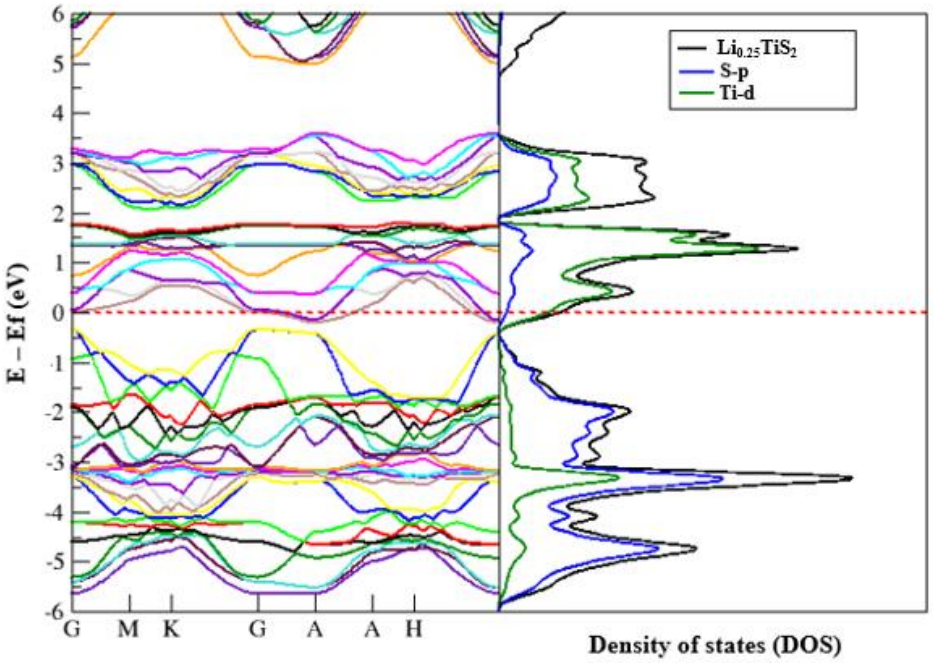

Figure 30. Band electronic structures, the total DOS of $Li_{0.25}TiS_2$, and projected DOS on the states specified in the legend.

In the intercalated compound, unlike what occurs in TiS_2, the Fermi level cuts some bands of the conduction region, so determining metallic conduction properties for $Li_{0.25}TiS_2$. The DOS graph also shows, as in the case of non-intercalated TiS_2, that the 3p orbitals of sulphur prevail in the valence bands, while the 3d orbitals of titanium prevail in the conduction region. The variations that occur in the electronic structure of the intercalated compound concerning TiS_2 is attributed to a charge transfer from lithium to TiS_2, giving rise to Li^+ upon intercalation, rather than to the formation of covalent Li-S bonds [182].

By changing the composition, a similar study was conducted for the $Li_{0.50}TiS_2$ supercell, which produced the results described below. The electronic structure and the related DOS of $Li_{0.50}TiS_2$ are shown in Figure 31.

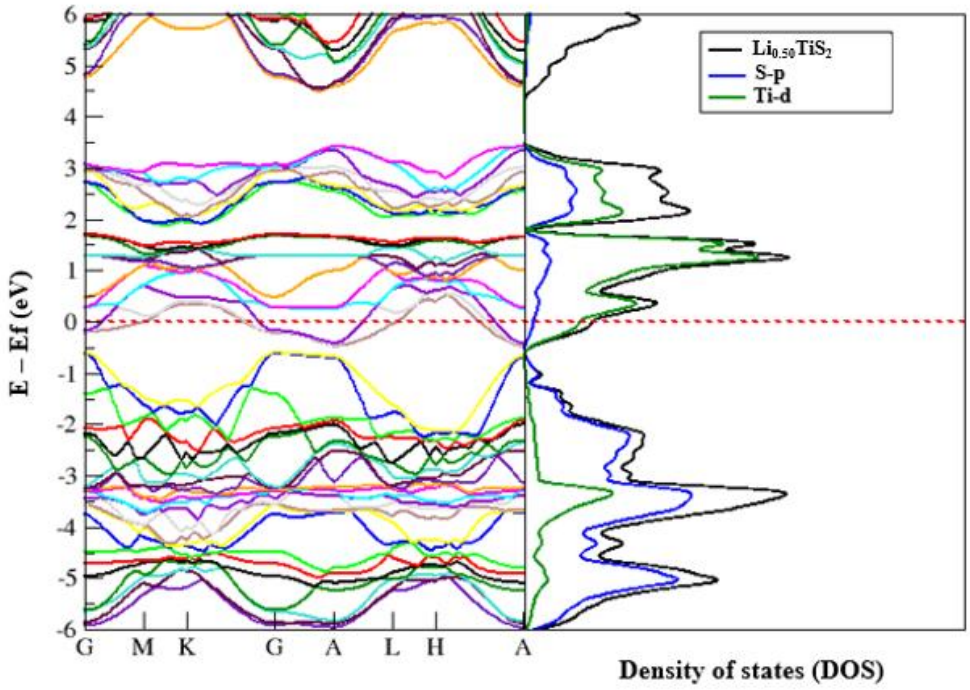

Figure 31. Band electronic structures, the total DOS of $Li_{0.50}TiS_2$, and projected DOS on the states specified in the legend.

Comparison of Figure 31 with Figure 30 shows that some bands move further below the Fermi level. On the other hand, only minor changes can be recognized in the band structure and in the DOS distribution, confirming for $Li_{0.50}TiS_2$ the charge donation of to the TiS_2 matrix and the prevalence of S-3p orbitals in the region of the valence bands and of Ti-3d orbitals in the conduction region.

2.4.2 Supercells of $Ca_{0.25}TiS_2$ and $Ca_{0.50}TiS_2$

The same procedure applied to the previous supercells was rried out for $Ca_{0.25}TiS_2$ and $Ca_{0.50}TiS_2$. In the case of $Ca_{0.25}TiS_2$ celldm(1)=12.92 Bohr and celldm(3)=0.90; for $Ca_{0.50}TiS_2$ these values are 13.00 Bohr and 0.90, respectively.

The electronic structure and the DOS and pDOS of $Ca_{0.25}TiS_2$ are shown in Figure 32.

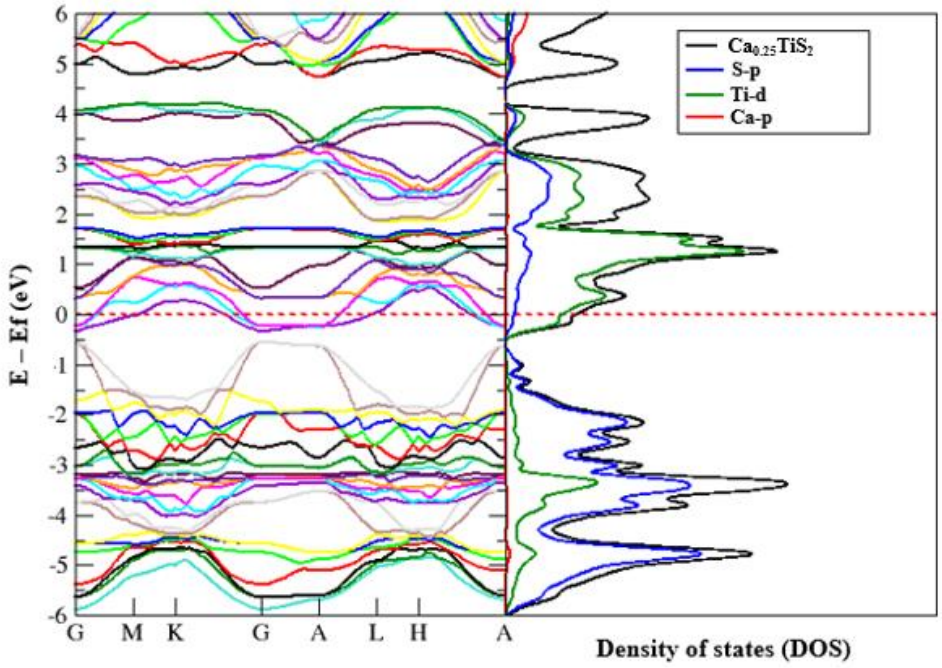

Figure 32. Band electronic structures, the total DOS of $Ca_{0.25}TiS_2$, and projected DOS on the states specified in the legend.

The analysis of the bands in Figure 32 and comparison with the electronic structure of pristine TiS_2 (Figure 28) shows that the intercalated calcium alters the electronic structure of TiS_2, as can be seen from the accumulation of bands beyond the energy of ~3 eV and from a sizeable lowering of the energy of states, leading to the intersection of some energy bands with the Fermi level. Once more, the DOS evidences a greater contribution of the 3s orbitals of sulphur in the region of the valence bands and of the 3d orbitals of titanium for the conduction ones; the contribution of the orbitals of calcium is not visible in the range considered.

The next step was to consider the $Ca_{0.50}TiS_2$ supercell. The electronic structure and DOS and pDOS of $Ca_{0.50}TiS_2$ are shown in Figure 33.

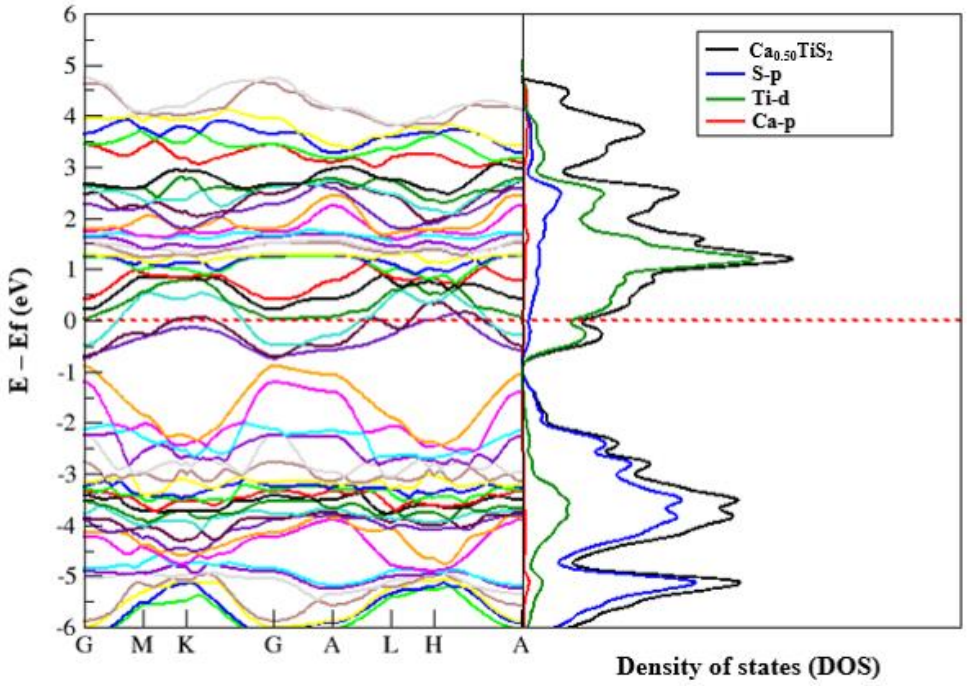

Figure 33. Band electronic structures, the total DOS of $Ca_{0.50}TiS_2$, and projected DOS on the states specified in the legend.

The calculated bands accumulate towards the Fermi level, which cuts several bands; a small band gap can be recognized at the G-G transition. Overall, the DOS shows a high number and a continuity of occupied states at the Fermi level; also in this case, the 3d orbitals of titanium prevail in the valence bands and the 3p of sulphur in the conduction region.

2.4.3 Supercells of $Ag_{0.25}TiS_2$ and $Ag_{0.50}TiS_2$

In the case of $Ag_{0.25}TiS_2$ the celldm(1) and the celldm(3) assume the values 12.95 Bohr and 0.86, respectively; for $Ag_{0.50}TiS_2$, celldm(1)=13.00 Bohr and celldm(3)= 0.89. The electronic structure and the DOS of $Ag_{0.25}TiS_2$ are shown in Figure 34.

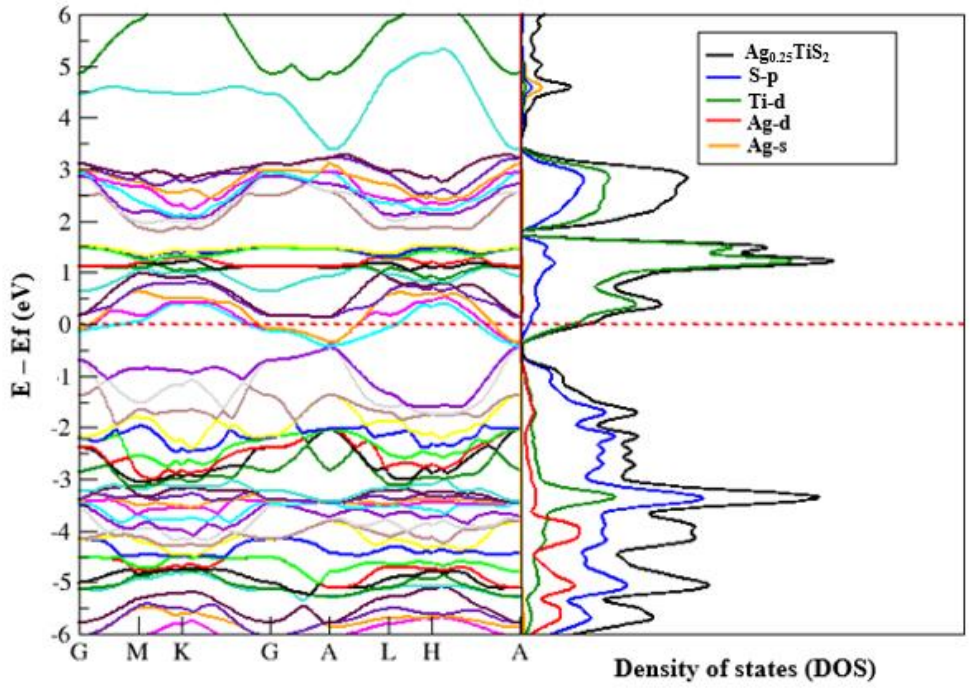

Figure 34. Band electronic structures, the total DOS of $Ag_{0.25}TiS_2$, and projected DOS on the states specified in the legend.

The presence of silver drastically modifies the electronic structure of TiS_2. From inspection of Figure 34 and comparison with Figure 28 it is observed that conduction bands accumulate beyond 3 eV and a general lowering of energies determine the intersection of some bands with the Fermi level; a small direct gap is present at point A. From the DOS relative to the valence bands, the contributions of the 3d orbitals of titanium, the 3p orbitals of sulphur, and the 4d orbitals of silver are all significant, while in the conduction bands the contribution of the 3d orbitals of Ti prevail.

The next step was to consider the $Ag_{0.50}TiS_2$ supercell. The electronic structure and the DOS of $Ag_{0.50}TiS_2$ are shown in Figure 35.

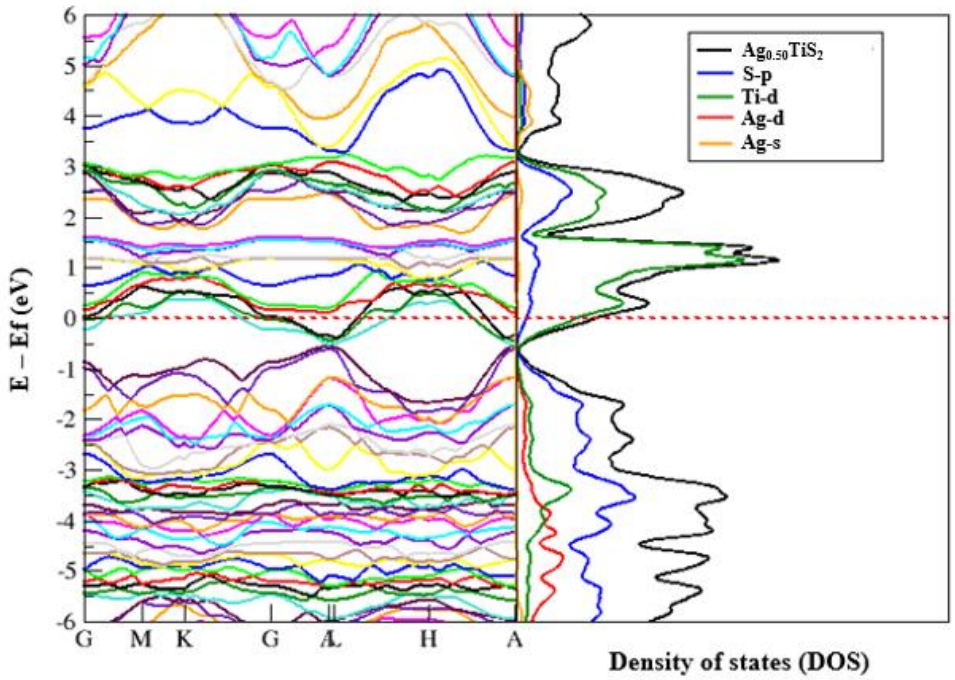

Figure 35. Band electronic structures, the total DOS of $Ag_{0.50}TiS_2$, and projected DOS on the states specified in the legend.

Compared to the results relative to $Ag_{0.25}TiS_2$ (Figure 34), Figure 35 shows a greater number of bands and a shift of energy levels to lower values with respect to the Fermi level. Concerning the DOS, the contributions of the 3d orbitals of titanium, the 3p orbitals of sulphur, and the 4d orbitals of silver are significant in the valence bands. Also in this case, in the conduction region the contribution of the 3d orbital of Ti prevails and a small A-A gap can be observed in the valence energy region.

2.4.4 Supercells of $Cu_{0.25}TiS_2$ and $Cu_{0.50}TiS_2$

The celldm(1) and the celldm(3) values of $Cu_{0.25}TiS_2$ are 12.92 Bohr and 0.83 respectively, while the corresponding parameters relative to $Cu_{0.50}TiS_2$ are 13.00 and 0.83 Bohr. The band structure and the DOS of $Cu_{0.25}TiS_2$ are shown in Figure 36.

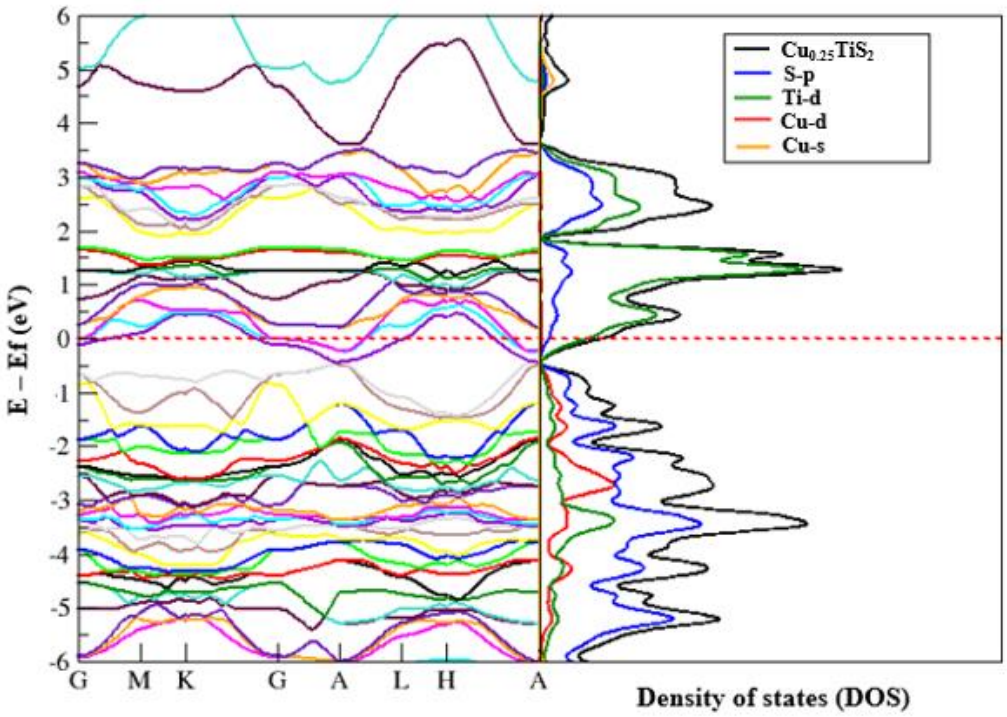

Figure 36. Band electronic structures, the total DOS of $Cu_{0.25}TiS_2$, and projected DOS on the states specified in the legend.

Also, for $Cu_{0.25}TiS_2$, as for the silver-intercalated samples, the Fermi level cuts the conduction bands. The pDOS evidence a prevalence of the 3d orbitals of titanium in the conduction band, while in the valence bands there is a prevalence of the 3p orbitals of sulphur. In the considered energy range, the contribution of copper is visible in the valence bands. The variation that the presence of copper causes in the electronic structure of TiS_2 is attributed to a charge transfer from intercalated copper to TiS_2 [183].

The electronic structure and the DOS of $Cu_{0.50}TiS_2$ are shown in Figure 37.

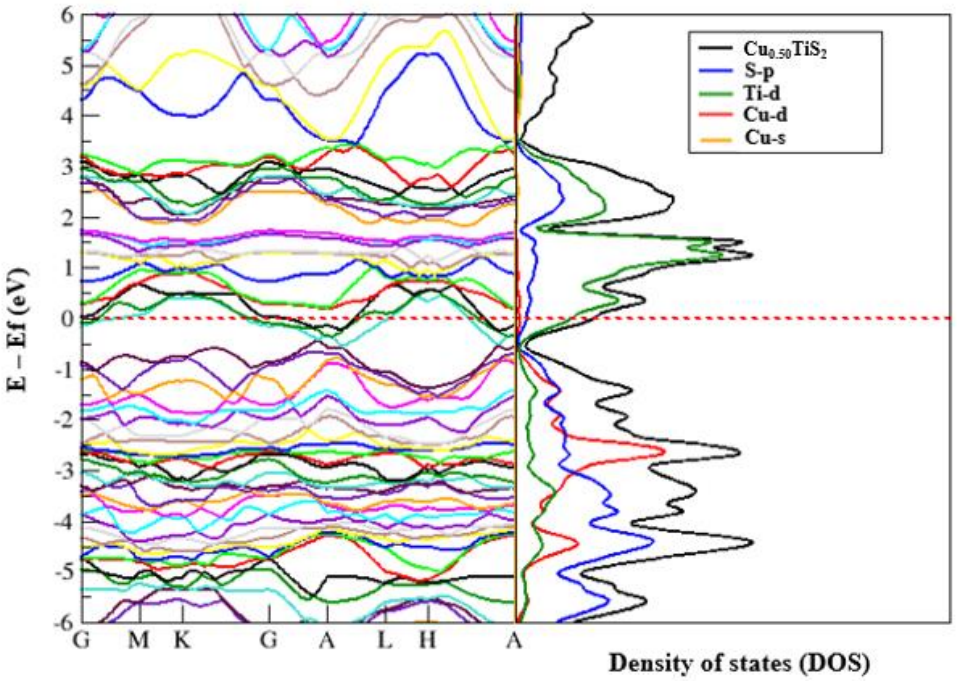

Figure 37. Band electronic structures, the total DOS of $Cu_{0.50}TiS_2$, and projected DOS on the states specified in the legend.

With respect to $Cu_{0.25}TiS_2$, in the reported energy range there are a greater number of bands and a slight lowering of energy levels. This latter rearrangement determines the overcome of the small gap that can be recognized at point A in $Cu_{0.25}TiS_2$ (Figure 36), so that the whole range of energies of $Cu_{0.50}TiS_2$ below the Fermi level is constituted by occupied states.

2.4.5 Bader charges

To quantitatively evaluate the charge transfer from intercalant metals to host TiS_2, put forth in the above quoted analyses and in some literature papers [182,183], the electron densities (in the form of Bader charges) of pristine TiS_2 and of the different intercalated compounds are reported in Table 11 for the $Me_{0.25}TiS_2$ stoichimetries and in Table 12 for the $Me_{0.25}TiS_2$ compositions. Actually, the Bader charge analysis substantiates a transfer of electronic charge to the inorganic scaffold which increases with the concentration of the intercalated metal.

Table 11. Bader charges of TiS_2 and of the respective intercalation compounds with Li, Ca, Ag, and Cu with $Me_{0.25}TiS_2$ stoichiometry.

	TiS_2	$Li_{0.25}TiS_2$	$Ca_{0.25}TiS_2$	$Ag_{0.25}TiS_2$	$Cu_{0.25}TiS_2$
Ti	10.26	10.27	10.31	10.26	10.30
S	6.87	6.97	7.02	6.93	6.92
Me	-	2.13	8.52	10.54	10.47

Table 12. Bader charges of TiS_2 and of the respective intercalation compounds with Li, Ca, Ag, and Cu with $Me_{0.50}TiS_2$ stoichiometry.

	TiS_2	$Li_{0.50}TiS_2$	$Ca_{0.50}TiS_2$	$Ag_{0.50}TiS_2$	$Cu_{0.50}TiS_2$
Ti	10.26	10.31	10.42	10.32	10.36
S	6.87	7.064	7.11	6.95	6.95
Me	-	2.12	8.73	10.56	10.47

2.4.6 Conclusions

The presence of lithium and calcium in the vdW gap of TiS_2 causes an energy shift of the electronic bands, which intersect the Fermi level and determine the metallic character of electronic conduction in the intercalated compounds. By increasing the concentration of intercalants, the energy bands are generally lowered with respect to the Fermi level, determining a metallic conduction character.

Silver intercalation causes a drastic variation in the electronic structure of pristine TiS_2. As the concentration of Ag increases, the bands of the conduction region tend to accumulate towards the Fermi level.

The intercalation of Cu was also investigated and evidenced, like Ag, the intersection of the conduction bands with the Fermi level. As concerns in particular $Cu_{0.50}TiS_2$, the energy range below the Fermi energy is entirely covered by occupied states, so enhancing the metallic character of the intercalated compound.

In comparison with the first and second group intercalants, the transition metals cause a definite variation of the electronic structure of TiS_2. Lithium does not contribute to the density of electronic states of TiS_2, while calcium contributes minimally with p-orbitals. Even if belonging to the same group, Cu and Ag behave slightly differently. Actually, comparison between Figures 35 and 37, relating

respectively to $Ag_{0.50}TiS_2$ and $Cu_{0.50}TiS_2$, show that, beside the above cited intersection between valence and conduction energy bands, leading to overcome energy gaps in the whole reported energy range, the contribution of the Cu-d orbitals to the total DOS is larger.

The results obtained demonstrated that the insertion of metals in the vdW gap of TiS_2 determines the metallic conduction character of the compounds under consideration. The evaluation of how much the concentration of charge carriers affects the ZT and PF parameters, remains a matter of further computational simulations and experimental determination.

2.5 MoS_2 and Li intercalation

The crystal structure of molybdenum disulphide (MoS_2) takes the form of a hexagonal plane of S atoms on either side of a hexagonal layer of Mo atoms, as shown in Figure 38. The sulphur planes stack on top of each other, determining a prismatic coordination of molybdenum. Referring to the projection of the Mo and S atoms onto the (**a**,**b**) basal plane, the sequence along **c** of the S and Mo layers can be represented as AbA BaB AbA and so on, where the upper-case letters are relative to sulphur and the lower-case to Mo. The structure is characterized by strong covalent bonds between the Mo and S atoms, and by weak vdW forces holding together the triple layers S-Mo-S.

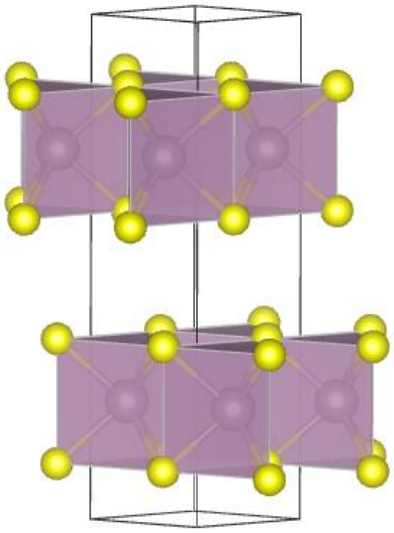

Figure 38. Crystal structure of MoS_2.

To obtain the best value of the parameters to insert in the Quantum Espresso input file, an initial study like the one performed for TiS_2 was performed.

The value relating to the energy for the wave function (ecutwfc) was found to be equal to 60 Ry, while the cutoff for the charge density (ecutrho) was 480 Ry. The determined celldm(1) and the celldm(3) values are 5.78 Bohr and 4.21, respectively. A structural optimization, performed through the vc-relax calculation, produced a slight modification in the cell parameters and the fractional atomic coordinates. These latter values are shown in Table 13.

Table 13. Atomic positions of MoS_2 resulting from the vc-relax calculation.

	x	**y**	**z**
Mo	0.333	0.667	0.250
Mo	0.667	0.333	0.750
S	0.333	0.667	0.6266
S	0.667	0.333	0.3734
S	0.333	0.667	0.8734
S	0.667	0.333	0.1266

Table 14 details the reciprocal path used to represent the MoS_2 energy bands.

Table 14. Coordinates of high symmetry k-points in the first Brillouin zone of MoS_2.

	Cartesian coordinates
Γ	0.000 0.000 0.000
M	0.500 0.000 0.000
K	0.333 0.333 0.000
Γ	0.000 0.000 0.000
A	0.000 0.000 0.500
L	0.500 0.000 0.500
H	0.333 0.333 0.500
A	0.000 0.000 0.500

The electronic band structure and the relevant DOS are shown in Figure 39. The calculated indirect band gap is equal to 1.19 eV.

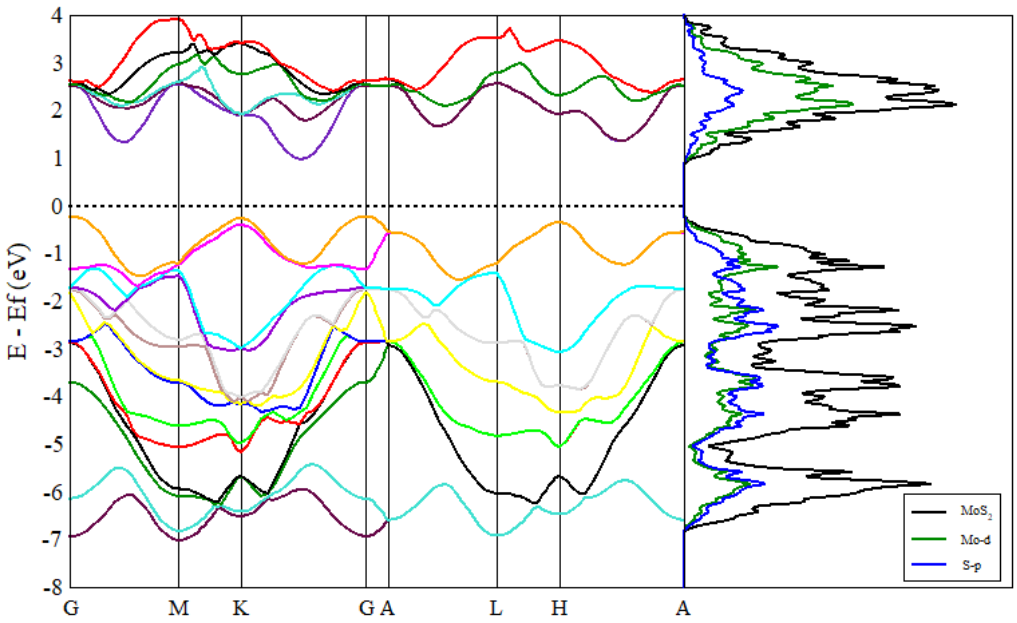

Figure 39. Band electronic structures, the total DOS of MoS_2, and the projected DOS on the states specified in the legend.

The conduction band minimum lies midway between the Γ and K points, while the valence band maximum is at Γ.

The DOS can be divided into two parts: below the Fermi energy, whre the equivalent contributions of S-3p and the Mo-4d orbitals can be recognized, and above the Fermi energy, where the main contribution is due to the 4d orbital of Mo.

In the case of MoS_2, the lithium intercalation simulation was carried out by allowing the insertion of Li in correspondence to each molybdenum. This model didn't request the introduction in the calculation of a supercell. In fact, it was considered the possibility that lithium intercalates every two S-Mo-S sandwiches, giving rise to the $Li_{0.50}MoS_2$ composition shown in Figure 40a, while the full intercalation, corresponding to the $LiMoS_2$ stoichiometry, is shown in Figure 40b.

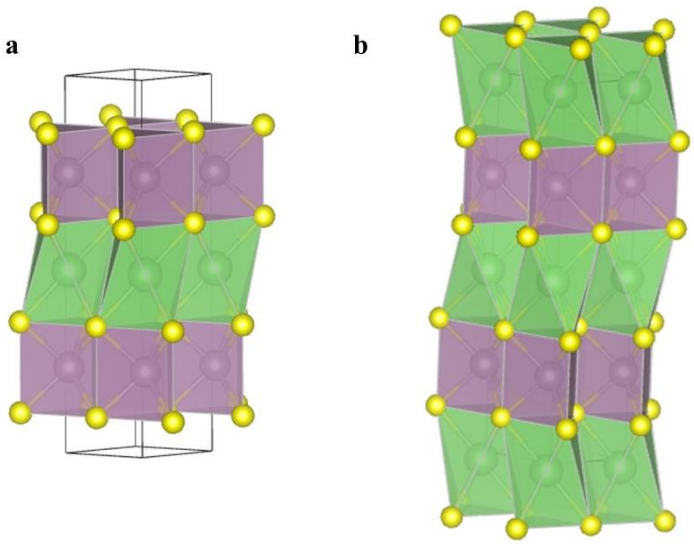

Figure 40. Crystal structure of a) $Li_{0.50}MoS_2$ and b) $LiMoS_2$.

The lithium intercalation modifies the distance between the layers. For this reason, for both structures, a study concerning the energy convergence of celldm(1) and celldm(3) parameters was conducted. In both cases the celldm(1) assumes the value 5.78 Bohr, while celldm(3) resulted as 4.51 in $Li_{0.50}MoS_2$ (Figure 41a) and 4.71 in $LiMoS_2$ (Figure 41b).

a

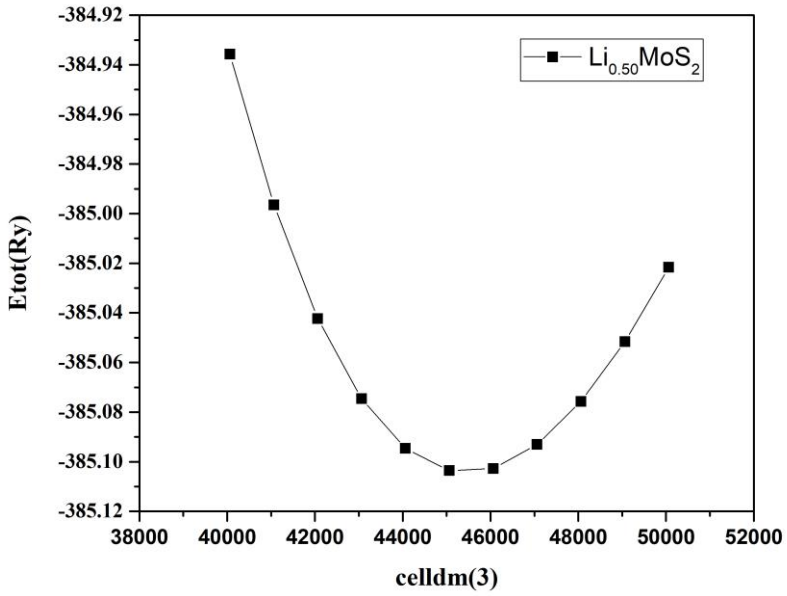

b

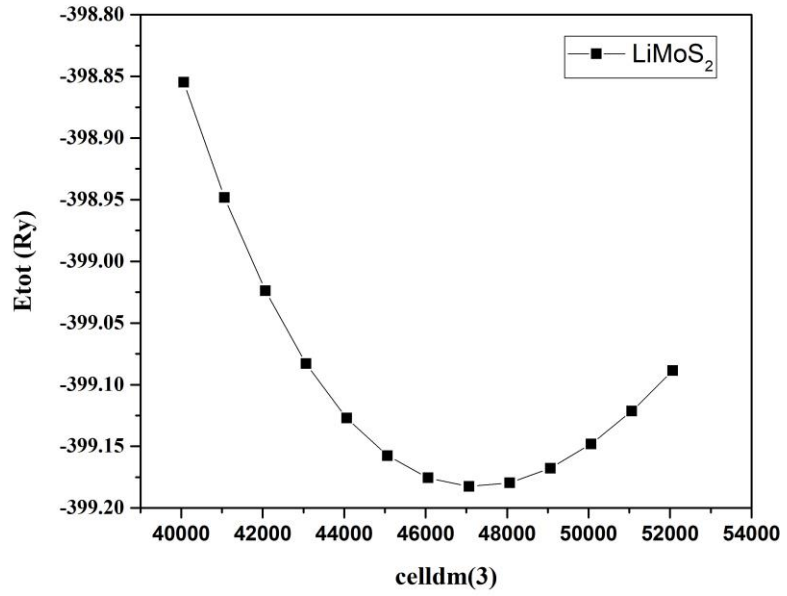

Figure 41. Variation of the total energy of the system as celldm(3) varies. a) $Li_{0.50}MoS_2$; b) $LiMoS_2$

The electronic structure of $Li_{0.50}MoS_2$ is reported in Figure 42.

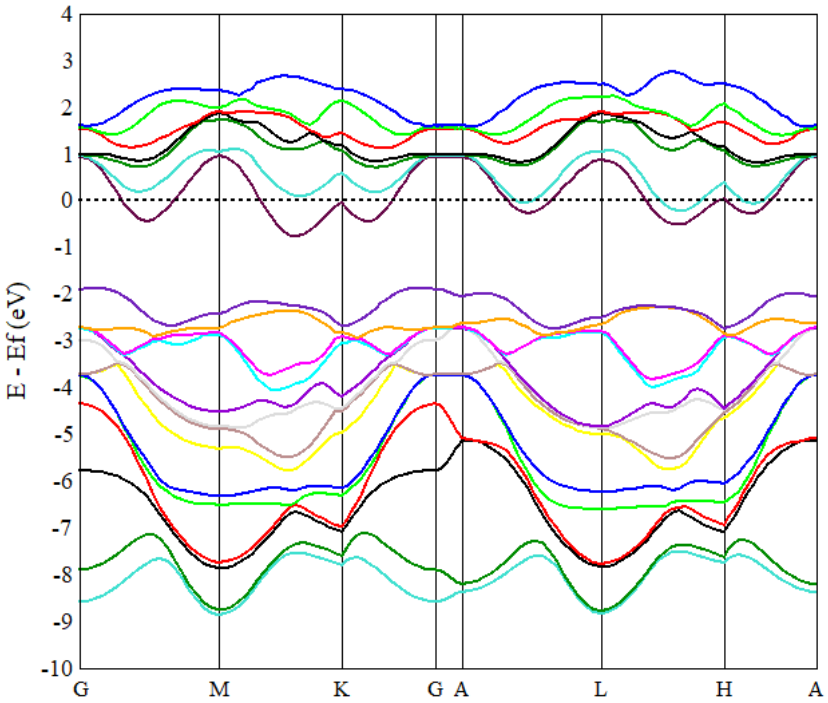

Figure 42. Band electronic structures of $Li_{0.50}MoS_2$.

As shown in Figure 42, the Fermi level intersects the conduction energy region, unlike what occurs in pristine MoS_2, so determining the metallic conduction character of $Li_{0.50}MoS_2$.

A similar study was conducted for $LiMoS_2$, producing the results described below. The electronic structure of $LiMoS_2$ is shown in Figure 43.

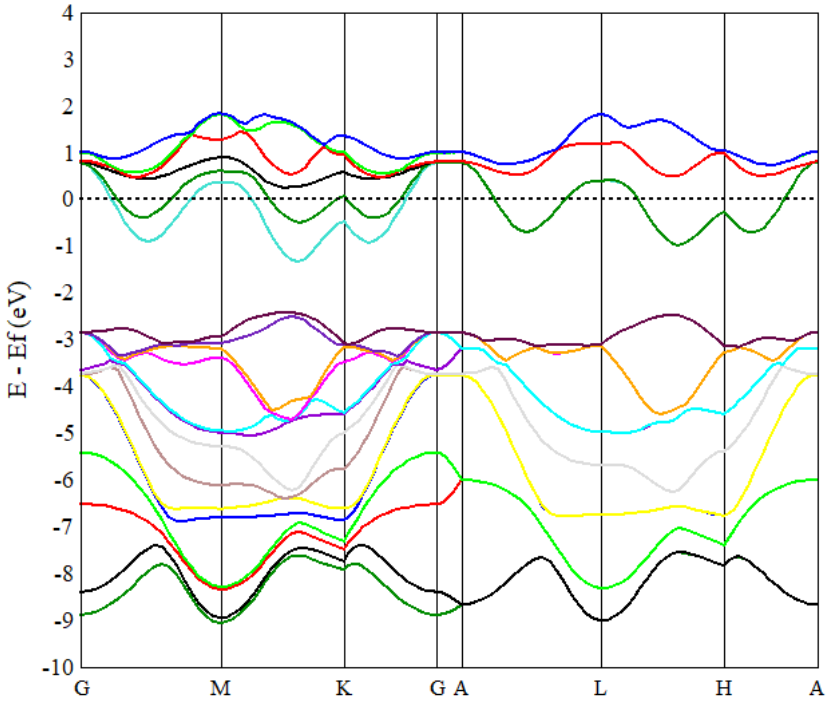

Figure 43. Band electronic structures of $LiMoS_2$.

Compared to the previous case, the only difference is the greater shift of the bands below the Fermi level. Like in the TiS_2 intercalated compounds, the variations that occur in the electronic structure of $Li_{0.50}MoS_2$ and $LiMoS_2$ may be due to a charge transfer from lithium to MoS_2.

3. Modelling the structural disorder in trigonal-prismatic coordinated transition metal dichalcogenides

3.1 Introduction

In this chapter it is investigated the disorder introduced in the structure of pristine MoS_2 because of the intercalation of lithium in the vdW gap between the S-Mo-S sandwiches. This insertion has obvious effects in varying the density of carriers and as discussed in section 2.5, the conduction properties of the material, that change from semiconductive to metallic. However, the presence of lithium has a further interesting effect, that is the introduction of structural disorder hindering the phonon transport and limiting the κ_L. Then, the chapter is devoted to a detailed analysis of the structural disorder in lithium-intercalated MoS_2.

Trigonal-prismatic coordinated TMDC are formed from stacked (chalcogen)-(transition metal)-(chalcogen) triple layers, where the chemical bond is covalent within the triple layers, while vdW forces are effective between the layers. Bonding is at the origin of the great interest of these compounds, as 2D materials are involved in applications ranging from catalysis, electronics, photoelectronic, sensors, batteries, and thermoelectricity. In this chapter the issue is addressed of modelling the structural disorder in multilayer TMDCs. The structural model takes into account stacking faults, correlated displacement of atoms, and average crystallite size/shape and is assessed by simulation of the XRD pattern and fitting to the experimental data relative to a powdered sample of MoS_2 exfoliated and restacked via lithiation. From fitting, an average size of about 50 Å, nearly spherical crystallites, and a definite probability of deviation from the fully eclipsed atomic arrangement present in the ordered structure, are determined. The increased interlayer distance and correlated intralayer and interlayer atomic displacement is attributed to the presence of lithium intercalated in the vdW gap between triple layers (Li/Mo molar ratio of about 0.06). The model holds for the whole class of

trigonal-prismatic coordinated TMDCs and is suitably flexible to take into account different preparation routes.

The literature on the structure of disordered systems is rooted in the early decades of the last century [184–186] but has received a great enhancement in the recent time frame from the recognition of the peculiar functional properties deriving from electronic confinement in 2D materials [187]. This renewed interest started with the pioneering paper on graphene by Novoselov *et al.* [188] which was followed by a huge scientific production, but involves today a plethora of different compounds characterized by a strong bond inside 2D structural units and by a weak interaction between them. Among this latter class, triple-layer TMDCs, constituted of a transition metal sheet (mostly from groups 4-7 and in particular Ti, Nb, Ta, Mo, W, Re) sandwiched between two chalcogen layers (S, Se, Te) and kept bound by covalent metal-chalcogen interactions are involved in applications ranging from catalysis, electronics, photoelectronic, sensors, batteries, thermoelectricity [188-190]. The 2D nature of these compounds can be exploited by suitable ways of preparing monolayer films, obtained by top-down procedures such as mechanical or liquid-phase exfoliation, or by bottom-up techniques, such as CVD or PVD.

The structure and defectivity of mono- or few-layer TMDC films were mostly investigated by spectroscopy, microscopy, and computational approaches [191–195]. A few papers report on structural analyses carried out by simulation of the total XRD powder pattern [196,197]; in particular, Pakharukova *et al.* [198] stress that the presence of a noticeable concentration of structural defects determines a significant size underestimation with respect to electron microscopy approaches.

Multilayer TMDCs can be obtained by various bottom-up procedures, mostly chemical [199–202], but also by top-down routes such as mechanical grinding of bulk samples or exfoliation-restacking. In the latter technique, the exfoliation step can be achieved by mechanical processing [203], or by intercalation of various organic or inorganic moieties in the vdW gap between the 2D TMDC bricks followed by suspension of the easily exfoliated phase in a suitable solvent; the successive restacking step can be achieved by drying the suspension and eventually baking [197]. The outcome of most of these procedures consists of a disordered stacking of the 2D metal-chalcogen slabs. Also, electrochemical [204] or vacuum heating

deintercalation can be a source of stacking disorder. A recent comprehensive review of the synthesis and characterization of nanostructured TMDCs is given by Phalswal *et al.* [205].

Spectroscopies and microscopies are exploited for the characterization of multilayer TMDCs as well, but several studies involving the careful analysis of diffraction patterns are also documented and give valuable and detailed information about the actual atomic arrangement of the investigated samples. In particular, are worth of citation: i. the early papers by Frindt and coworkers [196,206–208], which report EXAFS experimental analyses and numerical simulations of the XRD patterns of single, few layers and restacked MoS_2 and WS_2 samples, and ii. the atomic pair distribution analyses (PDF) performed on MoS_2 and WS_2 by different groups over a wide time span [209–213].

An overview of this literature shows that, according to the preparation routes and the exploited experimental techniques, different atomic arrangements are described, ranging from: i. metastable octahedral coordination in monolayers whereas the bulk specimens are trigonal-prismatic; ii. fullerene-like or multiwalled nanotubes keeping the local sheet arrangement of planar structures; iii. turbostratic stacking; iv. zig-zag chains of metal-metal bonds; v. stacking faults. A mixture of different sources of the disorder is often allowed.

This chapter, in particular, is focussed on trigonal-prismatic coordination in multilayered TMDCs, having as intensively investigated compounds MoS_2 and WS_2. The approach consists of the formulation of a general structural model, described in the next Section 3.3, accounting for structural disorder and size distribution; the simulation of the diffraction pattern and its fitting to experimental data (in Section 3.5). As an experimental counterpart (details on sample preparation and characterization techniques are given in Section 3.4), a specific sample of MoS_2 is investigated, obtained by dibutyl lithium reaction with ground commercial MoS_2, followed by exfoliation-restacking of 2D triple-layer units. In Section 3.6. the significance of some features of the model is discussed; Sections 3.7 and 3.8 deal with structural aspects described in the literature, and in particular with turbostratic (in Section 3.7) and octahedral arrangement (in Section 3.8).

3.2 The model

The description of the structural model of MoS_2 encompasses i. the stacking sequences of the S-Mo-S sandwiches; ii. the uncertainty in the relative position of atoms belonging to the same layer and different nth-neighbouring layers; iii. shape and size distribution of the crystallites; iv. simulation and fitting of the powder pattern.

3.2.1 Stacking sequences

The model assumes that the structural units of MoS_2 are S-Mo-S sandwiches stacked in disordered sequences, fulfilling the constraint of close packing between facing sulphur layers and keeping the same average spacing between the triple layers, irrespective of the close packing sequence. The coordination polyhedral are edge-sharing MoS_6 trigonal prisms, as depicted in Figure 44. The stacking of these units gives rise to the three-dimensional MoS_2 structure.

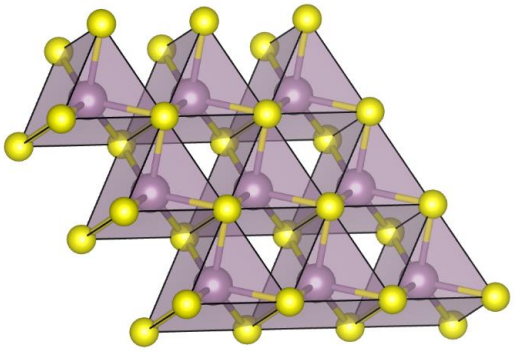

Figure 44. Two-dimensional network of edge-sharing MoS_6 trigonal prisms.

Figure 45 shows the available positions of sulphur and molybdenum with respect to the (**a**,**b**) axes of the reference hexagonal frame. According to the trigonal-prismatic coordination, the sulphur-molybdenum-sulphur atomic layers can respectively occupy, with reference to the cell depicted in Figure 45, the positions AbA, AcA, BaB, BcB, CaC, CbC, where the capital letters refer to sulphur and lower-case to molybdenum.

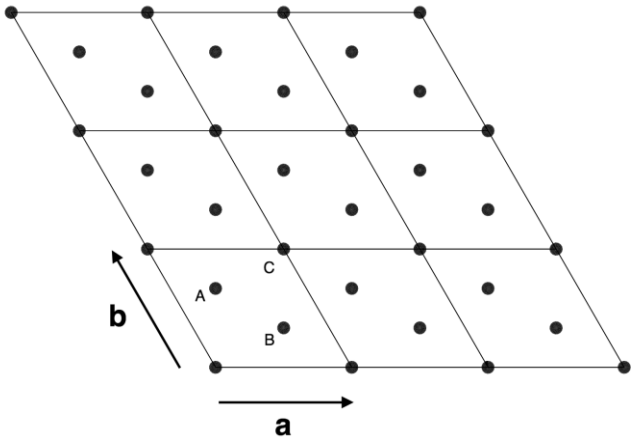

*Figure 45. (**a**,**b**) section of the MoS_2 hexagonal frame. The allowed Mo and S projections onto the (**a**,**b**) plane are indicated; for the sake of clarity, the metal sites are cited in the text with lower-case lettering.*

The ideal bulk structure of MoS_2 (*P63/mmc*) corresponds to the sequence AbA-BaB-... (i.e. AA' sequence, according to the formalism corresponding to fully eclipsed atoms [214–216]), but the AbA-BcB-CaC... polytype (i.e. space group *R3m* [217]), with partially staggered atoms (i.e. AB sequence [215]) is also described.

Due to the vdW weak interaction between neighboring layers, different synthetic routes result in similar diffraction patterns characterized by faulted stacking of the chalcogen-metal-chalcogen layers. This disorder has been associated to modification of electronic structure and to fine tuning of functional properties in a number of published papers.

The modelization of stacking faults was carried out within the formalism of Kakinoki & Komura [218], i.e. considering the stacking of the triple layers as a Markov chain, where the *n*-th step influences in a probabilistic sense the (*n*+1)-th event. Making reference to the position of metals and chalcogens drawn in Figure 45, the relevant stochastic matrix is defined in Equation 14

$$\mathbf{P} = \begin{bmatrix} & AbA & BcB & CaC & AcA & BaB & CbC \\ AbA & 0 & \alpha & \beta & 0 & \gamma & \delta \\ BcB & \beta & 0 & \alpha & \delta & 0 & \gamma \\ CaC & \alpha & \beta & 0 & \gamma & \delta & 0 \\ AcA & 0 & \delta & \gamma & 0 & \beta & \alpha \\ BaB & \gamma & 0 & \delta & \alpha & 0 & \beta \\ CbC & \delta & \gamma & 0 & \beta & \alpha & 0 \end{bmatrix} \quad (14)$$

where $\sum_j P_{ij} = 1$, so that the four parameters of Equation (14) are constrained with, for instance, $\delta = 1 - (\alpha + \beta + \gamma)$. The case γ=1 corresponds to the ordered structure in the *P63/mmc* space group.

The intensity equation worked out by Kakinoki & Komura [218] was modified to get the spherical average in the reciprocal space suitable to be fitted to the experimental data:

$$I_{klm}(q) = \sum_{i,j} f_i \, p_{ij}^m \, \mu\left(\mathbf{t}_{klm}^{ij}\right) \frac{sin2\pi q\left|\mathbf{t}_{klm}^{ij}\right|}{2\pi q\left|\mathbf{t}_{klm}^{ij}\right|} \quad (15)$$

where:

- the sums over *i* and *j* run over the six events heading the rows and columns of Equation (14).
- p_{ij}^m are the elements of the *m*-th power of **P**, $(\mathbf{P})^m$, which is still stochastic.
- f_i are the frequencies of existence of the *i*-th event, bound by the linear and homogeneous system $\sum_j f_j P_{ji} = f_i$; by symmetry, f_i=1/6.
- $\mathbf{t}_{klm}^{ij} = k\mathbf{a} + l\mathbf{b} + m\mathbf{c}$ are the distance vectors between an atom belonging to the *i*-th type triple layer and an atom belonging to the *j*-th, *m* steps ahead in the **c** direction; then, the index *m* is relative to the vertical component of the interatomic vector, while the indexes *kl* scan the horizontal component parallel to the (**a**,**b**) plane.
- $\mu\left(\mathbf{t}_{klm}^{ij}\right)$ is the multiplicity of the $\mathbf{t}_{klm}^{ij}$ interatomic distance, calculated as $\frac{1}{v}\int_V \mathbf{dr}\phi\left(\mathbf{r} + \mathbf{t}_{klm}^{ij}\right)\phi(\mathbf{r})$ [219], where *v* is the volume of the triple layer unit cell, *V* is the volume common to the shape function $\phi(\mathbf{r})$ ($\phi(\mathbf{r}) = 1$ inside

the crystallite, $\phi(\mathbf{r}) = 0$ outside), taking into account that chalcogens are twice the number of metals.

- $I_{klm}(q)$ represents the contribution to the total intensity coming from the interference, averaged over all the allowed *i*, *j* couples of layers, of two atoms joined by the distance vector $\mathbf{t}_{klm}^{ij}$.
- the overall scattering intensity (*vide infra*) is given by the sum of all terms like Equation (15), weighted by the respective atomic factors of the atoms joined by the $\mathbf{t}_{klm}^{ij}$ interatomic distance.

3.2.2 Size/shape

The possible shape anisotropy of the crystallites was taken into account assuming that the shape function $\phi(\mathbf{r})$ is relative to a spheroid [219], that is, an ellipsoid with two different axes, $r_{\parallel}$ parallel to the (**a**,**b**) plane and $r_{\perp}$ parallel to **c**. The model allows also for size distribution, if all the crystallites have the same shape, but for a proportionality factor; it is assumed that the size distribution is governed by a simple exponential law, so that the distance multiplicity is given by the weighted sum of terms corresponding to spheroidal crystallites from a minimum to a maximum size:

$$\mu_{AV}(\mathbf{r}) = \frac{1}{\eta}\sum_{i=1}^{\nu} R_i^2 exp[-\xi R_i]\mu_i(\mathbf{r}) \qquad (16)$$

where $R_i = \frac{i}{\nu}\left[r_{\parallel,max}^2 \cdot r_{\perp,max}\right]^{1/3}$, $\mu_i(\mathbf{r})$ is the distance multiplicity of the *i*-th allowed spheroid size, corresponding to $r_{\parallel,i} = (i/\nu) \cdot r_{\parallel,max}$ and $r_{\perp,i} = (i/\nu) \cdot r_{\perp,max}$, and $\eta = \sum_{i=1}^{\nu} R_i^2 exp[-\xi R_i]$; ν is the number of allowed spheroid sizes, and **r** represents the generic distance between atoms. Explicit mathematical form for **r** and μ_i is given above, in Section 3.3.1.

Size and stacking sequences are decoupled, that is, it is assumed that the probabilities defined in Equation (15) hold on the average for the whole sample, no matter of the size of crystallites.

3.2.3 Uncertainty in the relative position of atoms

As will be shown in the next section, the experimental evidence seems to suggest that the relative position of atoms is affected by an uncertainty and that this uncertainty propagates as a function of the distance; then, a correlated displacement of atoms from the ideal crystallographic positions is effective. The formalism, initially worked out by Hosemann [186] for polymeric materials and called "ideal paracrystal", was applied also to inorganic samples [220,221]. According to the theory, the mutual position of atom is not given by a delta function, but rather by a gaussian distribution, the width of which increases linearly with the distance between atoms:

$$\varphi_{\mathbf{t}_{klm}}(|\mathbf{r}|) = \sigma_{\mathbf{t}_{klm}}^{-3}(2\pi)^{-3/2} exp\left[-|\mathbf{r}|^2/2\sigma_{\mathbf{t}_{klm}}^2\right] \quad (17)$$

The model allows for the possibility that the *intra-layer* distribution could be different from the *inter-layer* one:

$$\sigma_{\mathbf{t}_{klm}} = \sigma_{\parallel} \cdot |\mathbf{t}_{klm}|/|\mathbf{t}_0|, \;\; m = 0 \quad (18a)$$

$$\sigma_{\mathbf{t}_{klm}} = \sigma_{\perp} \cdot |\mathbf{t}_{klm}|/|\mathbf{t}_0|, \;\; m \neq 0 \quad (18b)$$

where $|\mathbf{t}_0|$ is a unit reference length.
The Fourier transform of (26):

$$\Phi_{\mathbf{t}_{klm}}(|\mathbf{q}|) = exp\left[-|\mathbf{q}|^2\sigma_{\mathbf{t}_{klm}}^2\right] \quad (18)$$

enters as a multiplication factor in the intensity terms defined in Equation (15) [219-224].

3.2.4 The overall model intensity *I(q)*

The assembly of all the above-described features yields the total model intensity:

$$I(q) = \sum_{\kappa\lambda} \zeta_\kappa \zeta_\lambda \sum_{i,j} \sum_{klm} f_i \, p_{ij}^{m} \Phi_{\mathbf{t}_{klm}}^{ij,\kappa\lambda}(q) \, \mu_{AV}\left(\mathbf{t}_{klm}^{ij,\kappa\lambda}\right) \frac{sin2\pi q\left|\mathbf{t}_{klm}^{ij,\kappa\lambda}\right|}{2\pi q\left|\mathbf{t}_{klm}^{ij,\kappa\lambda}\right|} \qquad (19)$$

The sum over κ,λ runs over the different couples of atoms, Mo-Mo, S-S and S-Mo, considering the 2:1 stoichiometric ratio between sulphur and molybdenum; to avoid confusion with frequencies, the scattering factors are indicated with ζ instead of the traditional *f*.

3.2.5 Powder pattern simulation and fitting

The accelerated sum of the Debye series was finely treated by Cervellino *et al.* [225] to carry out the simulation of the powder pattern of ordered crystallites. In this chapter the approach of Cervellino *et al*. was adopted, but for a necessary modification to deal with the case of one-dimensional disorder. So, the above quoted accelerated convergence procedure was "sliced" in two dimensional sums of the type of Equation (15), each one corresponding to a fixed *m*-index value or, otherwise stated, to a given height jump. Despite this unavoidable complication, the CPU time was definitely viable. The fitting procedure was carried out by the package Minuit [226].

3.3 Experimental

A commercial MoS_2 sample (Alfa Aesar, 98%, -325 mesh) was milled in a high energy planetary mill (Fritsch, Poulverisette 6) using zirconia beads as grinding media and deionized water (Milli-Q) as solvent. The milling cycle includes 36 repetitions of 30 min for a total milling time of 18 hours. The milling speed was kept at 400 rpm, using a powder to beads volume ratio of 1:15. The obtained powder

was centrifugated at 6000 RPM for 20 min and vacuum dried at 160°C. The dried powder was sieved at 100µm to obtain the ground-dried sample.This ground-dried sample did not show the presence of secondary phases, while a definite reduction of the preferred orientation present in the fresh sample and a size reduction of about 50%, leading to an average size of 40 nm, were observed by X-ray diffraction (XRD). 8 mmol of the sample then reacted with 15 mL of a 1.6M solution of n-butyllithium in hexane under nitrogen atmosphere at room temperature for one week (molar ratio Li/Mo = 3), and the lithiated product was washed with hexane and dried under vacuum. The lithium content was determined with flame emission spectroscopy both directly on the solid (dissolved with hot concentrated sulphuric acid and hydrogen peroxide), and by difference from the washing solution, giving an effective Li/Mo molar ratio of about 0.06 in the lithiated solid.

To eliminate residual preferential orientations, which mostly enhance the (*00l*) reflections, the sample was mixed with amorphous silica powder. Different blendings were tested, until the diffraction intensity ratios between the (*00l*) and the (*hkl*) reflections reached a steady value at a weight dilution of 1:10. The XRD pattern was recorded with a Rigaku Miniflex 600 diffractometer equipped with a Si strip detector using Ni-filtered CuK_α radiation and an incident slit of 1.25° on the primary beam.

3.4 Results

Figure 46 shows the result of the fitting of the model to the experimental pattern, and Table 15 reports the values and the uncertainties of the structural parameters described in Section 3.3.

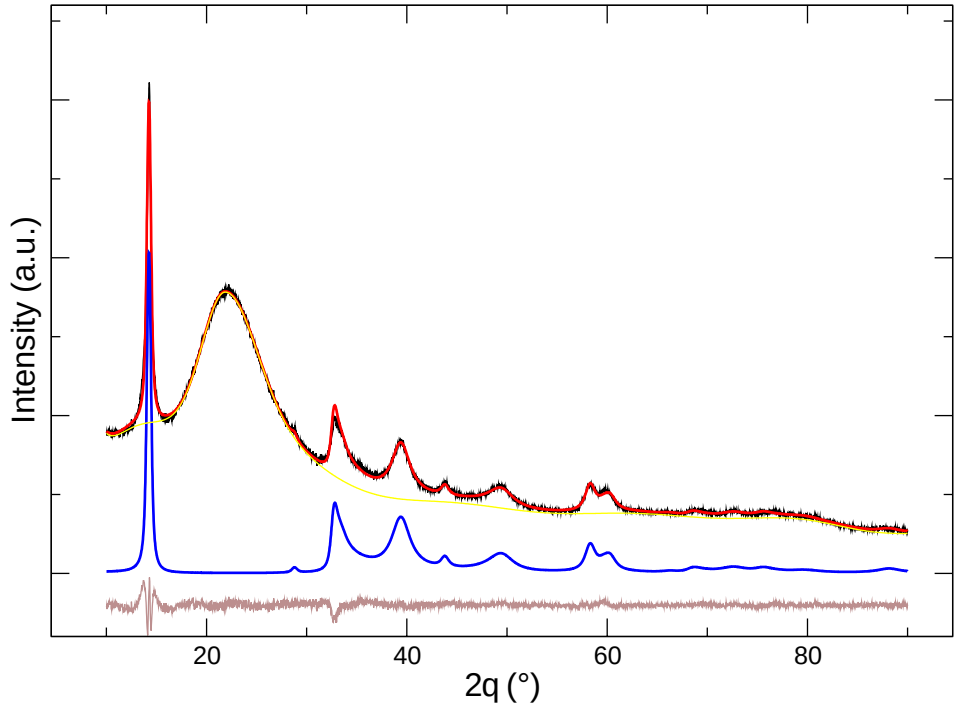

Figure 46. Fitting of the structural model to the XRD data of the exfoliated-restacked MoS_2 sample. Experimental, black; calculated, red; background, yellow; model, blue; residual, brown. The halo at 22° 2θ is due to the amorphous silica diluent.

Table 15. Refined parameters and uncertainties relative to the fitting of the model to the XRD data of the exfoliated-restacked sample of MoS_2. The goodness of fit was evaluated as $R_P = 100\left[\sum_i \left(y_{obs,i} - y_{calc,i}\right)^2 / \sum_i \left(y_{obs,i} - y_{back,i}\right)^2\right]^{1/2} = 12.6$

α †	β †	γ †	$\sigma_{\parallel}$ (Å) §	$\sigma_{\perp}$ (Å) §	ξ (Å) ◊	$r_{\parallel}$ (Å) ◊	$r_{\perp}$(Å) ◊	a (Å) #	c (Å) #
0.37(1)	0.16(1)	0.36(3)	0.0023(2)	0.0037(3)	0.057(1)	142(5)	151(3)	3.162(1)	6.190(2)

† *Defined in Equation (14). δ is not a fitting parameter, as it is bound to the condition that the sum of the rows of a stochastic matrix equals 1.*

§ *Defined in Equations (17), (18a), (18b).*

◊ *Defined in Equation (16).*

Hexagonal cell constants.

A non-negligible expansion of the interlayer spacing with respect to bulk MoS_2 amounting to 0.03 Å, according to the figure of 6.16 Å reported by Petkov *et al.* [227], is likely related to residual intercalated lithium (with a Li/Mo molar ratio about

0.06) in the vdW gap after the baking-restacking process. The inter- and intra-layer correlated displacement could also be ascribed to this intercalation, due to the reduction of Mo^{4+} and/or to local change of local Mo coordination [209,227]. The α, β, γ parameters reported in Table 15 confirm that the structure of the investigated sample is heavily affected by stacking disorder. The deviation from the value γ=1, corresponding to the ordered sequence of fully eclipsed atoms, points to a partially staggered atomic arrangement in the restacked sample. The average size is calculated as $R_{AV}(\mathbf{r}) = \frac{1}{\eta}\sum_{i=1}^{\nu} R_i^3 exp[-\xi R_i]$, yielding R_{AV} = 51±1 Å. Within the errors of $r_{\parallel}$ and $r_{\perp}$ reported in Table 15, the crystallites are roughly isometric.

3.5 Is the model oversized?

This section addresses the issue relative to the significance of all the features of the model and, in particular, the question whether the model is "oversized" as concerns the treatment of structural disorder. Figure 47 shows the simulated patterns relative to: *i.* the lattice constants and the shape/size parameters reported in Table 15, no disorder, with Miller indexes labels; *ii*. the same as item i. plus the stacking faults parameters gathered from Table 15; *iii*. the same as item i. plus the correlated displacement disorder quantified by the parameters reported in Table 15; *iv*. the fitting to the data with only correlated displacement disorder; *v*. the fitted pattern already drawn in Figure 46.

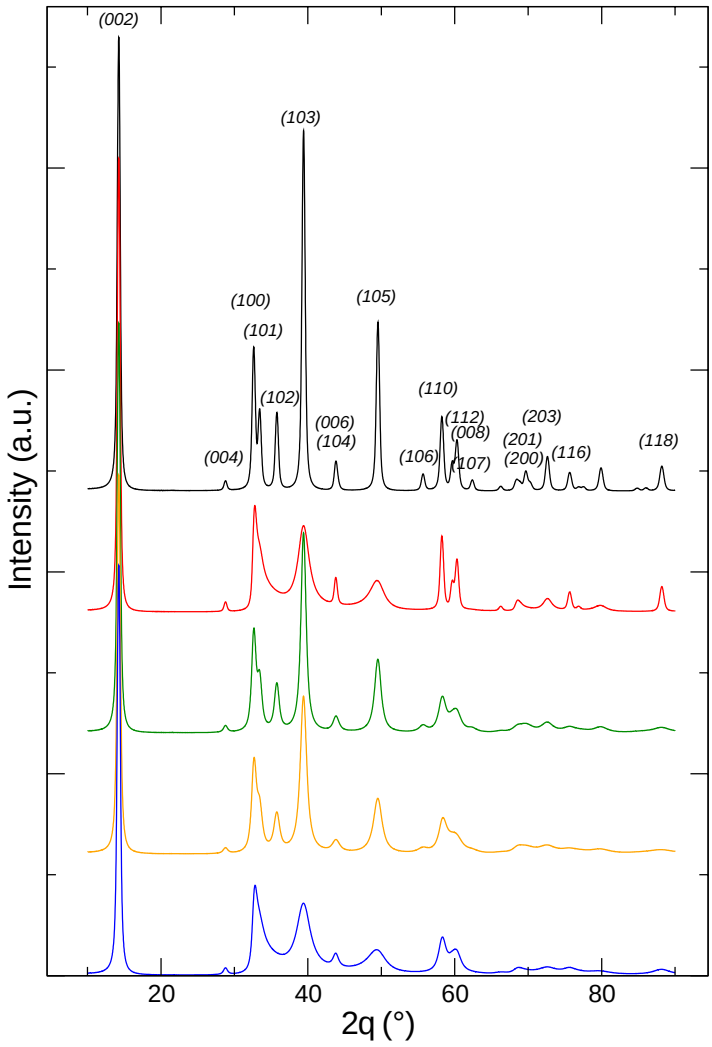

Figure 47. Simulated patterns for exfoliated-restacked MoS_2. From top to bottom: ordered (black trace), stacking faults only (red), correlated displacement only (green), best fit to the data with correlated displacement only (orange), fitting with both types of disorder (i.e. stacking faults and correlated displacement, blue).

Inspection of Figure 47 confirms [228] that stacking faults do not produce broadening of the peaks with Miller indexes (*00l*), (*hk0*) and of the reflections with $h+k=3n$. On the other hand, the correlated displacement uncertainty determines a progressive broadening of the diffraction peaks, increasing with the modulus of the scattering vector q. It is evident that the selective damping of the diffraction peaks induced by stacking faults produce the definite blurring of high intensity peaks, such as the

(*102*), (*103*) and *(105)*, which isn't so effectively obtained by the action of correlated displacement only. To further support this analysis, the fitting run assuming no stacking faults and only correlated displacement was also carried out, to check the possibility that allowing for stacking faults could underestimate the correlated displacement distribution. The fitting, clearly unsatisfactory, confirms that, within the proposed model, both stacking faults and correlated displacement should be allowed.

3.6 Turbostratic arrangement

A limiting case of stacking disorder in TMDCs layered structures is turbostratic stacking, proposed since the early papers by Frindt and coworkers [196,197] as a possible tridimensional arrangement, in analogy with turbostratic graphite. In an ideal turbostratic TMDC structure the S-TM-S layers are piled up parallel, but with a completely random relative position. The Frindt group simulations for restacked MoS_2 were sound, even if not completely suitable for the reported experimental data. Later, the turbostratic arrangement was taken into consideration by Mangelsen *et al.* [210] for WS_2 and by Bekx-Schürmann *et al.* [201] for MoS_2. These authors carried out a PDF analysis of the respective XRD data, allowing for stacking faults and small random displacements of the S-TM-S sandwiches parallel and perpendicular to the basal planes, concluding that both sources of disorder are necessary for a suitable fitting to the data. The question of turbostratic disorder in restacked WS_2 was addressed also by Petkov *et al.* [209] showing, by PDF analysis, that the nanostructured material undergoes a prismatic-trigonal to distorted-octahedral rearrangement of the tungsten coordination, giving rise to locally different S-W distances; based on this analysis, the turbostratic disorder was ruled out and a distortion within the S-TM-S sandwiches was allowed. Petkov and coworkers also observed that a similar analysis can be hardly extended to MoS_2, due to the higher instability of the metastable octahedral coordination in this compound.

It is clear that the finer details of preparation can result in quite different samples, and, in this respect, all the above cited analyses are based on specific experimental evidence coming also from spectroscopic data in addition to diffraction techniques.

Figure 48 reports the XRD simulation using the lattice parameters from Bekx-Schürmann *et al.* [201] and assuming, like these authors, a finite-width distribution in the mutual position of ideal trigonal-prismatic coordinated triple layers. Stacking faults were modulated by trial and error, in order to get a calculated pattern similar to those reported in Fig. 5 of that paper (Bekx-Schürmann *et al.* [201]). The most evident discrepancy with the reported data can be observed for the (118) peak, at about 87° 2θ (at 10.76° 2θ using λ=0.20728 Å), which is not blurred by stacking faults and only partially by interlayer correlated displacement. Consequently, it is argued that intralayer disorder is effective. It is also worth noting that, with respect to the fitting parameters reported in Table 15, the same overall pattern shape is obtained with $\alpha=\beta=0.27$, $\gamma=0.2$ and then by reducing, with respect to the refined parameters relative to our sample, the probability of the AbA-BaB sequence corresponding to fully eclipsed atoms along **c**. This trend is even more remarkable in the second simulation reported in Figure 48, showing the case $\alpha=\beta=0.33$, $\gamma=0.0$, and yielding a profile like the one reported in Fig.3b of the paper by Yang & Frindt [197].

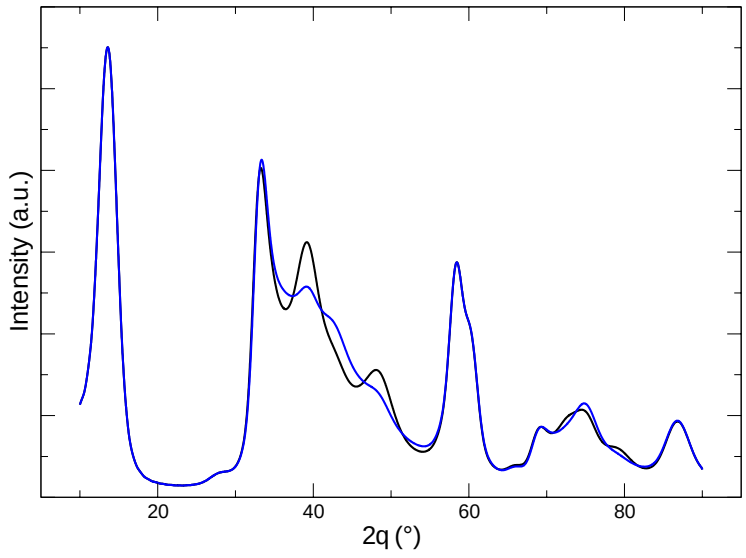

Figure 48. Simulated patterns of MoS_2 with two combinations of disorder parameters. 1) $\alpha=\beta=0.27$, $\gamma=0.2$ (black trace); 2) $\alpha=\beta=0.33$, $\gamma=0.0$ (blue trace). In both cases, a=3.155 Å, c=6.4 Å.

3.7 Octahedral arrangement

The octahedral coordination of Mo in MoS_2 was observed as a consequence of intercalation with different guests [227–231] or as a result of special preparation techniques [232–234]; the variety of reported structural details is likely related to preparation routes and to materials composition.

The possibility of octahedral coordination is investigated in this study by allowing two kinds of S-Mo-S sandwiches with, respectively, prismatic, and octahedral coordination, each one characterized by its own thickness and then by two different spacings, $|\mathbf{c}_P|$ and $|\mathbf{c}_O|$, along the direction perpendicular to the S-Mo-S layers. The 12x12 transition matrix, analogue of **P** in Equation (15), taking into account the prismatic-prismatic (AbA-AbA like), the octahedral-octahedral (AbC_AbC), the prismatic-octahedral (AbA-AbC) and the octahedral-prismatic (AbC-AbA) sequences, is shown in Equation (16).

$$\mathbf{P} = \begin{bmatrix} & AbC & BcB & CaC & AcA & BaB & CbC & AbC & BcA & CaB & AcB & BaC & CbA \\ AbC & 0 & \alpha & \beta & 0 & \gamma & \delta & 0 & \eta & \eta & 0 & \eta & \eta \\ BcB & \beta & 0 & \alpha & \delta & 0 & \gamma & \eta & 0 & \eta & \eta & 0 & \eta \\ CaC & \alpha & \beta & 0 & \gamma & \delta & 0 & \eta & \eta & 0 & \eta & \eta & 0 \\ AcA & 0 & \delta & \gamma & 0 & \beta & \alpha & 0 & \eta & \eta & 0 & \eta & \eta \\ BaB & \gamma & 0 & \delta & \alpha & 0 & \beta & \eta & 0 & \eta & \eta & 0 & \eta \\ CbC & \delta & \gamma & 0 & \beta & \alpha & 0 & \eta & \eta & 0 & \eta & \eta & 0 \\ AbC & \varepsilon & \varepsilon & 0 & \varepsilon & \varepsilon & 0 & \phi & \chi & 0 & \psi & \omega & 0 \\ BcA & 0 & \varepsilon & \varepsilon & 0 & \varepsilon & \varepsilon & 0 & \phi & \chi & 0 & \psi & \omega \\ CaB & \varepsilon & 0 & \varepsilon & \varepsilon & 0 & \varepsilon & \chi & 0 & \phi & \omega & 0 & \psi \\ AcB & \varepsilon & 0 & \varepsilon & \varepsilon & 0 & \varepsilon & \psi & 0 & \omega & \phi & 0 & \chi \\ BaC & \varepsilon & \varepsilon & 0 & \varepsilon & \varepsilon & 0 & \omega & \psi & 0 & \chi & \phi & 0 \\ CbA & 0 & \varepsilon & \varepsilon & 0 & \varepsilon & \varepsilon & 0 & \omega & \psi & 0 & \chi & \phi \end{bmatrix} \quad (16)$$

It is clear that the overall number of involved probability parameters is too large for a significative refinement and therefore a drastic shortcut was imposed by assuming that the prismatic-octahedral and octahedral-prismatic sequences are governed by a unique parameter (respectively indicated as η and ε in Equation 16). The different spacings, $|\mathbf{c}_P|$ and $|\mathbf{c}_O|$, involve that the vertical distance between two S-Mo-S layers is a function of the height jump (that is, of the integer *m* in the interatomic distance vector $\mathbf{t}_{klm} = k\mathbf{a} + l\mathbf{b} + m\mathbf{c}$) and of the path between the terminal layers [43]; due to the huge number of intermediate steps combinations, for large *m* this vertical

distance tends asymptotically to $m|\bar{\mathbf{c}}| = m|f_P\mathbf{c}_P + (1-f_P)\mathbf{c}_O|$, where f_P is the fraction of prismatic layers, no matter of the type of terminal layers.

Fitting of this "prismatic-octahedral" model yields an only marginal improvement, with a decrease of the goodness-of-fit parameter to R_P=11.9 with respect to the above quoted R_P=12.6. The refined parameters $|\mathbf{c}_P| = 6.193(1)$ and $|\mathbf{c}_O| = 6.189(3)$ are fairly similar, while the fraction f_P =0.8499(2) denotes, as expected, a large predominance of prismatic coordination. Figure 49 reports the obs-calc patterns and Figure 50 the simulated pattern obtained by excluding the effect of correlated disorder. Some further comments about the occurrence of interatomic distance uncertainty are supported by the simulations reported in Figure 51.

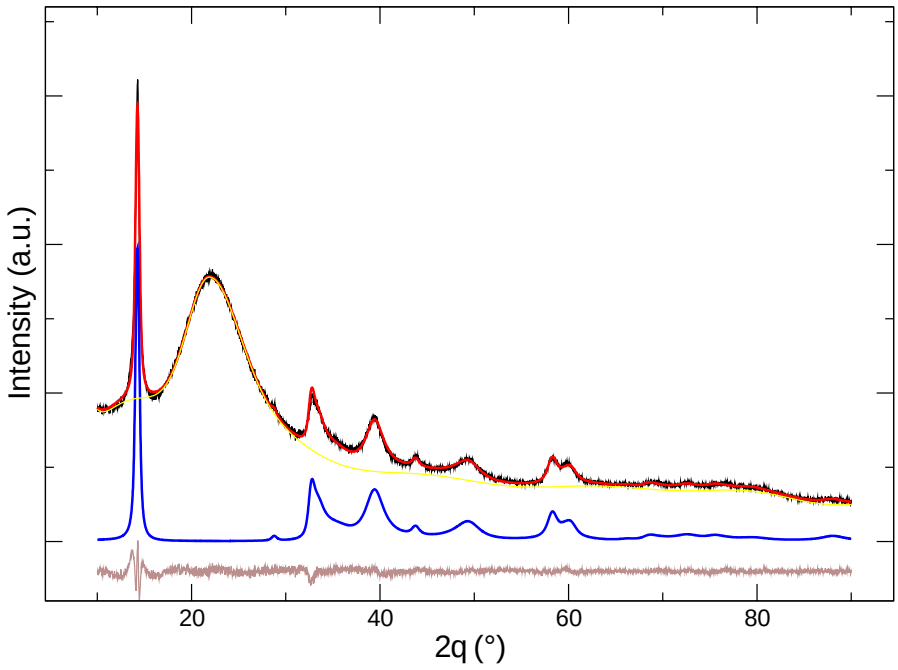

Figure 49. Fitting of the prismatic-octahedral model to the XRD data of the exfoliated-restacked MoS_2 sample. Experimental, black; calculated, red; background, yellow; model, blue; residual, brown.

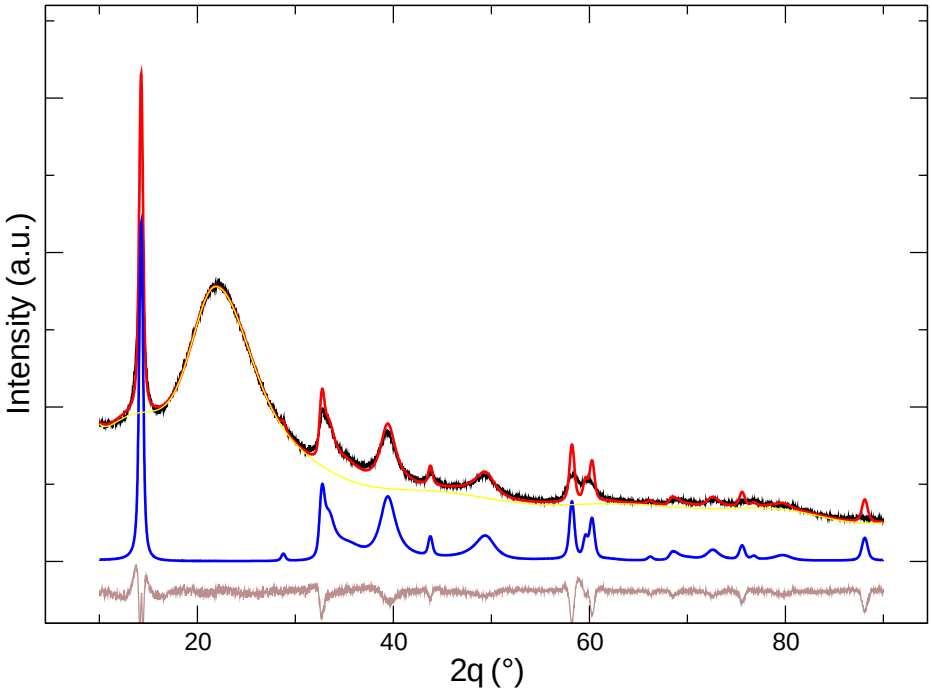

Figure 50. Simulation of the prismatic-octahedral model to the XRD data of the exfoliated-restacked MoS_2 sample. Experimental, black; calculated, red; background, yellow; model, blue; residual, brown. The correlated interatomic distance uncertainty is eliminated.

Figure 50 shows that the presence of two different S-Mo-S thicknesses is not the main source of interatomic distance uncertainty with consequent blurring of the high-angle lines. This evidence was confirmed by simulations involving a small (f_P=0.5) frequency of prismatic layers and a quite large difference between prismatic and octahedral thicknesses ($|\mathbf{c}_P|$=6.19 Å and $|\mathbf{c}_O|$=6.23 Å): Figure 51 shows that the components of the total XRD pattern corresponding to different height jumps between *m*-neighbouring sandwiches (that is, the value of the integer *m* in the interatomic distance vector $\mathbf{t}_{klm} = k\mathbf{a} + l\mathbf{b} + m\mathbf{c}$) remain sharp despite the large difference between the prismatic and octahedral thicknesses if the interatomic distance correlated uncertainty is not considered (blue traces) whereas, if this source of disorder is considered (red traces), the blurring of the intensity

components increases as a function of the scattering angle and of the distance (*i.e.* at increasing *m*) between the S-Mo-S sandwiches. On the contrary, the effect of blurring the high-angle lines determined by the presence of two different thicknesses decreases at increasing *m*, because at high *m* values the spacing between *m*-neighbouring layers tends asymptotically to the unique $m|\bar{\mathbf{c}}| = m|f_P\mathbf{c}_P + (1 - f_P)\mathbf{c}_O|$ value, no matter of the terminal layers.

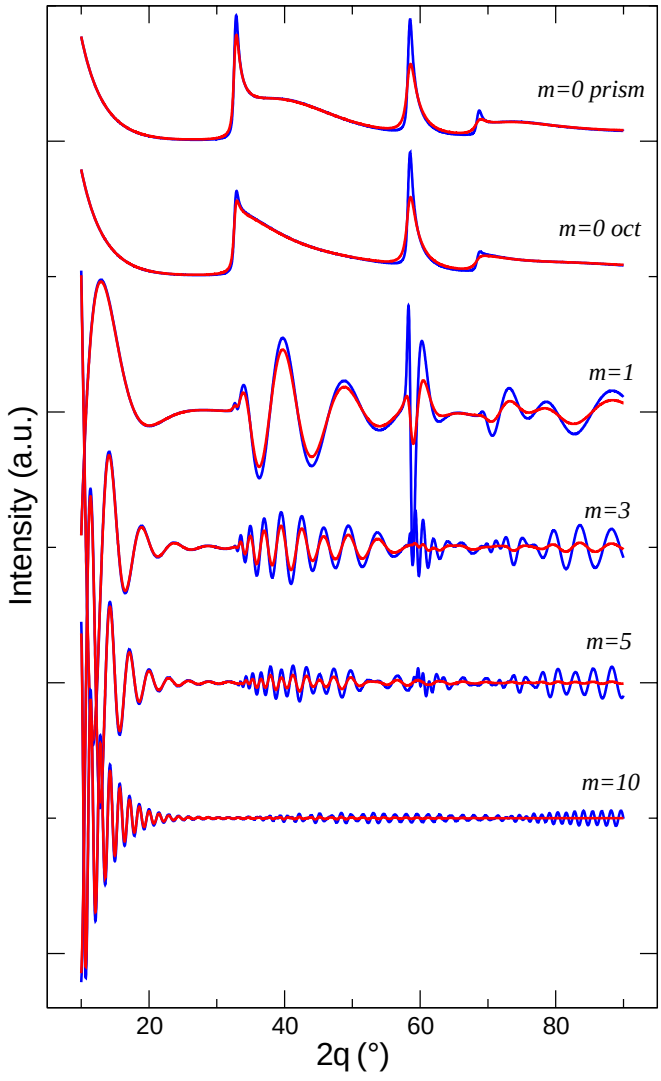

Figure 51. Components of the total XRD pattern corresponding to different height jumps (see text) between S-Mo-S sandwiches. Blue traces, no interatomic distance correlated uncertaint;, red traces, with correlated uncertainty. For m=0 (self-scattering of the S-Mo-S units) the distinct contributions of prismatic and octahedral sandwiches are drawn.

For a critical appraisal of the prismatic-octahedral model the following items should be considered:

- the assumption that the S-Mo-S sandwiches are thoroughly prismatic or octahedral is clearly very strong and, taking into account that the octahedral arrangement is locally induced by the intercalated lithium ions (see, e.g., [209]), should be related to a lithium segregation in some of the vdW gaps, rather than a sparse distribution of lithiums;
- this latter distribution of intercalant, producing local perturbations in the S-Mo-S sandwiches, looks like more realistic, and could also explain why correlated atomic displacements (see Figure 50) are still necessary to get a good fitting;
- partial substitution of sulphur with oxygen, producing MoS2-xOx compositions, can be obtained by different synthesis routes involving heath treatments in oxygen-rich environment [235,236]. For relatively thick (~6 μm) films [235], the so-obtained materials showed reduced cell constants with respect to pure MoS_2 and noticeable structural disorder as well. However, considering the presence of residual lithium detected by the chemical analysis and the restacking procedure carried out under vacuum, it seems feasible to attribute the observed correlated displacement to the reduction of Mo by intercalated Li [227,237], giving rise to local octahedral rearrangement of molybdenum coordination and to a structural distortion propagating to the neighboring structural units;
- overall, it can be concluded that the model presented in Sections 3.3 and 3.5 is able to give a detailed picture of the average structure of the investigated material. The prismatic-octahedral model described in this section does not produce a significative improvement while, for a thorough structural characterization, integration of the XRD long-range analysis with local techniques such as PDF and/or XAS should be suitable.

3.8 Conclusions

The XRD patterns reported in literature and relative to nanosized trigonal-prismatic coordinated TMDCs seem to agree that the main sources of structural disorder are both intralayer and interlayer, while ideal Turbostratic disorder should be ruled out. The "prismatic" model presented in this chapter treats the correlated displacement of atoms within the formalism of the "ideal paracrystal" [186]. Accordingly, the width of the Gaussian distribution governing the mutual displacement of atoms is a linear function of the distance. It is likely that this uncertainty, even if roughly effective in accounting for the quoted experimental evidence, could be more finely modelized, in particular by allowing for different coordination, such as the distorted octahedral proposed by Petkov and coworkers [209], which could be at the origin of a correlated displacement ranging beyond the first neighbors. In the case of the sample investigated by us, residual lithium surviving in the structure after baking-restacking of monolayer dispersion could influence either the local metal coordination, or the stacking sequence of triple layers, or both. Also, the "prismatic-octahedral" model described in Section 3.8 needs correlated displacement to get a good fitting to the data. This fact, and the only marginal improvement obtained with respect to the "prismatic" model, induced us to conclude that, rather than sequences of all-prismatic and all-octahedral sandwiches, intercalated lithium ions determine the above quoted perturbation of the prismatic coordination of molybdenum.

Stacking faults are anyhow necessary to get satisfactory data fittings. This kind of disorder has been recognized by several other authors (just to cite the most recent papers: Niefind *et al.* [200]; Bekx-Schürmann *et al.* [201]; Sanikop & Sudakar [202]) but, to my knowledge, this is the first attempt to quantify it on statistical grounds. The model described in Section 3.3 can be useful for the structural analysis of prismatic TMDCs such as WS_2 and the respective selenides of Mo and W. The extension to octahedral TMDCs is also straightforward.

PART 3: INTERCALATION OF 2D CHALCOGENIDES BY ORGANIC MOIETIES

4. Long-term stability of TiS_2-alkylamine hybrid materials

4.1 Introduction

One of the most interesting prospect applications of hybrid inorganic-organic TE materials is probably the harvesting of the metaboli c heat produced by the human body to feed energy into portative devices such as computers, mobile phones, monitors of vital functions and so on. A necessary requisite for the involved TE materials is the flexibility, to suitably shape the energy harvester to the body. This characteristic is typically achieved by hybrid TE materials. On the other hand, issues relative to the synthesis routes and the long-term stability of these materials should also be taken into consideration.

Intercalation compounds of TMDCs, where neutral organic molecules (NOM) are inserted in a regular or less ordered fashion, have been the subject of numerous studies [162-163,165-166]. However, many relevant aspects, such as stoichiometry, chemical stability, thermal inertness, polymorphic occurrence, or the nature of MX2-NOM bonding, are still not completely clarified.

Among layered TMDCs, titanium disulfide is a promising candidate for n-type thermoelectrics owing to some remarkable properties: it is chemically stable, mechanically manageable [238], environmentally benign and, most relevant for availability and cheapness, contains earth-abundant elements (Ti and S). In this chapter it is shown that amine intercalated-TiS_2 prepared by a simple mechanochemical process is prone to chemical decomposition due to sulphur exsolution, and that the presence of molecular oxygen is likely to mediate the decomposition reaction. In particular, it is proposed by computational analysis of the possible reaction pathways that Ti-N adducts are formed because of amine

groups substituting for S vacancies on the internal surfaces of the S-Ti-S layers and that the reaction with ambient oxygen leads to the formation of an undesired S8 crystalline phase.

4.2 Materials and Methods

4.2.1 Synthesis

TiS_2 powder (99.8% metals basis, Alfa Aesar, Haverhill, MA, USA) and liquid n-hexylamine (99%, Sigma-Aldrich, St. Louis, MO, USA, labeled as HA in the following), combined in a 1:4 molar ratio, were mixed in an agate mortar and manually ground with a pestle for 30 min (Figure 52). This synthesis was found to be highly reproducible. After grinding, the volume of the powders expanded significantly, indicating that the intercalation was effective, with an evident color change from black to shiny brown. The intercalated hybrid is labeled as TiS_2/HA below. The pertinent chemical reaction then reads:

$$TiS_2\,(s) + x\,[n\text{-}C_6H_{13}NH_2\,(l)] \longrightarrow TiS_2(C_6H_{13}NH_2)_x\,(s) \qquad \text{with } x \approx 1 \qquad (17)$$

This material was found to be unstable if exposed for a prolonged time to environmental conditions. Indeed, after 12 months storage without specific precautions, TiS_2/HA had gone through macroscopic changes. For this reason, the effect of aging on this sample was further investigated. Two batches of freshly prepared TiS_2/HA were left for 1 week in different environments: one in air and the other in inert atmosphere (N_2), both in the dark and at room temperature.

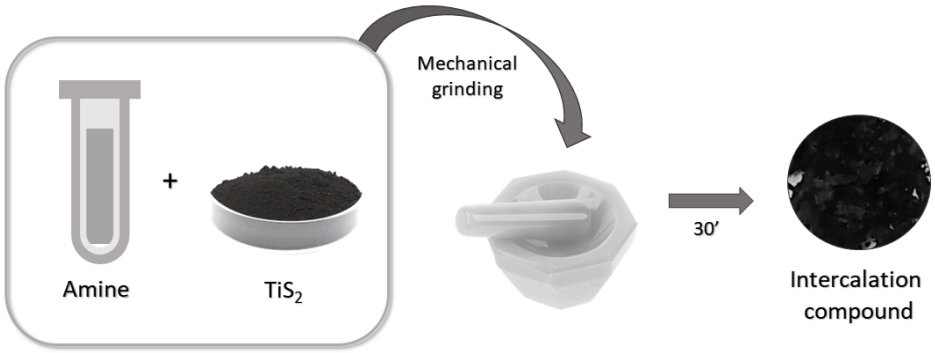

Figure 52. Scheme of the intercalation process through mechanochemical synthesis.

4.2.2 Experimental Characterization

X-ray powder diffraction (XRD) data were acquired in Bragg–Brentano geometry on a Rigaku Miniflex 600 (Tokyo, Japan) or on a Bruker D8 Advance diffractometer (Billerica, MA, USA), both working in vertical scan using Ni-filtered Cu Kα radiation. XRD traces were analyzed with Topas [239], for peak hunting whole pattern profile analyses, in the structureless (Le Bail) or Rietveld modes (see Figures 53-55 for the full description of such analyses).

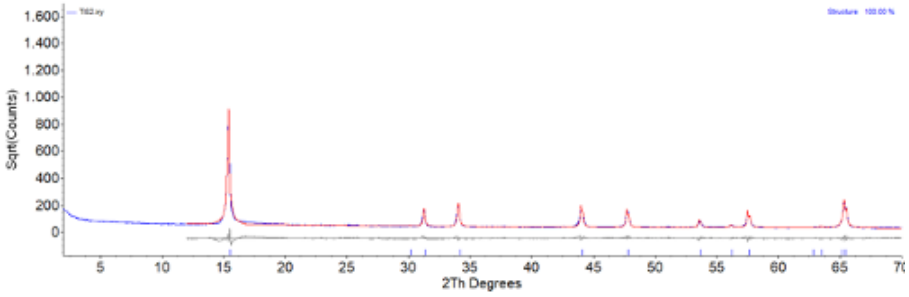

Figure 53. Rietveld refinement of the pristine TiS_2 material. Y-axis is in square root scale. All experimental peaks belong to the titanium disulphide structure. XRD modeling required the insertion of a strong textural component, with the preferential orientation parameter r001 = 0.42 (in March-Dollase desctiption,).

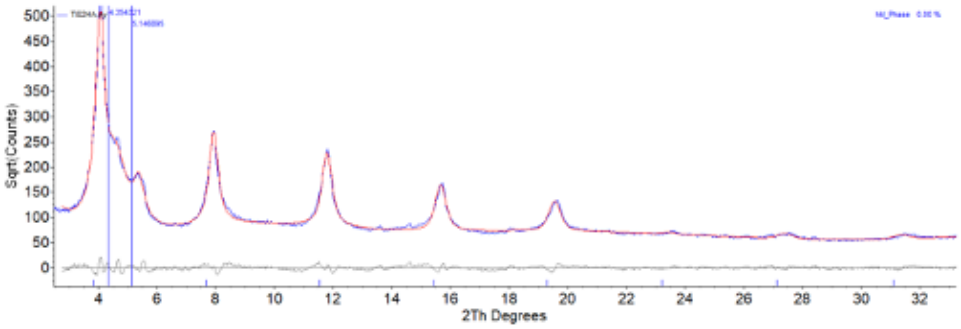

Figure 54. Structureless 1D Le Bail refinement of TiS_2/HA hybrid with 00l peaks only. Y-axis is in square root scale. These experimental peaks are typical of an inflated titanium disulphide structure, with a significantly large interlayer spacing (23.0 Å, vs. 5.7 Å of the original TiS_2 powders). Two additional peaks (vertical lines at 4.35-5.14°) are attributed to minor contaminants characterized by different packings of HA molecules in the interlayer space, or, more likely, to a slightly lower amount of intercalated HA moieties.

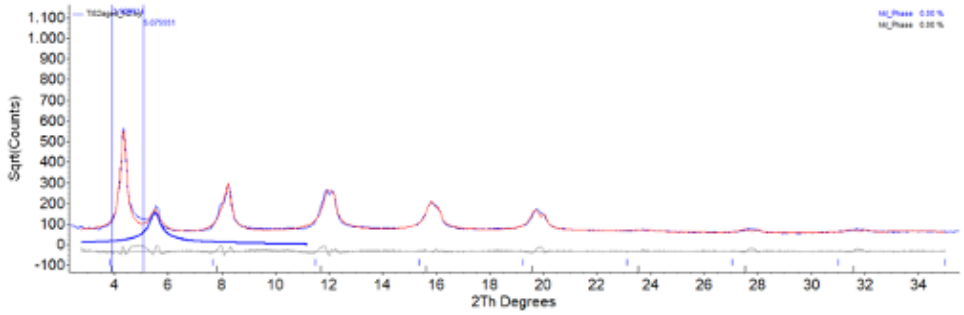

Figure 55. Structureless 1D Le Bail refinement of TiS_2/HA (N_2). Y-axis is in square root scale. No significant differences with respect to TiS_2/HA. are evident. As explained in the main text, the spurious peak highlighted by the blue trace is attributed to different HA packing (or content).

Thermogravimetric traces under nitrogen were acquired from room temperature to 700 °C using a TA Q500 thermogravimetric analyzer (New Castle, DE, USA) with a Pt sample holder. Micro-Raman spectra were recorded on a Horiba Raman Evolution spectrometer employing a confocal microscope with 50× long working distance and a laser with an excitation wavelength of 633 nm. Imaging by scanning electron microscopy (SEM) was performed in secondary electron mode using FEI Versa 3D (Lincoln, NE, USA) using a 10 kV acceleration voltage.

4.2.3 Computational Methods

Periodic ab initio DFT + U calculations were carried out with the PWscf package in the Quantum ESPRESSO 6.7 suite [240]. TiS_2 hybrids were modeled starting from the P-3m1 trigonal parent structure and enlarging the c lattice parameter to accommodate amines. All structures were fully relaxed, and energies were calculated using a k-space sampling over a dense 8 × 8 × 4 grid. The pseudopotentials and kinetic energy and density cut-offs were taken from the standard solid-state pseudopotential efficiency library (SSSP) [241,242]. All calculations were performed using the generalized gradient approximation [243] and the PBEsol exchange-correlation functional [244]. The value of Hubbard U parameter for the Ti atom was set to 3 eV [245]. The vdW interlayer interactions were considered using Grimme's D2 dispersion correction [246,247].

4.3 Results and Discussion

The macroscopic evidence of materials swelling during synthesis clearly indicated that hexylamine could be rapidly incorporated into TiS_2 by a simple mechanochemical synthetic method. This unsophisticated method was indeed quantitative and could be repeated many times with the same outcome, providing robust information on its reproducibility. The structural changes were easily followed by acquiring XRD data from the final product. In this sense, XRD was first used in its qualitative (i.e., fingerprinting) mode, and when later used in a quantitative way, it allowed the determination of the axial d-spacings of the intercalated materials and for assessing either the presence of contaminant residues or the (unexpected) formation of elemental sulphur upon sample degradation. Specifically, in the pristine TiS_2 solid, where Ti^{4+} ions are sandwiched between two sulfide layers, the 001 peak, corresponding to the stacking periodicity, falls near 15.7° (i.e., 5.69 Å). After 30 min grinding, when the macroscopic alterations exhibited by the powders (liquid amine absorbed, volume increment, and color change) indicated that the intercalation of hexylamine into TiS_2 occurred, XRD was used to monitor the changes in the interlayer distance between adjacent S-Ti-S

sheets. In the TiS_2/HA species, the 001 peak in the XRD pattern (the strongest one in the traces shown in Figure 56) shifted from 15.7° to 4.1°. This implies an enormously increased (4×) separation between layers (21.6 Å) compared with that found on the pristine TiS_2 (5.69 Å), confirming HA intercalation.

It is worth noting that the stacking sequence in polymorphs and polytypes of intercalated TiS_2 can be different and is normally addressed by the occurrence of superstructure peaks, here not observed. However, since diffraction peaks were detected along only one reciprocal space rod (00l), this technique may be fully blind to polymorphs occasionally sharing the same d-spacing along c. Thus, it cannot be excluded that the TiS_2 layers in the intercalated hybrids are slightly offset in the xy plane.

Appraisal of c-axis expansion (ca. 15.9 Å) can safely allow to conclude that HA was embedded into the TiS_2 lattice, forming a bilayer structure. Since the estimated length of a single HA molecule, in its common all-trans conformation, H-bonded to S and vdW radii-corrected, is ca. 11.5 Å, the limited increase of the c-axis value suggests that the intercalated molecules possess a measurable inclination in the vdW gap of TiS_2, being 44° the estimated angle: $\sin{-1}(15.9/(2 \times 11.5)) = 43.7°$ (Figure 57). The DFT computational analysis provided geometry optimization of the HA location and orientation, eventually leading to an inclination of 40.0°, in very good agreement with the purely geometrical consideration set above. Density and geometrical considerations also indicate that 100% filling of the interlayer separation requires a stoichiometric TiS_2/HA formulation (one amine per TiS_2 unit formula), which, inter alia, would provide a cross-section area of ca. 20.0 $Å^2$, like that found in the orthorhombic all-trans polyethylene crystal phase [248].

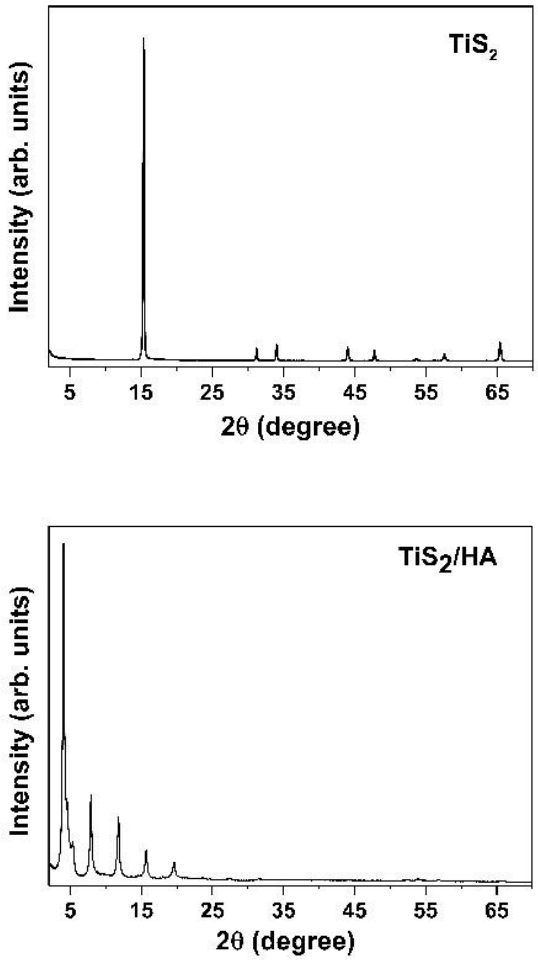

Figure 56. XRD patterns of (a) pristine TiS_2 and (b) TiS_2/HA.

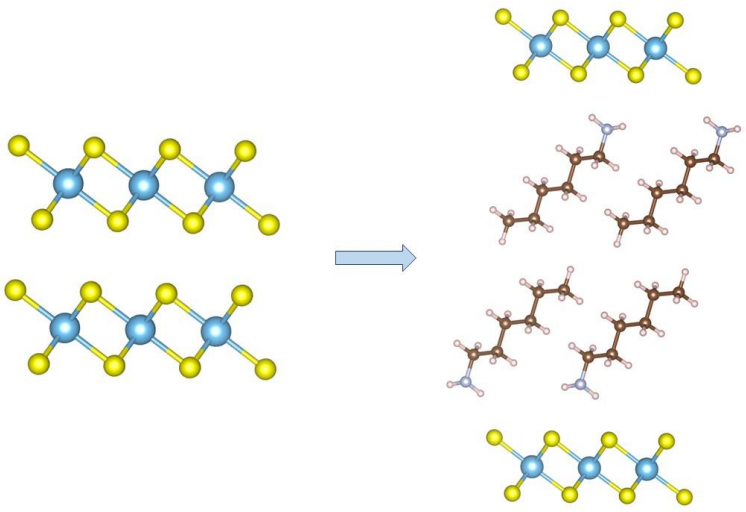

Figure 57. Left: Crystal structure of pristine TiS_2. Right: Proposed crystal structure of TiS2/HA, containing one HA molecule per TiS_2 formula unit.

Thermogravimetric studies (TGA) were performed to estimate the quantity of hexylamine in the inorganic matrix, through calculation of the molar coverage fraction (as mol/mol TiS_2), defined in Equation 18

$$\frac{\Delta\%_{org} \times MM(TiS_2)}{MM(HA) \times \left(100 - \Delta\%_{org}\right)} \tag{18}$$

where $\Delta\%_{org}$is the weight loss at 250 °C due to the organic moieties, and MM are the molar masses.

The weight loss of pristine TiS_2 was 3.36%, which was subtracted from $\Delta\%_{org}$. To obtain a reproducible result, the sample was prepared and subjected to TGA analysis thrice.

The average weight loss of the organic component was 43.06 ± 0.26%. Then, the exact stoichiometry of the intercalated system sample was $TiS_2(HA)_{0.833}$, not far from the TiS_2(HA) formula used as a model for the DFT simulations (vide infra).

After 12 months of aging in the dark at environmental conditions, the XRD pattern of powders of TiS_2/HA evidenced the limited stability of this intercalated material. Moreover, the formation of new crystalline phases was clearly observed. Indeed, jointly with residual TiS_2/HA, elemental sulphur was formed in its low-temperature/low-pressure orthorhombic polymorph (Fddd space group [249]). The complete Le Bail/single peak and Rietveld refinement plot for such sample, which contains TiS_2/HA, an unknown contaminant and crystalline sulphur, is shown in Figure 58.

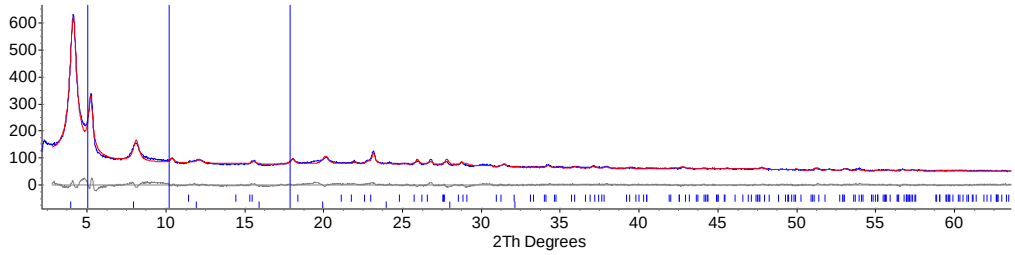

Figure 58. XRD pattern of twelve months-aged TiS_2/HA, showing the partial degradation of the intercalated material with the formation of crystalline sulphur.

Data modelling of the polyphasic of the polyphasic TiS_2/HA sample was performed by a hybrid approach comprising Rietveld refinement of rhombic sulphur and 1D structureless Le Bail refinement of the TiS_2/HA species. Blue trace: observed data; red trace, simulated pattern. Difference plot (in grey) and peaks markers, for sulphur and 00l reflections belonging to the TiS_2/HA crystal phase (blue ticks), are drawn at the bottom. The three spurious peaks highlighted by the blue vertical lines are attributed to different HA packing (or content) and/or to unknown contaminants.

A puzzling and open question, however, remains: what is the fate of titanium atoms? As anticipated, sulphur exsolution is accompanied by the formation of an unknown and partially crystalline contaminant (see blue vertical lines in Figure 58). The few uninterpreted diffraction peaks do not match any titania polymorph, nor could they be related to any other reasonable reaction product, such as those presented in the computational study discussed below, with the obvious substitution of NH_{3-n} residues with $CH_3(CH_2)_5NH_{2-n}$ ones (n = 0, 1, 2). Additionally, the large incoherent scattering raising the overall background level suggests that non-crystalline components are present (amorphous titania and its congeners [250], to mention a few).

Further evidence of sulphur demixing is given by Raman spectroscopy. Figure 59 shows the Raman spectra of three samples: pristine TiS_2 and TiS_2/HA (in the 200–500 cm^{-1} range) and aged TiS_2/HA (20–500 cm^{-1}). As expected, the Raman spectrum of the as-prepared TiS_2/HA is very similar to that of pristine TiS_2, while the aged TiS_2/HA hybrid exhibits many more signals due to sulphur exsolution.

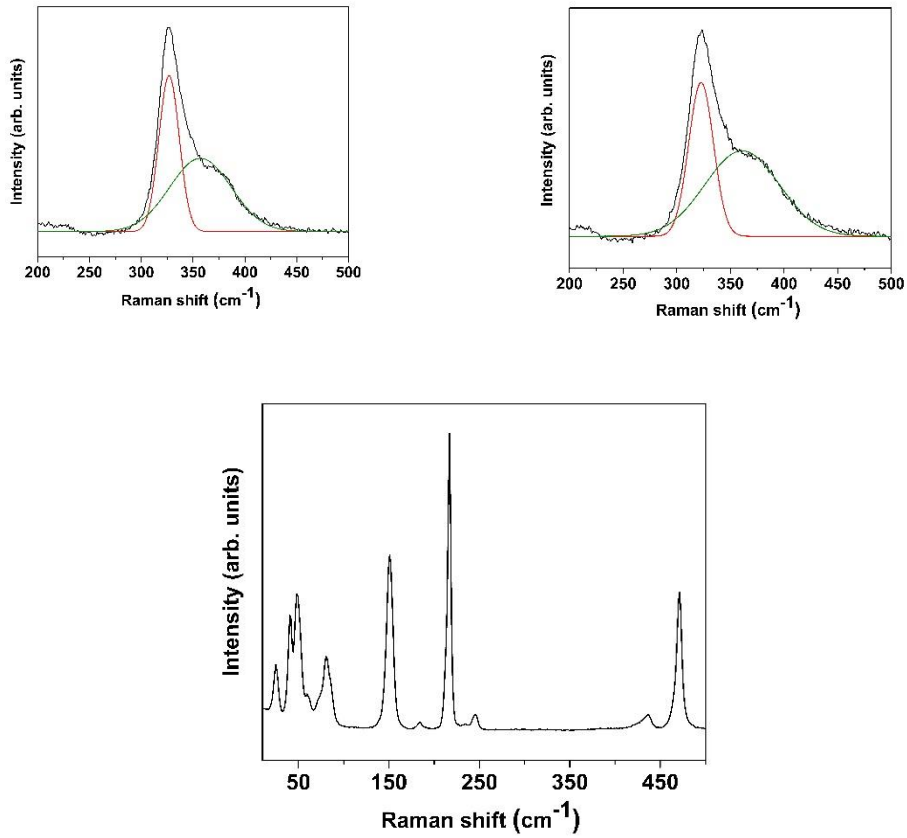

Figure 59. Micro-Raman spectra of (a) pristine TiS_2; (b) TiS_2/HA; (c) aged TiS_2/HA. In panels (a) and (b), the deconvolution of the Raman peaks with two components is shown.

The phonon modes at the Γ-point of the reciprocal space can be probed by Raman and IR spectroscopies. The primitive cell of TiS_2 consists of two chalcogen atoms and one metal atom with trigonal prismatic coordination, with the optical normal modes of vibration A_{1g}, E_g (Raman active), A_{2u}, and E_u (IR active). The experimental Raman spectrum was then interpreted through simulation of the active modes (Table 16).

Table 16. Vibrational modes of TiS2 calculated by DFT+U simulations.

Mode	Raman shift (cm^{-1})
$\mathbf{E_u}$	162.45
$\mathbf{E_g}$	233.10
$\mathbf{A_{1g}}$	321.23
$\mathbf{A_{2u}}$	361.10

The calculated Raman shifts are in very good agreement with the experimental ones. In particular, the Raman-active mode out of the plane (A_{1g}) is measured at 326.9 cm^{-1} for the pristine system, and 322.7 cm^{-1} for the intercalated one, confirming that the simulation captures well the electronic structure of the layered compound. A high-energy shoulder peak located at ~360 cm^{-1}, labelled Sh in the literature, is evident in the Raman spectra as an additional component (shown in Figure 60, TiS_2 and TiS_2/HA). Although this peak position matches the calculated frequency of the A_{2u} mode, it cannot be ascribed to this vibrational mode, the symmetry of which (A_{2u}) makes it only IR active. The physical origin of this shoulder has been subject to several interpretations in the literature, but no consensus has been reached to date [251–253]. Significantly, the presence of intercalated HA between the Ti-S layers does not affect the vibration modes in the measured range (see Figure 60).

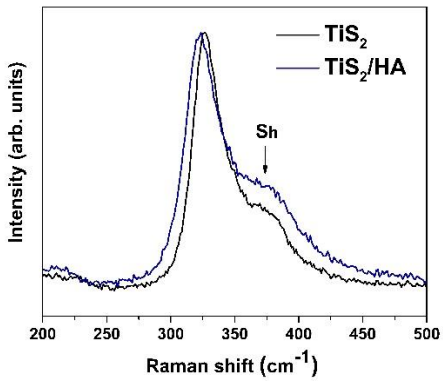

Figure 60. Comparison between the Micro-Raman spectra of pristine TiS_2 (black) and of the intercalated TiS_2/HA hybrid (blue).

An interesting aspect of the change brought about by the intercalation process is the morphological evolution of the sample with time, evident at both the macroscopic and the microscopic scales. As Figure 61 shows, pristine TiS_2 is a fine and dry black powder, while TiS_2/HA is a brown sticky powder, probably because of residual (not intercalated) hexylamine. Due to progressive material degradation, after 2 months, TiS_2/HA turns almost grey, and 1 year later, a yellow powder is found instead. The morphology of TiS_2, freshly prepared and aged (in air) TiS_2/HA hybrids, was also investigated using SEM imaging (Figure 62).

The SEM images of the intercalated compounds (both fresh and aged) show a substantial modification of the TiS_2 morphology. In pristine TiS_2, the lamellar shape of the crystals is evident, but it fully disappears in the freshly prepared TiS_2/HA hybrid, demonstrating that the mechanical treatment induces a severe morphological change, where a simple topotactic HA insertion does not maintain crystal size and shapes, it being accompanied by a complete lamellar disruption. Estimation of the average crystal domain lengths (along c) from the peak broadening of XRD data confirms that from micrometer-sized TiS_2 crystals, coherent domains of average size as low as 40 nm are formed in TiS_2/HA. On the other hand, there is no substantial microscopic modification upon aging, despite the occurrence of sulphur exsolution (with coherent isotropic domains of about 50 nm) and partial sample degradation. The hybrid structure, obtained by intercalation of the HA within the TiS_2 lattice, remains stable even after partial sulphur elimination. The hypothesis is confirmed by the XRD pattern reported above in Figure 58, as the persistence of the 001 peak of the intercalated compound is the dominating signal also upon material aging.

To pinpoint the driving force behind the decomposition of TiS_2/HA, and a possible mechanism for sulphur exsolution, the enthalpy variations were calculated relative to several possible reactions (ΔH_r, as $E_{(products)} - E_{(reactants)}$) with the DFT + U scheme described above. As is standard practice in this kind of simulations, the difference in total energy of products and reactants is taken as an approximation of the enthalpy of reaction.

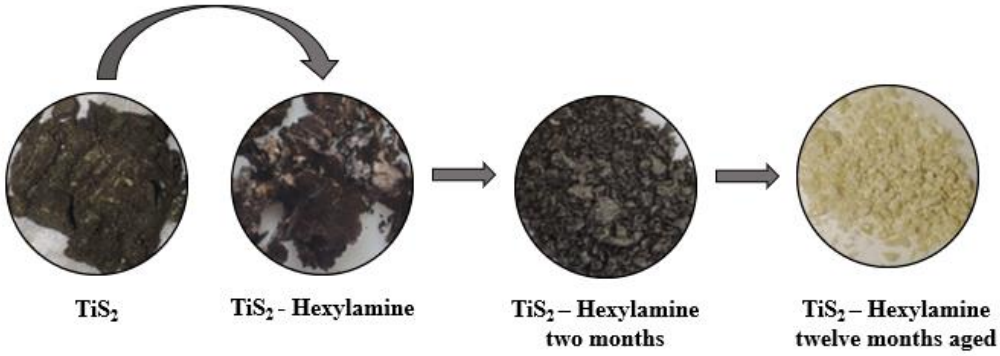

Figure 61. Macroscopic morphological and colour changes of TiS_2/HA.

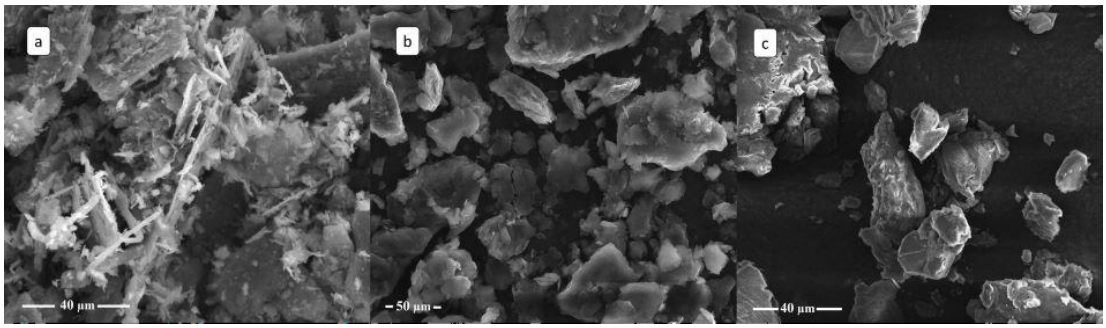

Figure 62. SEM images of a) pristine TiS_2; b) fresh TiS_2/HA; c) aged TiS_2/HA.

Initially, different sulphur-deficient TiS_2 superstructures were modelled. Three progressively larger supercells were constructed, with a corresponding dilution of sulphur vacancies. These ideal structures are synoptically depicted in Figure 63. As shown in Table 17, the enthalpic cost for the formation of a sulphur vacancy decreases as the cell size increases, but in all cases, the formation of such vacant sites is never energetically favoured per se. Using a simple linear extrapolation of the ΔH_r with $1/n$ plot (for the Ti_nS_m formulation), the energy required to form an infinitely diluted (neutral) S-vacancy in TiS_2 at the bulk limit can be estimated to be ca. 2.2 eV.

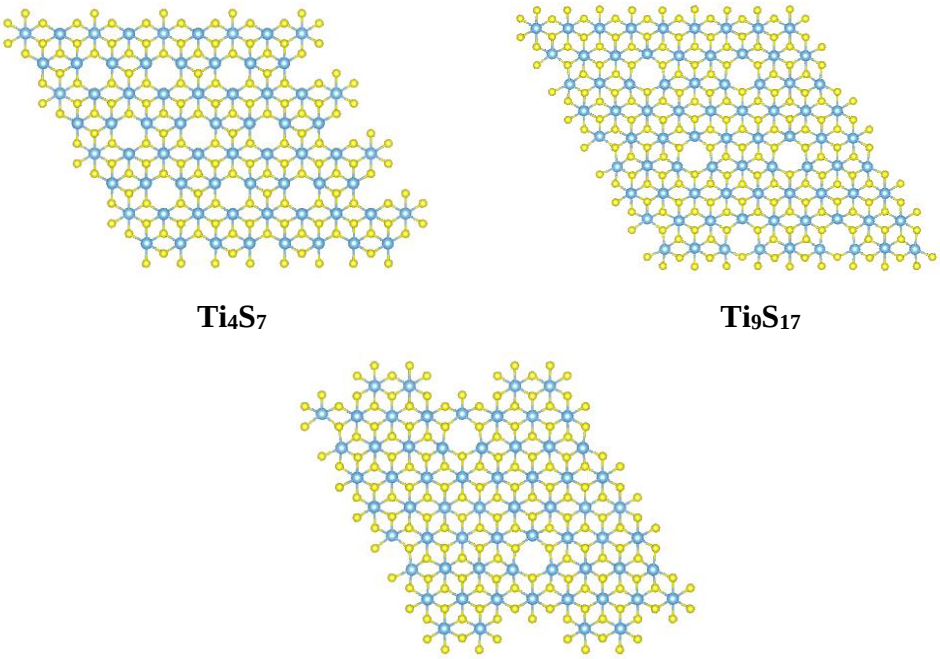

Figure 63. Top view of the different TiS_2 supercells used in the DFT modelling, all with periodic sulphur vacant sites.

Table 17. Formation of sulphur defects in TiS_2 at different concentrations (down to 0.03 at%). Extrapolation to an infinitely diluted vacant site leads to 2.2 eV, which is the energy required to eliminate one single (neutral) S atom from bulk TiS_2.

Reaction	ΔH_r (eV)
$Ti_4S_8 \rightarrow Ti_4S_7 + S$	3.14
$Ti_9S_{18} \rightarrow Ti_9S_{17} + S$	2.71
$Ti_{16}S_{32} \rightarrow Ti_{16}S_{31} + S$	2.43

Once the stability of pristine TiS_2 was quantitatively confirmed, to understand and interpret the experimentally observed spontaneous intercalation of HA, two consecutive steps were considered: (i) the formation of the TiS_2/HA hybrid and (ii) sulphur exsolution therefrom. To reduce computational costs, the intercalation, within TiS_2, of simple amine molecules (using ammonia and methylamine instead of HA) (Table 18) was investigated, using an idealized coverage of one nitrogen atom per four titanium ions (see Figure 64). The calculations were then based on

2×2 TiS_2 supercells with a single-side N-substitution. The intercalation reaction was mediated by moisture as amines or ammonia were used as aqueous solutions.

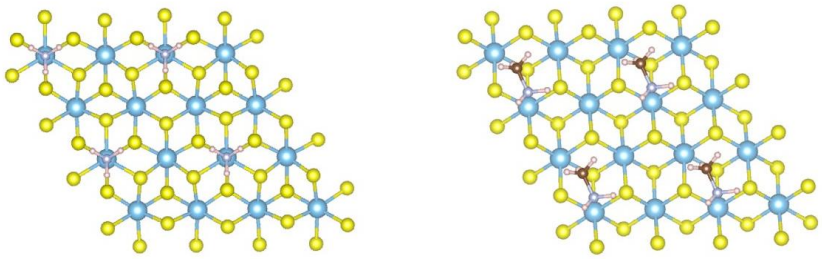

$Ti_4S_8NH_3$ **$Ti_4S_8CH_3NH_2$**

Figure 64. [001] view of NH_3 and CH_3NH_2 molecules adsorbed onto a TiS_2 slab containing 16 metal atoms. Nitrogen atoms interacts vertically with the Ti atoms of the TiS_2 surface, with N…Ti distances of around 2.25 Å.

Table 18. Reaction energy of TiS_2 intercalation compounds with either aqueous ammonia or aqueous methylamine.

Reaction	ΔH_r (eV)
$Ti_4S_8 + NH_4^+ + OH^- \rightarrow Ti_4S_8NH_3 + H_2O$	-2.93
$Ti_4S_8 + CH_3NH_3^+ + OH^- \rightarrow Ti_4S_8CH_3NH_2 + H_2O$	-1.75

That the intercalation reaction, observed experimentally for hexylamine, is energetically favoured is here confirmed by the simulated reaction energies, which are negative for both ammonia and methylamine cases. Once these adducts are formed, one sulphur atom is lost and nitrogen from the amine replaces it, with the formation of a Ti-N interaction. The fact that the NH_3 molecule interacts favourably with Ti, replacing S in its position, suggests that the Ti-N bond formation may drive S exsolution. For this reason, a few different possible reactions were tested, all involving the formation of defective TiS_2 slabs where amine groups carrying one to three H atoms actively interact with open Ti sites near a sulphur vacancy. Some of these complexes are shown in the case of ammonia (Figure 65), where the S atom is replaced by N. A similar situation is obtained in the case of methylamine.

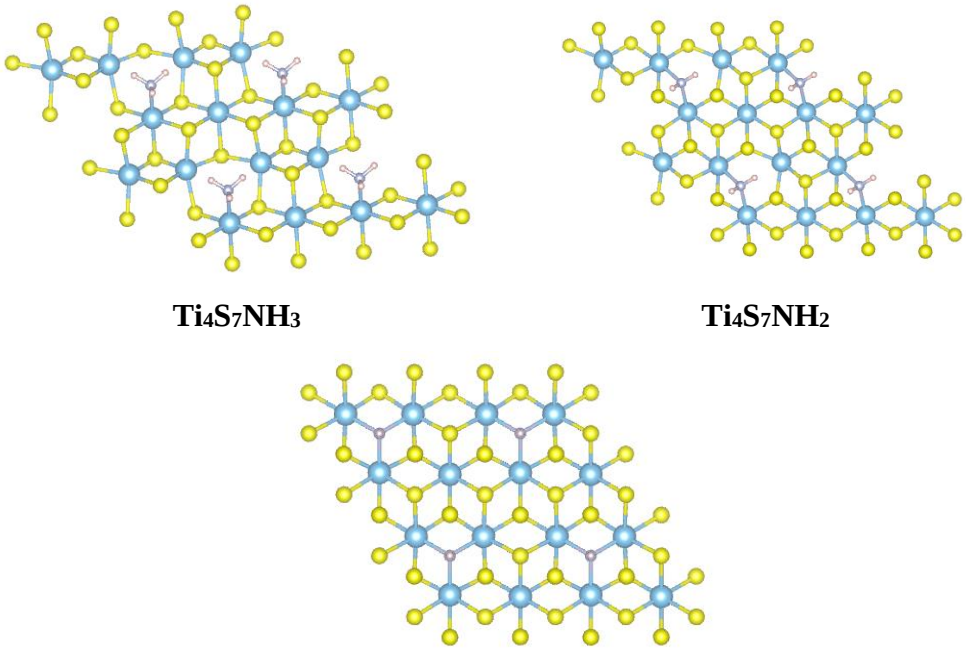

Figure 65. Top view of the nitrogen-containing Ti-S slabs formed by the loss of S atoms, substituted by ammonia molecules. In the last panel, all H atoms are eclipsed by N atoms, as N-H bonds lie perpendicular to the plane of drawing.

The last row in Table 19 indicates that the substitution of S by N is probably mediated by the action of molecular oxygen. In other words, the intercalated TiS_2/amine compounds seem to undergo sulphide oxidation to elemental sulphur, accompanied by a structural change in which Ti-N bonds are formed. In particular, the imido Ti_4S_7NH structure, where N is bound to three Ti sites, appears to be the most stable. Such μ3-NH coordination geometry on three Ti ions should not surprise, as it was found in a number of polynuclear organometallic complexes and, more paradigmatically, also in the highly symmetric [Ti(NH)(Cp*)]4 cubane (Cp* = tetramethyltrimethylsilylcyclopentadiene) [254].

Table 19. Reaction energy of the formation of Ti-N bonds arising from the exsolution of S and its substitution with the (deprotonated) ammonia molecules.

Reaction	ΔH_r (eV)
$Ti_4S_8NH_3 \rightarrow Ti_4S_7NH_3 + S$	1.51
$Ti_4S_8NH_3 \rightarrow Ti_4S_7NH_2 + S + ½\ H_2$	1.47
$Ti_4S_8NH_3 \rightarrow Ti_4S_7NH + S + H_2$	1.76
$Ti_4S_8NH_3 + ½\ O_2 \rightarrow Ti_4S_7NH + S + H_2O$	-0.83

However, it should be noted that all four reactions reported in Table 19 are in principle consistent with the available experimental evidence (exsolution of crystalline sulphur). The impossibility of verifying experimentally which is the true path to sulphur elimination (which likely occurs very locally without the formation of a clearly distinguishable crystalline phase) makes uncertain the nature, stoichiometry, and structure of the newly formed Ti/S/N product.

In order to quantitatively assess the effective charge transfer between N and Ti, the electron densities (in the form of Bader charges [255,256]) of pristine TiS_2 and different Ti-N complex supercells were compared (Table 20). By comparing bound structures with varying amounts of H atoms, it is seen that the Ti-N charge transfer is more and more effective as the amine group loses hydrogen atoms and forms stronger bonds with titanium: the Ti electron density decreases, and the N/H electron density increases.

Table 20. Bader charges of TiS_2 supercell and the Ti-N supercells formed via sulphur exsolution and substitution with nitrogen. The number of electrons explicitly included in the calculation is indicated for each element.

	Ti_4S_8	$Ti_4S_7NH_3$	$Ti_4S_7NH_2$	Ti_4S_7NH
Ti (10)	10.23	10.27	10.20	10.13
S (8)	6.89	6.99	6.95	6.92
N (7)	-	6.30	6.39	6.43
H (1)	-	0.55	0.58	0.59
Total Ti/S	96.00	90.05	89.46	88.97
Total ammonia	-	7.95	7.54	7.03
Total	96.00	98.00	97.00	96.00

To experimentally test the hypothesis that the structural change (and material decomposition) of TiS_2/HA was a consequence of exposure to molecular oxygen, a newly prepared batch of TiS_2/HA was kept under inert atmosphere, while another batch was kept in air for comparison (both in the dark and at room temperature, for 1 week). Figure 66 compares the XRD patterns of these two samples. The absence of crystalline sulphur in the case of TiS_2/HA kept in inert atmosphere is the experimental confirmation of the proposed reaction pathway, where O_2 actively participates in sulphur elimination.

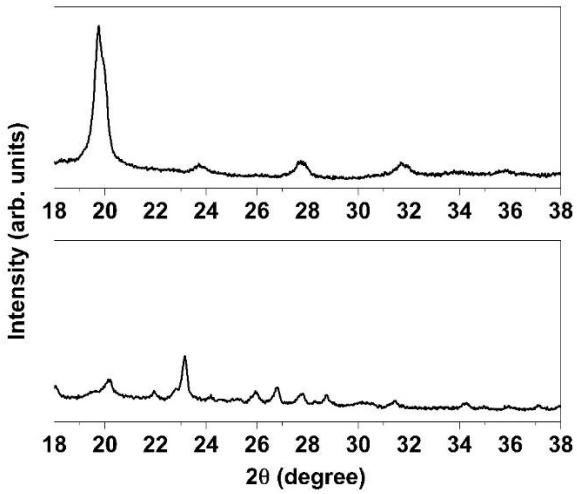

Figure 66. XRD patterns of TiS_2/HA (N_2) (top) and TiS_2/HA (air) (bottom), showing that sulphur exsolution only occurs by exposure to molecular oxygen.

4.4 Conclusions

This chapter reports about the experimental evidence of limited stability in ambient conditions of hexylamine-intercalated titanium disulphide, a material that has recently attracted interest for prospected TE applications. X-ray powder diffraction and Raman spectroscopy clearly show the formation of crystalline sulphur at the expense of the layered TiS_2/hexylamine compound. Different degradation mechanisms were tested by *ab initio* periodic DFT calculations on a TiS_2/NH_3 model system, suggesting that TiS_2 reacts with molecular oxygen, resulting in Ti-N adducts, where N resides in lieu of S vacancies, with the subsequent formation

of elemental sulphur and water. A comparison of the aging of TiS_2/HA in the presence or the absence of oxygen further corroborates the proposed mechanism since prolonged storage in inert atmosphere does not result in the degradation of the intercalated material. Since the reported findings point to a limited stability in air of such hybrid systems, appropriate actions taken to minimize exposure to oxygen in practical applications should be devised for TMDCs to be used in environmental conditions. While this appears to be a severe limitation for their wide usage, similar issues have been recently solved for oxygen- and moisture-labile hybrid materials (lead halide perovskites, above all [257]), which are deposited within thin layers of nonpermeable, and optically transparent, plastic films.

5. *Ab-initio* transport properties calculation of the hybrid superlattices hexylamine-TiS_2 and adamantylamine-TiS_2

5.1 Introduction

This chapter tackles the issue of the design of new hybrid inorganic-organic TE materials based on the TiS_2 inorganic scaffold. In the existing scientific literature, the only organic moieties taken into account for insertion in TiS_2 are the family of linear amines. On the other hand, the flexibility of the hybrid compounds and the (hopefully good) TE functional properties could be achieved, at least in principle, with different intercalating organic molecules. So, this chapter reports on the computational simulations relative to hexylamine (HA) intercalated TiS_2 and of another hybrid TiS_2-based material, obtained by intercalation in the TiS_2 scaffold of adamantylamine (ADA), a molecule that, like HA, has a terminal amine group and a similar overall hindrance but, with respect to HA, displays a more compact shape that, in particular, involves a limited variability of orientation with respect to the structure of the inorganic host.

The electronic properties of TiS_2, a layered solid constituted by the stacking of covalently bound S-T-S slabs weakly interacting with vdW forces, and of TiS_2 intercalated with hexylamine (TiS_2/HA) have been studied using density functional methods. The simulations of the transport properties agree with the available experimental data for pristine TiS_2 and TiS_2/HA. The computational approach is then extended, *mutatis mutandis*, to the prediction of the TE behaviour of TiS_2 intercalated with adamantylamine (TiS_2/ADA), a hybrid organic-inorganic compound not yet synthesized. Based on the electronic properties of a range of swelled TiS_2 structures obtained by artificially expanding the width of the vdW gap between the S-Ti-S slabs, it is argued that the improvement of TE performance of TiS_2 could be achieved by a wide variety of organic intercalated moieties.

Among the environmentally friendly ways of producing electricity, TE technology is attracting growing interest in recovering waste heat from various sources of a

thermal gradient, but also for the opportunity to collect the heat produced by the human body. In fact, TE devices powered by the heat produced during metabolic processes are now considered a promising source of energy for wearable electronics, such as fitness trackers, smartwatches, and medical sensors.

The performance of a TE material is evaluated through the $ZT = S^2\sigma T\kappa^{-1}$, where T is the temperature. The power factor ($PF = S^2\sigma$) characterizes the electron energy conversion capability, while κ characterizes heat leakage. Then, an ideal TE material must exhibit high σ, high S, and low κ [258]. It is difficult to combine all these features together, as the total thermal conductivity $\kappa = \kappa_e + \kappa_l$ is bound to the electronic conductivity κ_e by the Wiedemann-Franz law $\kappa_e = \sigma LT$, where L is the Lorenz number. Therefore, the research on new TE materials tackles the somewhat puzzling issue of minimizing κ and keeping a suitable electronic conductivity, a goal that is pursued by acting on the lattice component κ_l of κ. At present, good, and reliable performances are achieved at low and medium temperatures by devices based on Bi_2Te_3, displaying *ZT* values around 1 at 400 K [106]. On the other hand, several high-performance TE materials present drawbacks such as toxicity, scarcity, and high price, that should be overcome by broadening the possible composition range [279]. In this context, other layered chalcogenides [259], and in particular TiS_2-based compounds, have attracted the interest of researchers for almost ten years now [137,140,161,165-166,260-262]. TiS_2 has a layered structure consisting of covalently bonded S-Ti-S sandwiches stacked along the *c*-direction (Figure 67a) and weakly stabilized by vdW interaction. Among the various known polymorphs of TiS_2, differing in the sequence of relative displacements of the S-Ti-S sandwiches, in this chapter it is taken into consideration the one crystallizing in trigonal space group *P-3m1* depicted in Figure 67, that is experimentally observed in commercially available TiS_2.

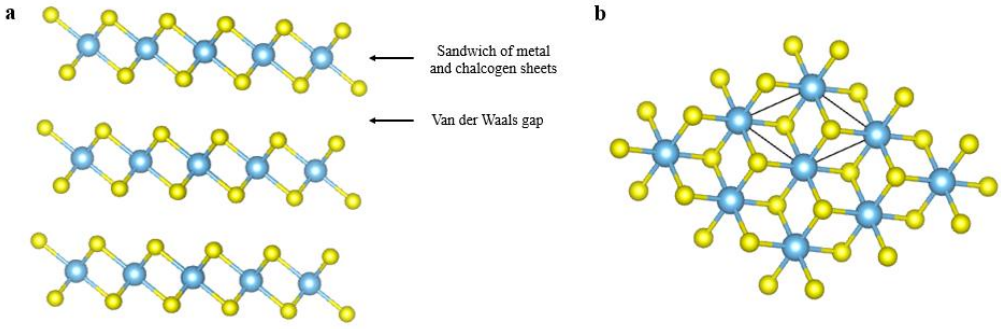

Figure 67. Crystal structure of trigonal TiS_2 (blue: Ti, yellow: S) with a=3.407 Å and c= 5.6989 Å [264] *a) side view; b) top view.*

The experimental studies on pristine TiS_2 need to control the stoichiometry very carefully during the synthesis, since self-intercalated $Ti_{(1+x)}S_2$ structures can be easily formed, with an injection of n-carriers in the conduction band [264]. The layered structure of TiS_2 is also prone to host in the vdW gap between S-Ti-S sandwiches a wide range of guest species, including monoatomic cations, molecular ions, and organic molecules, thus enhancing phonon scattering processes and hampering κ[163], which is ultimately beneficial for TE use. On the other hand, the fabrication of this type of heterostructures is expected to also affect the electronic transport properties, due to chemical interaction with the matrix and variation of carrier concentration[164].

The literature relative to *ab initio* studies on pristine TiS_2 is mainly concerned with the analysis of the electronic and vibrational properties, also in comparison with the fourth group sulphides and with the Ti chalcogenides [265–267]. In particular, the debate about the nature of TiS_2, whether it is a semimetal or semiconductor, is still lively [268,269]. As regards TiS_2 intercalation, the literature is quite limited, and concerns mainly metal cation intercalated TiS_2 [270,271]. Computational analyses of TiS_2 intercalated with organic moieties are lacking and limited to one single investigation on molecular dynamics simulations of phonon transport [272]. This study is focussed on organic-intercalated TiS_2, with the aim of elucidating by *ab initio* DFT calculations the electronic structure and transport properties of two hybrid compounds: i. hexylamine-intercalated TiS_2 (TiS_2/HA), already experimentally proposed as a hybrid TE material [162,165-166,267] and ii. adamantylamine-intercalated

TiS_2 (TiS_2/ADA), yet to be synthesized (Figure 68).

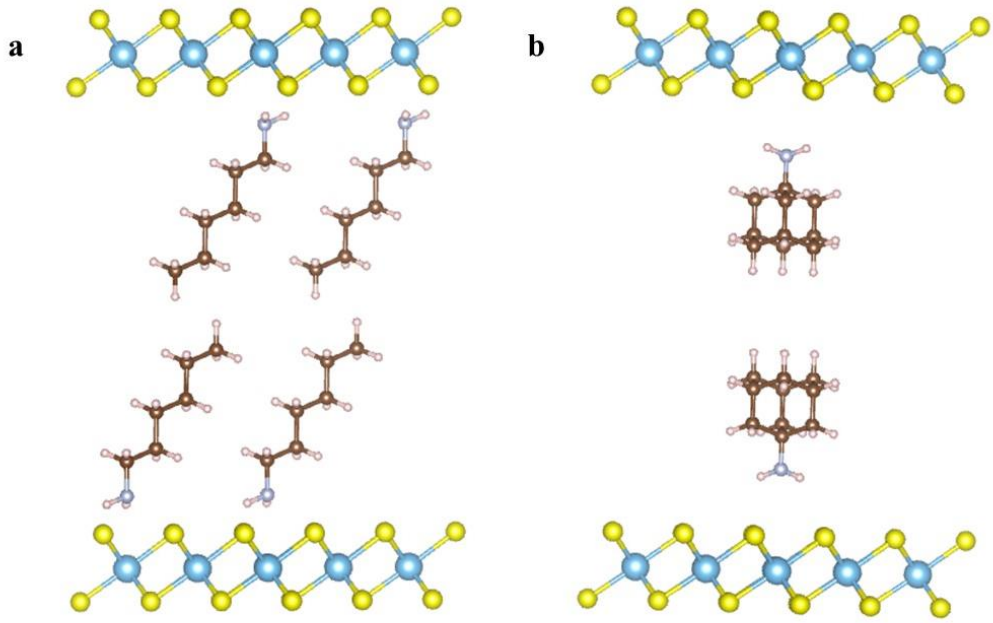

Figure 68. Model TiS_2-based hybrid compounds: a) TiS_2/HA and b) TiS_2/ADA.

ADA and HA are both aliphatic amines. The NH_2 group is linked to a secondary carbon in the case of HA, and to a tertiary carbon in ADA, which makes the latter slightly more basic. The substantial difference between the two molecules lies in their structural and geometric features. Previous studies have shown different possible arrangements of linear alkylamines when they are intercalated in layer structures [273,274]. For example, the paper by Wan et al.[166] describes two different configurations. The first with two organic molecules incorporated into the vdW gap of TiS_2, and the second with the organic molecule lying parallel to the basal plane of the TiS_2 layer. Such variance in the orientation of the organic molecule may lead to poor homogeneity and stability of the resulting material. On the contrary, ADA, thanks to its compact structure and shape, has significantly lower orientational variability and could be an ideal block to be incorporated into layered host materials, giving rise to stable hybrid multifunctional nanostructures.

In the following, the study carried out on a single geometric configuration of TiS_2/HA is reported and compared with the hypothesized structure of TiS_2/ADA,

to verify how the structural features of the intercalant (size and geometry) affect the electronic and transport properties.
The simulations related to the thermoelectric properties part were performed at the Theoretical Chemistry Department of Technische Universität Dresden.

5.2 Methods

The DFT + U calculations were carried out by using the ab initio simulation package VASP [275] for the computational analysis of TiS_2 electronic properties. All calculations were performed using the generalized gradient approximation [245] and the PBEsol exchange-correlation. The degauss parameter, the positions of atoms, and the Hubbard parameter [245] were optimized to increase simulation efficiency and improve subsequent calculations. The value of Hubbard U correction for the Ti atom was set to 3 eV. The plane-wave cut-off energy was set to 500 eV, and a denser Monkhorst-Pack (MP) [276] k-point meshes 9x9x1 was adopted. Based on the band structure calculation, the TE transport coefficients (i.e., S, σ, and κ_e) were calculated with the BoltzTraP code [277], assuming an isotropic electron relaxation time of 2.6×10^{-14} s [278,279]. The algorithm by Tang et al. [255] was used for Bader charge density decomposition.

5.3 Results and discussion

5.3.1 Bulk TiS_2

The bulk TiS_2 lattice constants were optimized and resulted in good agreement with experimental data, as shown in Table 21 [263]. The band structure and the DOS are plotted in the energy range −6.0 to 6.0 eV along the paths joining the high-symmetry k-points drawn in Figure 69. The presence of an indirect bandgap of 0.1 eV can be observed between the valence band (VB) maximum at Γ (indicated with G in Figure 70), and the conduction band (CB) minimum at L. This bandgap value agrees with the predicted semiconductor nature of TiS_2 [265-266,268-269]. In the DOS, the peak at

−4.7 eV is ascribed to the S 3p state and the sharp peak at −2.9 eV results from the localized Ti 3d-S 3p hybridization. The peaks in the range 0.8-3.0 eV above the Fermi energy are mainly of Ti 3d character. Then, the 3p orbitals of sulphur are predominant in the VB, while in the CB the 3d orbitals of titanium prevail.

Table 21. Difference between the cell parameters obtained and the literature's parameters.

	Lattice parameter (Å)	Error (%)
a	3.3973	-0.3
c	5.6056	-1.6

Γ	0.00000 0.00000 0.00000
M	0.00000 0.50000 0.00000
K	-0.33333 0.66667 0.00000
Γ	0.00000 0.00000 0.00000
A	0.00000 0.00000 -0.50000
L	0.00000 0.50000 -0.50000
H	-0.33333 0.66667 -0.50000
A	0.00000 0.00000 -0.50000

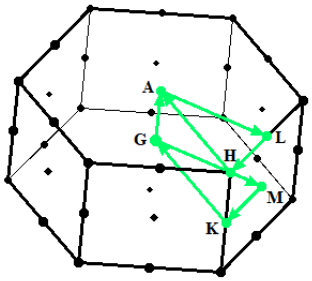

Figure 69. First Brillouin zone of the P-3m1 space group with high-symmetry points.

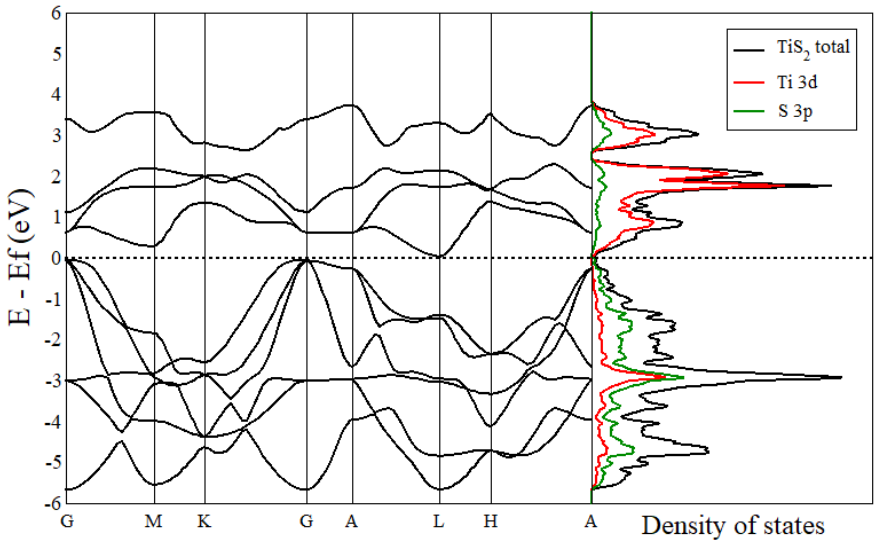

Figure 70. Electronic band structure and (right panel) pDOS of bulk TiS_2.

With regards to the transport properties, the S, the σ of TiS_2 as n-type semiconductor [266] and the PF were calculated with BoltzTrap as function of carrier concentration

at 300 K (Figure 3). As can be easily expected, the σ increases steadily with carrier concentration, while the *S* has the highest value of |*S*| at a carrier concentration of 10^{20} cm^{-3}. A fair compromise between *S* and σ can be set around 10^{21} cm^{-3} and this trade-off is confirmed in Figure 71, showing that *PF* has a maximum between 10^{20} and 10^{21} cm^{-3}. At a carrier concentration of 10^{20} cm^{-3} and at a temperature of 300 K, we obtain $S = -158.7$ μV/K, $\sigma = 4.2\times10^4$ S/m, κ_e = 0.38 W/mK and *PF* = 1.06 mW/mK^2.

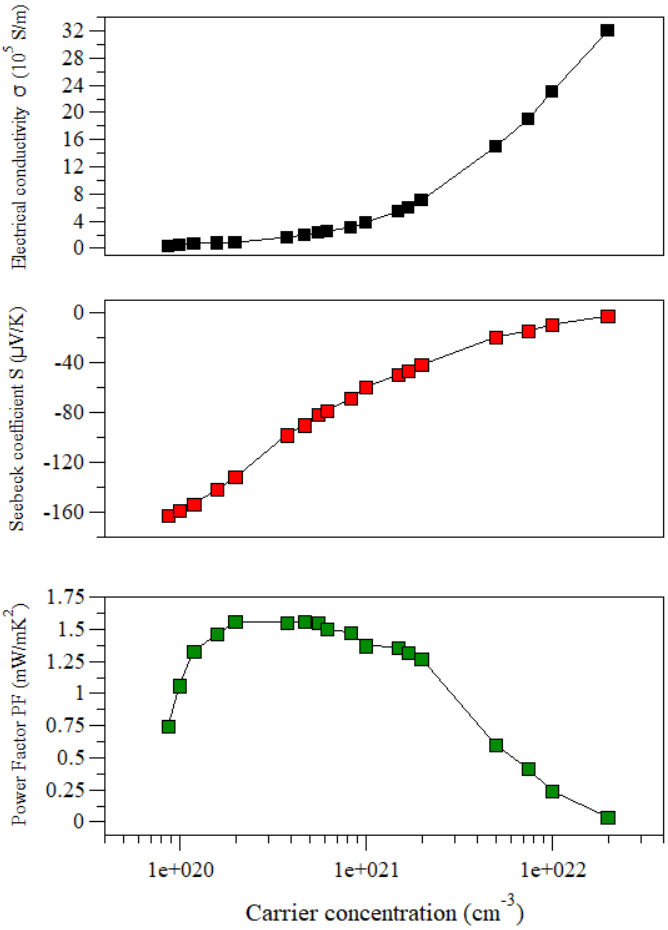

Figure 71. Calculated thermoelectric parameters of bulk TiS_2 vs. carrier concentration (logarithmic scale): a) electrical conductivity; b) n-type Seebeck coefficient; c) power factor.

Figure 72a reports the calculated κ_e as a function of carrier concentration, while in Figure 4b the corresponding *ZT* values are drawn. Considering a κ_L of about 4.3 W/mK [271], the resulting estimated *ZT* = 0.2 is in line with experimental

determinations. Guilmeau et al. [280] predicted smaller values for *S* and conductivities, resulting however, by compensation, in a very similar *ZT*. Although the comparison with experimental data should be taken very cautiously, as the stoichiometry of TiS_2 is hard to control precisely during the syntheses, and self-intercalated Ti can influence the measured TE parameters [133], these figures can be considered in fair agreement with literature values [271]

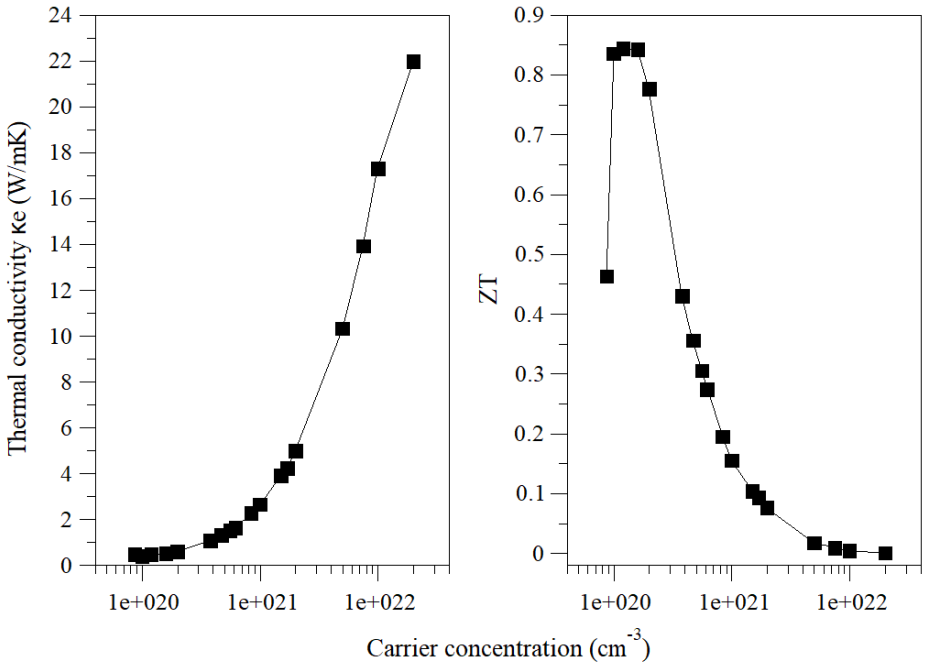

Figure 72. a) Calculated electron thermal conductivity κ_e vs carrier concentration (logarithmic scale) in bulk TiS_2; b) figure of merit ZT.

The TE parameters were also calculated along the *ab*-plane and *cross*-plane directions. The ratio between the two directions shows moderate anisotropy, $S_{(xx)}/S_{(zz)} = 1.56$ ($S_{(xx)} = -194$ μV/K), $\sigma_{(xx)}/\sigma_{(zz)} = 1.08$ and $\kappa_{(xx)}/\kappa_{(zz)} = 1.16$ at 300 K, related to the anisotropy of the chemical bonding in the structure. However, as pointed out by Glebko et al. [266], this connection should be interpreted cautiously in case of moderate anisotropy. The above quoted $S_{(xx)}$ value is in fair agreement with Glebko's. As for experimental determinations, the literature presents a wide spread of values [137,259], for which the above comment about the control of Ti stoichiometry in the synthesis routes of TiS_2 could also be effective.

In conclusion, the level of theory adopted for the simulation of the bulk TiS_2 band structure appears to be in reliable agreement with the recent literature and therefore was extended to the computations relative to the hybrid TiS_2-intercalated compounds.

5.3.2 Cell expansion and intercalation with hexylamine and adamantylamine

Intercalation of organic and inorganic species in the TiS_2 vdW gap, as discussed mainly in the literature, can strongly modify the TE properties of layered materials. This effect depends on the kind of intercalating species. For example, it is well-acknowledged that metal cation intercalation injects electrons into the conduction band. However, no matter the intercalant, an increase in structural defects and enhanced scattering processes are understood to be beneficial for reducing κ. Organic molecules inserted in the vdW gap of TiS_2 could, ideally, limit the κ_L component and leave the electronic conductivity unchanged parallel to the ab plane. As a preliminary approach to the computational analysis of TiS_2 hybrids, the study of the electronic structure of TiS_2 at increasing distance between the layers was carried out. In the simulations, lattice constant *a* was fixed to the optimized 3.3973 Å value determined for bulk TiS_2, and the lattice constant *c* was increased with a step Δ=2 Å (c = 5.6056 Å. + nΔ). The bandgap steadily increases from the bulk value of 0.1 eV to 0.23 eV for n=8, while the Γ and A BZ points collapse (Figure 73a) as each 2D layer is increasingly isolated. Simultaneously, the branches along the paths ΓMK and ALH, parallel to the *ab* plane, tend to become symmetric; this change in the band structure is already visible at a lattice parameter of 9.6 Å (Figure 73b), demonstrating that the interaction between S-Ti-S sandwiches is easily quenched already at a relatively small swelling level. These results are consistent with the band structure calculations for other nanosheet materials [281,282]. Due to quantum confinement [283,284], in the interval (−0.4 to 0.4) eV the monolayer-like DOS features of the swelled structure are much sharper than those of the bulk (Figure 74); simultaneously, swelling produces a drastic increase of anisotropy at 300 K, as shown in Figure 75.

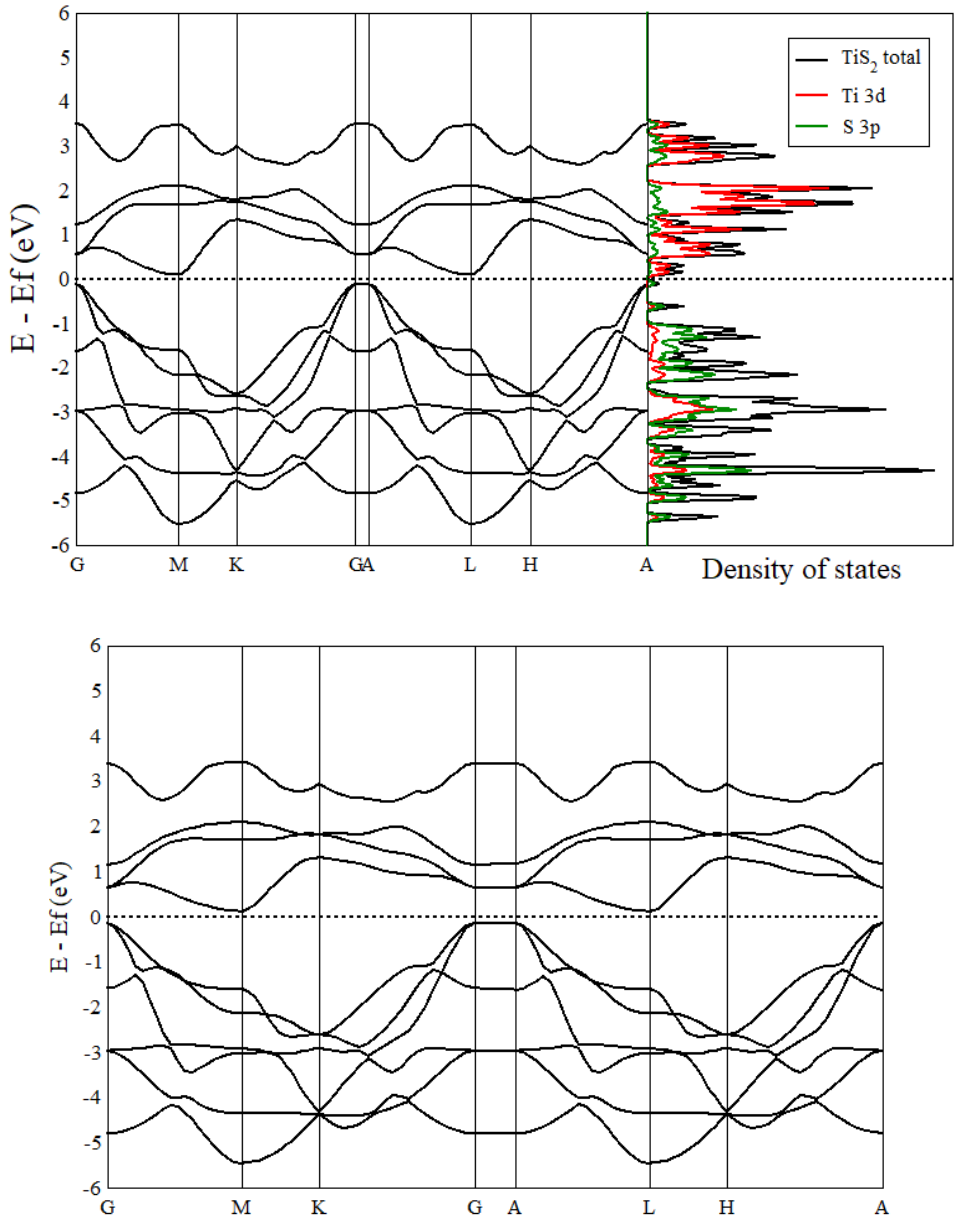

Figure 73. a) Electronic band structure along the paths depicted in Figure 69 and (right panel) DOS of swelled TiS_2 (c=21.6 Å); b) Energy bands at a spacing c=9.6 Å between the S-Ti-S sandwiches.

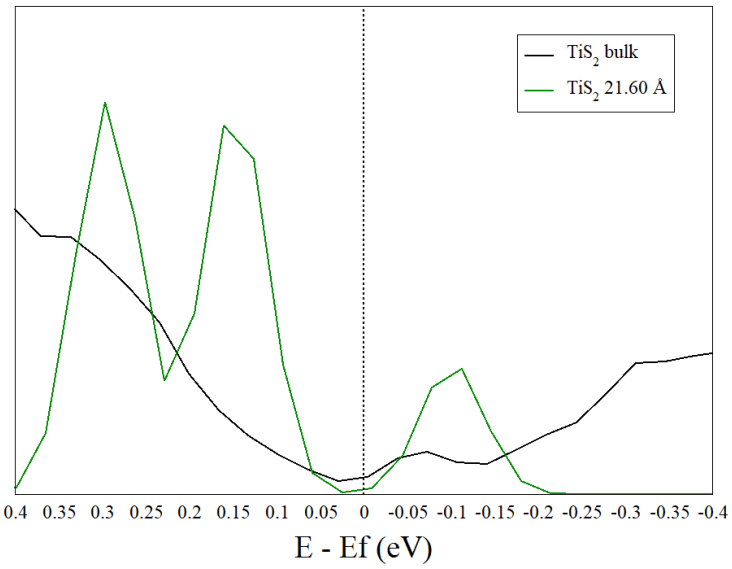

Figure 74. Bulk and swelled TiS_2 DOS close to the Fermi level.

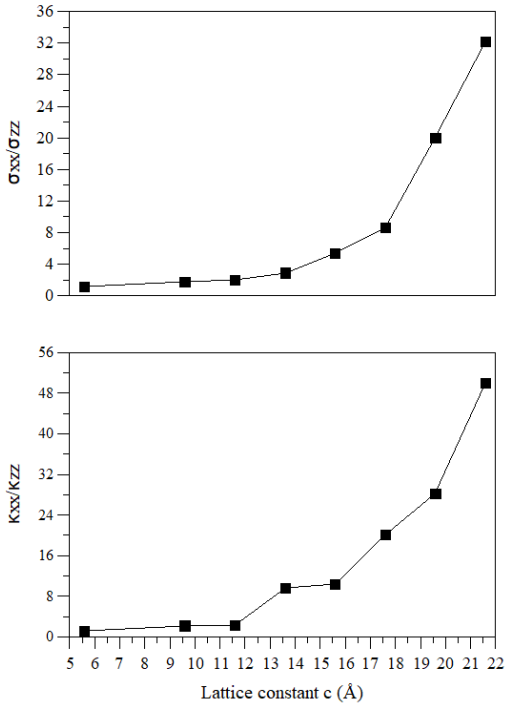

Figure 75. Relationship trends of $\sigma_{(xx)}/\sigma_{(zz)}$ and $\kappa_{(xx)}/\kappa_{(zz)}$ as a function of increasing lattice constant c (Å).

The artificially increased distance between the layers has its counterpart in the analysis of what happens when a similar widening of the interlayer gap is accomplished by the intercalation of an organic species. Aiming at evaluating organic candidates for TiS_2 intercalation, the band structure, and the TE parameters, as a function of carrier concentration at 300 K, were calculated for two intercalated compounds: TiS_2/HA taken as a reference, and TiS_2/ADA as a potential new TiS_2-based hybrid material.

An atomic structure for TiS_2/HA has been hypothesized in only one paper [162]. After intercalation, the spacing between TiS_2 layers increases, slightly less than twice the length of HA, indicating a bilayer sheet of slightly slanted intercalated hexylamine molecules.

This evidence was experimentally confirmed by acquiring XRD data from the final TiS_2/HA product, with the HA slope of 40.0° and a layer spacing of approximately 22 Å [285]. This structural scheme was adopted in the simulations, with the N-C bond perpendicular to the S-Ti-S layer, HA parallel to an axis and the angle with the (*a*,*b*) plane determined by the zig-zag sequence of carbon atoms.

The energy of the intercalated compound was calculated when gradually increasing the lattice constant *c* with a step Δ=1 Å ($c = 18.6056 + n\Delta$), finding a minimum value at c = 21.6 Å. A similar approach was adopted for TiS_2/ADA, with the minimum energy at c = 22.6 Å.

A 2x2x1 TiS_2 supercell (labeled Ti_4S_8 in the following) was then considered as a compromise between realistic stoichiometry and computing time. Both organic molecules are Lewis bases (electron donors), but the respective steric hindrance and the different chemical composition could play a role in the variation of the properties of the system.

Figure 76a shows the band structure of Ti_4S_8, as a reference for Ti_4S_8/HA and Ti_4S_8/ADA (Figure 76b-c). In these latter cases, it can be noticed that new bands arise, slightly below the Fermi level, due to the respective intercalants.

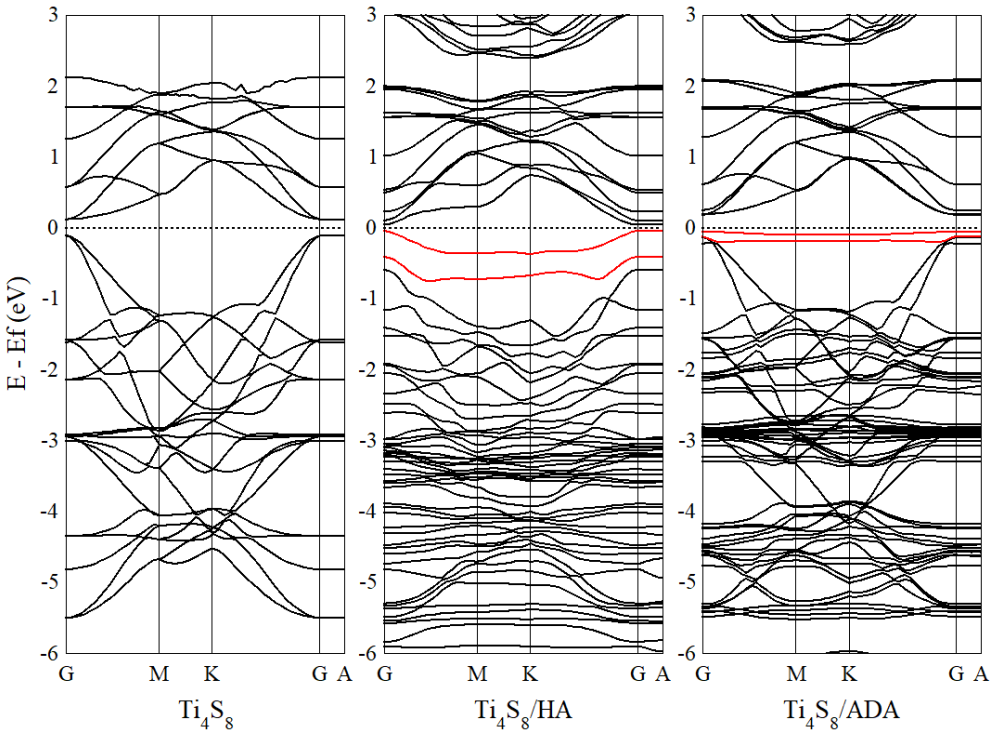

Figure 76. Electronic band structure of: a) the 2x2x1 supercell of TiS_2 (labelled as Ti_4S_8) with c=21.6Å. b) the TiS_2 supercell intercalated with hexylamine (Ti_4S_8/HA) and c) with adamantylamine (Ti_4S_8/ADA). Bands due to the intercalated organic molecule below the Fermi level are marked in red.

The pDOS of Ti_4S_8/HA and Ti_4S_8/ADA are plotted in Figure 77. In both intercalated compounds the states from −2.5 eV to −6 eV is formed by the hybridization of C 2p, N 2p, H 1s, S 3p, and Ti 3d. Around the Fermi energy a noticeable contribution of orbitals deriving from the organic molecules can be observed, in correspondence of the new branches in the band structures. In the case of Ti_4S_8/HA, the sharp peaks around −0.3 eV and −0.7 eV are due to the hybridization of N 2p, Ti 3d, and S 3p, while for Ti_4S_8/ADA the peak around −0.2 eV is attributed to the hybridization of N 2p and C 2p. From 0 eV to 4 eV above the Fermi level, all peaks are predominantly composed of Ti 3d state, like in bulk TiS_2. Then, the 2p orbitals of nitrogen and carbon and 1s orbital of hydrogen lead to substantial variation in the VB, while in the CB the 3d orbitals of titanium are still prevailing.

In Figure 78 the band structures of Ti_4S_8/HA and Ti_4S_8/ADA are compared with those of Ti_4S_8 and with the HA and ADA components alone, whose respective

pDOS within 1 eV of the Fermi level are also plotted in Figure 79a-b. It can be recognized that, as a result of the interaction with the inorganic scaffold, the energy bands of the intercalated molecules are modified, and in particular that the top VB energy levels are split, as also evidenced by the comparison between the zoomed DOS patterns reported in Figures 77b,d and those of the organic components (Figure 79a-b).

Moreover, by comparing the band structure of pristine TiS_2 and the free organic molecule, with the intercalated compound (Figure 78), new bands not belonging to the two separate components are visible between 2 and 3.5 eV, and they could be the product of the interaction between the two components.

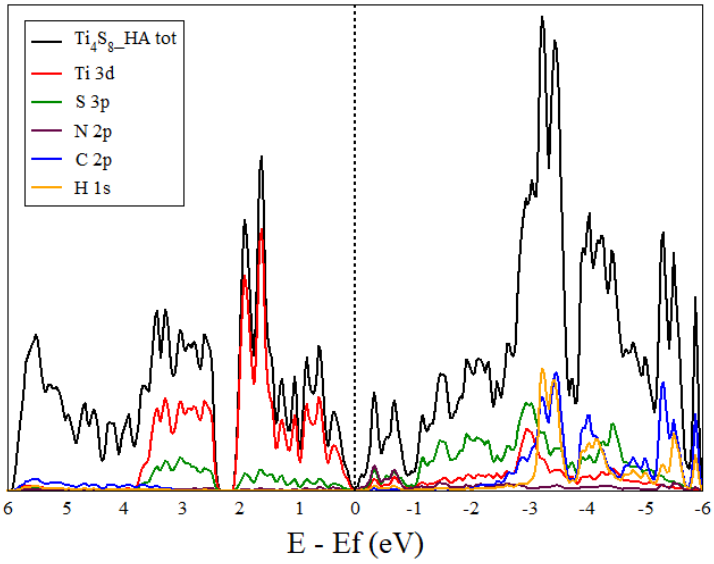

a)

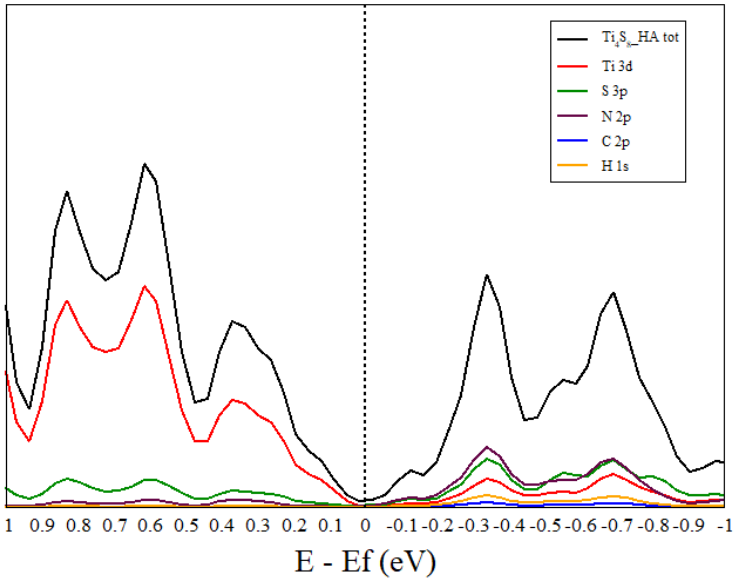
Ti4S8_HA tot
Ti 3d
S 3p
N 2p
C 2p
H 1s
1 0.9 0.8 0.7 0.6 0.5 0.4 0.3 0.2 0.1 0 -0.1 -0.2 -0.3 -0.4 -0.5 -0.6 -0.7 -0.8 -0.9 -1
E - Ef (eV)

b)

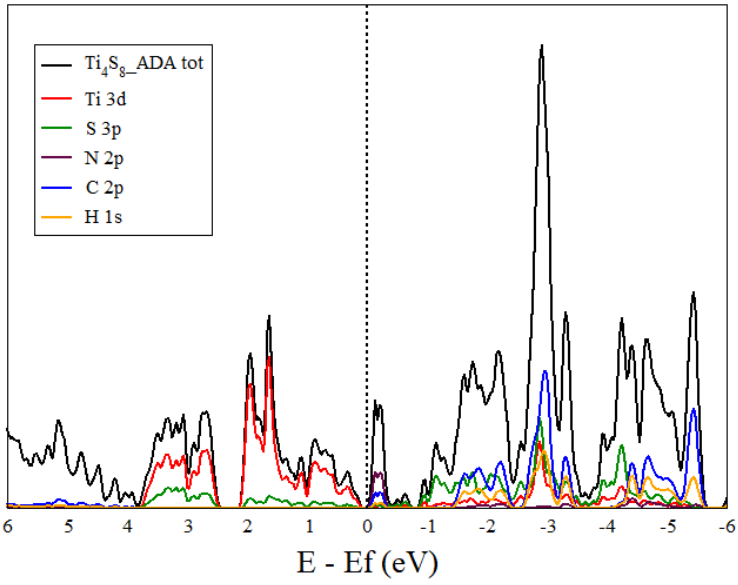
Ti4S8_ADA tot
Ti 3d
S 3p
N 2p
C 2p
H 1s
6 5 4 3 2 1 0 -1 -2 -3 -4 -5 -6
E - Ef (eV)

c)

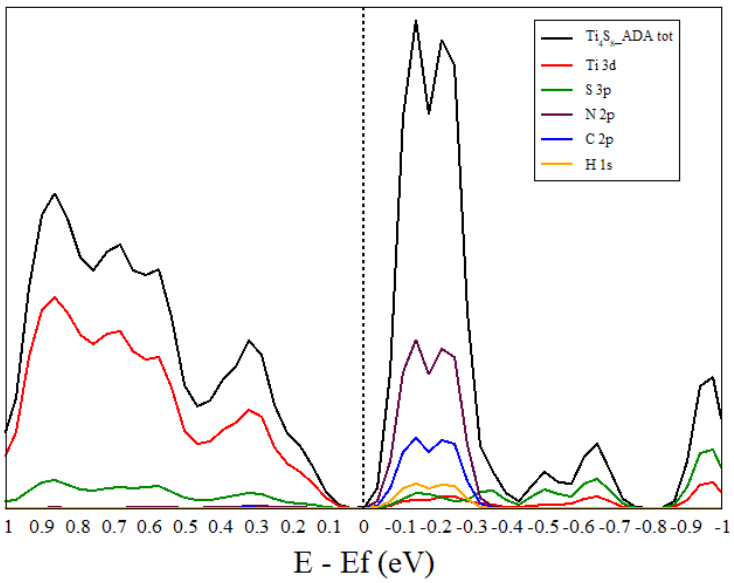

d)

Figure 77. a-c) DOS of Ti_4S_8/HA and Ti_4S_8/ADA; b-d) enlargement of the previous plots close to the Fermi level.

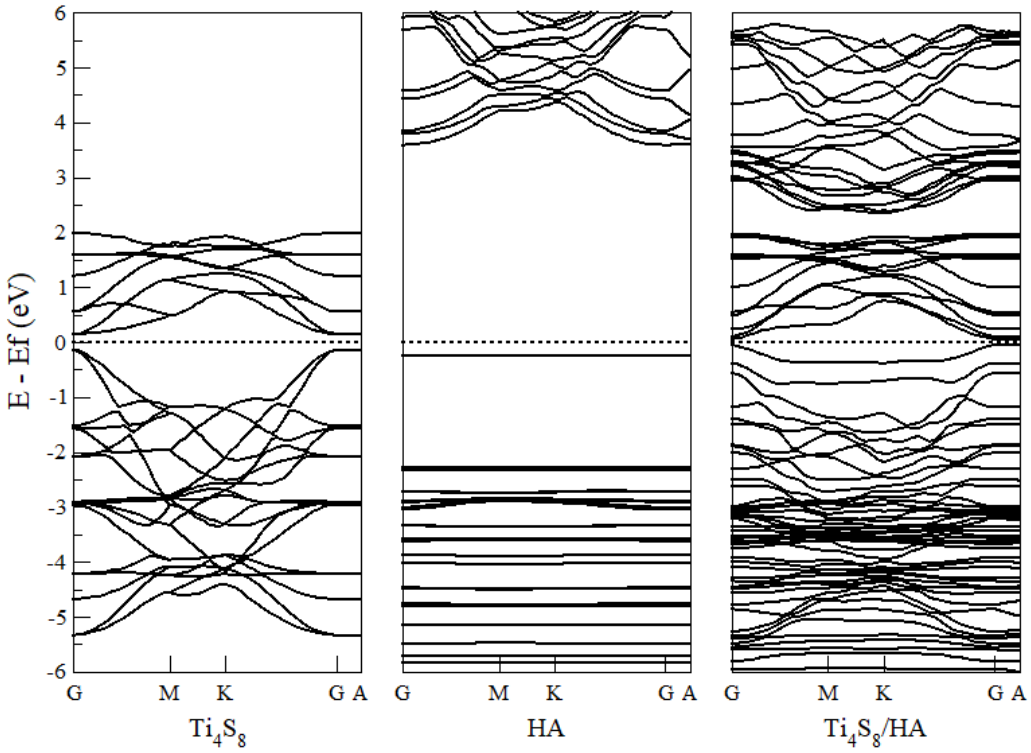

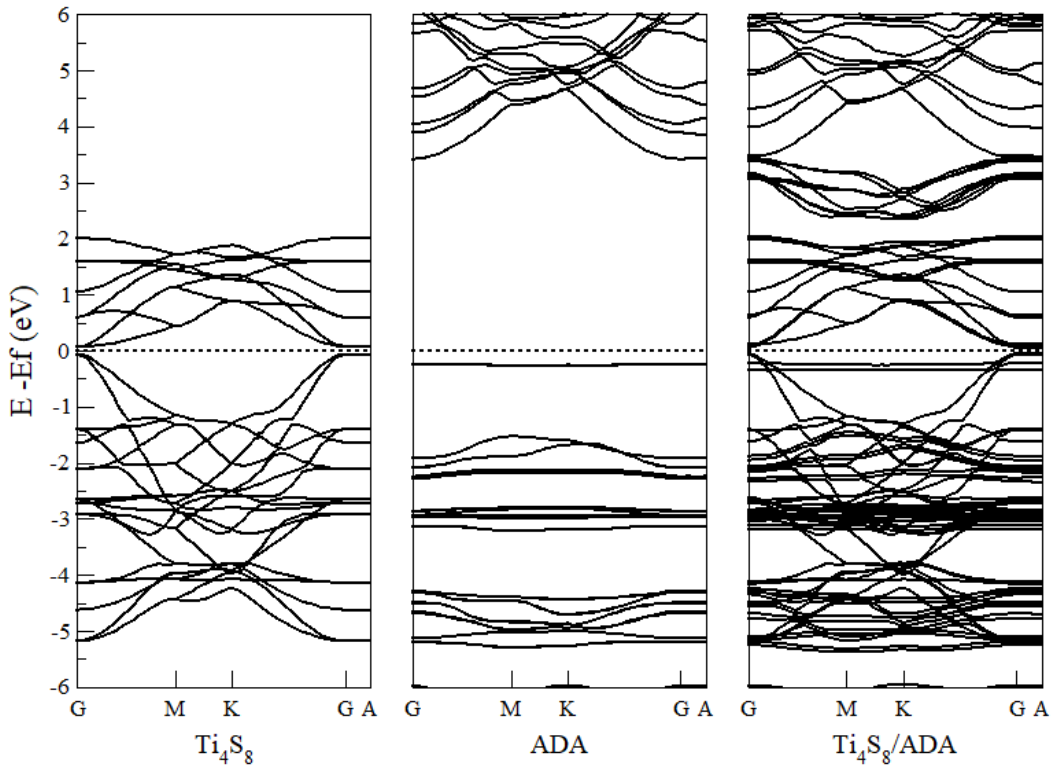

Figure 78. a) Electronic bands of, respectively, Ti_4S_8, HA molecules packed with the same structure as in the intercalated compound, Ti_4S_8/HA; b) electronic bands of Ti_4S_8, ADA molecules packed with the same structure as in the intercalated compound, Ti_4S_8/ADA.

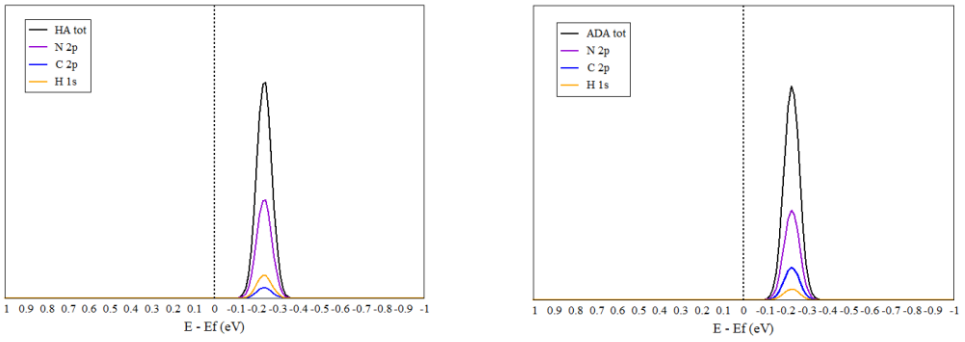

Figure 79. pDOS of a) HA, and b) ADA, close to the Fermi level.

To further assess the interaction between the organic moieties and the inorganic scaffold, Bader charges (reported in Table 22) were computed, as well as the formation energies of the components and of the intercalated compounds. The

energy balance for the intercalation reaction is equal to −2.1 eV for Ti_4S_8/ADA and to −0.9 eV for Ti_4S_8/HA (see Table 22). The energetically favoured intercalation reaction, experimentally observed for hexylamine, is then confirmed by the simulated reaction energies. The simulation also demonstrates the possibility of intercalation of adamantylamine, with an even larger formation energy per molecule.

Table 22. Bader charges and formation energies (eV) of Ti_4S_8, HA and ADA, and of the respective intercalation compounds.

	Ti_4S_8	**HA**	**Ti_4S_8/HA**	**ADA**	**Ti_4S_8/ADA**
Ti	10.23	-	10.21	-	10.23
S	6.89	-	6.91	-	6.90
C	-	4.00	3.99	3.98	3.98
H	-	0.92	0.92	0.94	0.94
N	-	6.11	6.14	6.14	6.14
Total inorganic	96.00	-	96.12	-	96.11
Total organic	-	88.0000	87.8748	124.0000	123.8846
Total	-	-	184.0000	-	220.0000
E (eV)	-9104.61	-3982.60	-13088.10	-6017.75	-15124.44

Figure 80 shows the comparison between the electronic charge difference maps of Ti_4S_8/HA and Ti_4S_8/ADA (respect organic molecules packed with the same structure as in the intercalated compound and respect the slab) along the sections (010) highlighted in the drawings.

A simple hypothesis for the intercalated complex formation is based on the charge transfer between the organic molecules and disulphide layers [238,164]. The analysis of the Bader charges and the analysis of the electronic charge difference maps, reported in Figure 78, show that there is a transfer of electronic charge from the organic molecule to the inorganic scaffold. In particular, the Bader charges demonstrate a simultaneous decrease in the charge of the organic molecule (−0.14% in the case of Ti_4S_8/HA) and an increase in the charge of the inorganic layer (+0.13%).

Looking at the Figure 80, in Ti_4S_8/HA a collective drift of the electron density is observed towards the S-Ti-S sandwich, resulting in a depletion of electrons in the opposite ends of facing molecules, for Ti_4S_8/ADA the charge rearrangement involves a different pattern of polarization, leading to a diffuse framework of electrostatic interactions between electron-enriched and electron-depleted regions. A donation of electronic charge takes place from the intercalators to the inorganic scaffold, as hypothesized in the literature [238,164], accompanied by the population of the Ti 3d orbital by the nitrogen lone pair and the drift of electronic charge from the hydrocarbon tails of HA and ADA towards the amine head. In fact, inspection of Figure 78 alows to recognize a different behaviour of the Ti close to the organic molecule compared to those more distant. Furthermore, in the case of Ti_4S_8/HA, a union between the electronic clouds of nitrogen and titanium can be noted. Even the sulphurs close to the organic molecules show a different electronic rearrangement compared to the more distant ones.

This difference between the charge distributions could be closely related to the different distance between N and slab, which is smaller in the case of the intercalated with HA than in the intercalated with ADA (Table 23), a consequence of a different interaction between the two organic molecules and their respective slabs, probably deriving from different steric effects.

a)

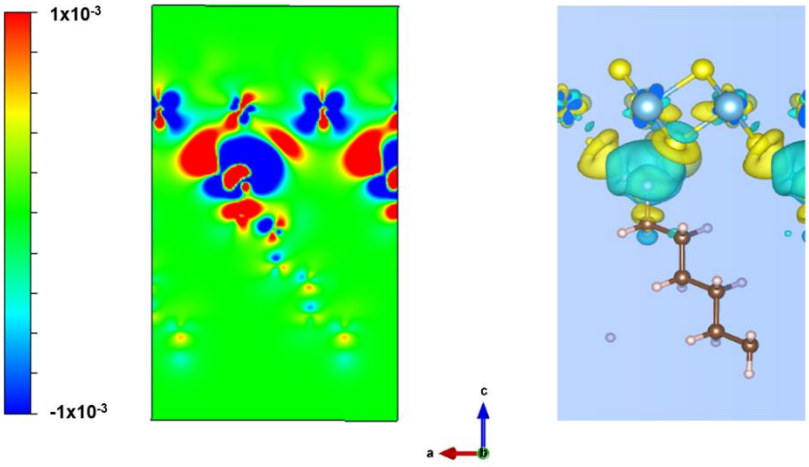

b)

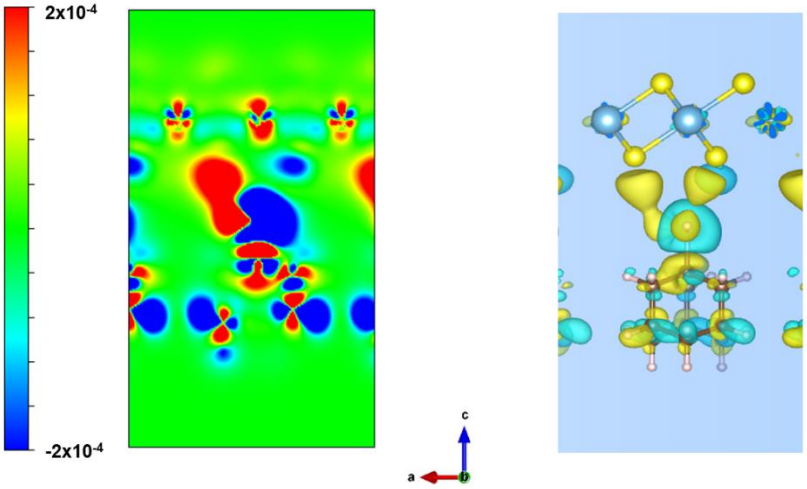

Figure 80. Electronic charge difference maps in the (010) sections of a) Ti_4S_8/HA and b) Ti_4S_8/ADA compared to molecules packed with the same structure as in the intercalated compound and the inorganic slab.

Table 23. Distance between N and slab.

	Ti-N (Å)	Ti-S (Å)
Ti_4S_8/HA	4.57	2.55
Ti_4S_8/ADA	5.65	3.66

Table 24 reports the relevant TE parameters of bulk TiS_2 and of the intercalated compounds at a carrier concentration of 10^{20} cm^{-3} and at a temperature of 300K.

Table 24. Thermoelectric parameters of Ti_4S_8, Ti_4S_8/HA and Ti_4S_8/ADA.

	Ti_4S_8	Ti_4S_8/HA	Ti_4S_8/ADA
$\boldsymbol{S}$ (μV/K)	-158.7	-135.8	-140.9
$\boldsymbol{\sigma}$ (S/m)	4.2×10^4	2.4×10^4	2.7×10^4
$\boldsymbol{\kappa_e}$ (W/m • K)	0.38	0.182	0.184
$\boldsymbol{PF}$ (mW/m • K^2)	1.152	0.443	0.536
$\boldsymbol{ZT}$	0.835	0.730	0.874

A decrease in σ and electronic contribution of κ results from intercalation, while the S at the carrier concentration of 10^{20} cm^{-3} does not vary significantly. The on-

plane and off-plane electrical and electron-thermal conductivities (Table 25) confirm that the organic intercalants strongly affect the transport properties of TiS_2 normal to the plane of the Ti-S slabs. In particular, both intercalants lower the σ and κ z-components compared to bulk TiS_2 as a result of the quantum confinement effect [286].

Table 25. xx and zz components of the electrical conductivity and electron-thermal conductivity of Ti_4S_8 and intercalated compounds.

	$\sigma_{(xx)}$ (S/m)	$\sigma_{(zz)}$(S/m)	$\kappa_{(xx)}$ (W/mK)	$\kappa_{(zz)}$ (W/mK)
Ti_4S_8	4.3×10^{4}	4×10^{4}	1.456	1.274
Ti_4S_8/HA	1.4×10^{4}	1.3×10^{2}	0.416	2.6×10^{-4}
Ti_4S_8/ADA	9.3×10^{3}	5.2×10^{1}	0.455	2.3×10^{-4}

Tables 26 and 27 report the S, the σ, and the PF as a function of the concentration of charge carriers for, respectively, TiS_2 intercalated with hexylamine and with adamantylamine; in Figure 81 the respective ZTs are plotted as a function of carrier concentration. A marginally better performance of ADA could be recognized, within the assumptions of the proposed computational models.

Table 26. Predicted n-type Seebeck coefficient, electrical conductivity, and electron thermal conductivity of Ti_4S_8/HA as a function of carrier concentration.

Carrier concentration (cm^{-3})	**S (μV/K)**	**σ (S/m)**	**κ_e (W/mK)**
1×10^{18}	−48.2	3.2×10^{3}	0.111
4×10^{18}	−100.8	3.2×10^{3}	0.103
1×10^{19}	−173.8	3.4×10^{3}	0.086
4.4×10^{19}	−183	1.1×10^{4}	0.098
1×10^{20}	−135.8	2.4×10^{4}	0.182
4.8×10^{20}	−72.2	9.8×10^{4}	0.726
1×10^{21}	−45.4	2×10^{5}	1.324

Table 27. Predicted n-type Seebeck coefficient, electrical conductivity, and electron thermal conductivity of Ti_4S_8/ADA as a function of carrier concentration.

Carrier concentration (cm^{-3})	S (μV/K)	σ (S/m)	κ_e (W/mK)
1×10^{18}	−143.6	2.5×10^{3}	0.090
4×10^{18}	−185	3.3×10^{3}	0.085
1×10^{19}	−218	4.5×10^{3}	0.084
4.4×10^{19}	−190.6	1×10^{4}	0.082
1×10^{20}	−140.9	2.7×10^{4}	0.184
4.8×10^{20}	−73.9	1.25×10^{5}	0.845
1×10^{21}	−22.2	2.6×10^{5}	1.748

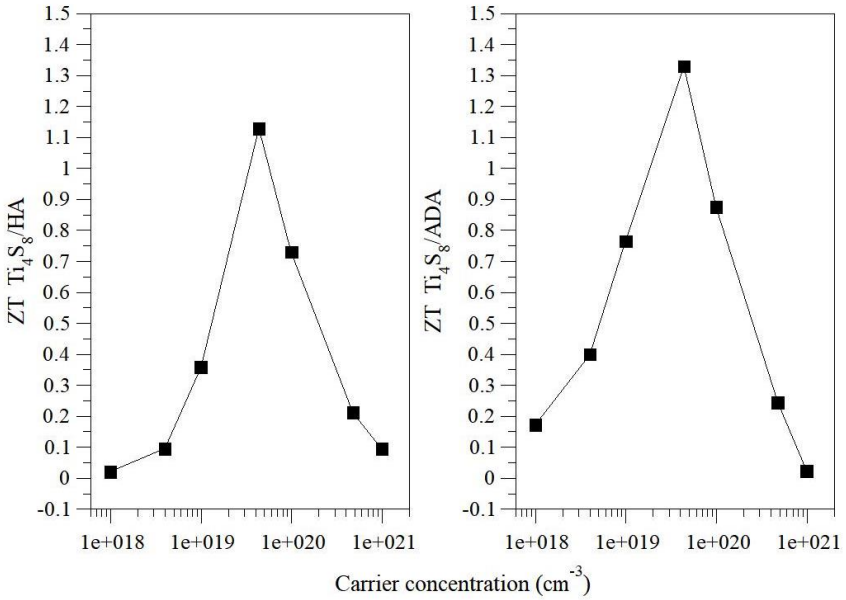

Figure 81. Calculated ZT as a function of carrier concentration of a) Ti_4S_8/HA and b) Ti_4S_8/ADA.

5.4 Conclusions

From the analysis of the electronic structure, it can be argued that the intercalation of differently shaped amines in the vdW gap of TiS_2 is effective in enhancing the 2D character and the anisotropic transport properties of hybrid intercalate with respect to pristine TiS_2. The comparison between HA and ADA shows a similar

behavior between the two amines, maybe somewhat better for ADA, in boosting the anisotropy of the properties of TiS_2. This latter conclusion holds within the framework of the Boltzmann transport theory and should be confirmed by actual measurements on real samples, but the simulations point to the possibility that the portfolio of organic intercalants of TiS_2 could be much richer than the mere HA described in literature. Considering that the anisotropic 2D properties of TiS_2 are already achieved at relatively small interlayer distances, interesting TE performance could be attained also with smaller molecules than HA and ADA. Among the large population of possible candidates, the isotropic shape of the intercalant could be suitable for achieving a spacing between the S-Ti-S sandwiches independent on the intercalant concentration, and therefore a better control on the TE properties.

The hypothesis put forth in literature [238,164], that TiS_2 intercalation is favoured by the Lewis base nature of the intercalant is substantiated in this thesis, demonstrating that electron donation of both ADA and HA molecules to the host inorganic scaffold is effective. Based on the Bader charge analysis and on the reported maps of charge density sections, it is proposed that the interaction mechanism involves the transfer of electronic charge from the intercalant Lewis base to TiS_2 and its accumulation of electronic charge on Ti, with the consequent establishment of an electrostatic host-guest interaction.

SUMMARY AND CONCLUSION

This PhD project was involved in the design, preparation, and characterization of materials for the development of new TE devices. Today, most of the research efforts in this field are addressed to the improvement of materials which already exhibit good TE parameters. The strategies to achieve this goal are described in the first chapter of this thesis and substantially deal with the task of overcoming, let's say, the *Wiedemann-Franz law's curse*; that is, the task of improving σ while keeping low thermal transport. My thesis work was inserted in this line of research; the reference compounds were the layered chalcogenides TiS_2 and MoS_2, which have interesting TE properties due to their 2D atomic structure, involving strongly anisotropic transport properties. The basic idea was that of improving, by intercalation of inorganic or organic moieties, the σ perpendicular to the S-Me-S sandwiches, while keeping low the κ thanks to the 2D nature of the matrix, eventually enhanced by the structural defectivity induced by intercalation.

So, PART II of this thesis was dedicated to the study of the insertion of metal ions in the vdW gap between the S-Me-S triple layers. The computational simulations involved the analysis of the electronic structure of TiS_2 intercalated with two transition metals, Cu and Ag, and two s-block metals, Li and Ca. It was demonstrated that all these metals modify the σ of the intercalated compounds, that is changed, to a different extent, to metallic character. The preparation of a real sample was limited to the lithium intercalation of MoS_2. For this compound a detailed structural analysis was carried out, demonstrating that lithium intercalation produces both stacking faults in the sequence of S-Mo-S triple layers, *and* intralayer disorder that was successfully modelled by assuming a correlated distribution in the mutual position of atoms within the S-Mo-S sandwiches. The possibility that the structural disorder involved also sequences of octahedral-coordinated whole layers was also addressed, and its feasibility discussed.

PART III of my dissertation is concerned with the idea of producing hybrid inorganic-organic compounds having (hopefully) the good characteristics of both the organic (flexibility, low κ, wide availability) and inorganic (high σ, chemical/mechanical stability) components. In particular, PART III was concerned

the simulation of the intercalation of two amines, hexylamine and adamantylamine, in the vdW gap of TiS_2. The insertion of hexylamine in TiS_2 is described in the literature and the resulting compound is claimed to show very interesting TE properties; on the other hand, its electronic structure was only partially investigated. As a counterpart of this well-acquainted compound, the intercalation of ADA, having a more compact shape but a similar height as HA, was also studied. Notably, the hybrid ADA-TiS_2 was not yet synthesized and then the reported simulations constitute a hint for the synthesis of a new TE material. The simulated TE parameters of the two inorganic-organic materials were substantially similar, allowing to foresee those various organic moieties, maybe also showing electronic conductivity, could be tested for intercalation in layered chalcogenides. A fundamental aspect for the technological implementation of inorganic-organic materials, that is the long-term range stability, was also investigated. Different degradation mechanisms were tested by *ab initio* periodic DFT calculations on a TiS_2/NH_3 model system, suggesting that TiS_2 reacts with molecular oxygen, resulting in Ti-N adducts, where N resides in lieu of S vacancies, with the subsequent formation of elemental sulphur and water. A comparison of the aging of TiS_2/HA in the presence or the absence of oxygen further corroborated the proposed mechanism since prolonged storage in inert atmosphere did not result in the degradation of the intercalated material, while sulphur evolution was detected with different techniques for the sample stored in air.

In conclusion, this thesis focused some crucial points for the development of a new generation of TE materials, but much work is still necessary for further developments. As concerns my research activity, I just mention the experimental counterpart, involving syntheses and functional characterization, of the metal-intercalated chalcogenides, the investigations about the stability of hybrid compounds, and the widely open field of intercalation of organic moieties into 2D layered chalcogenides.

APPENDICES

A. Characterization techniques

A.1. X-ray diffraction (XRD)

X-ray diffraction (XRD) is a non-destructive technique for the characterization of crystalline materials. For a crystalline sample, XRD analysis provides a complete three-dimensional picture of information about composition, structure, phases, interatomic distances, and other structural parameters such as size and crystallinity. The constructive interference of a monochromatic beam of X-rays scattered at specific angles from each set of lattice planes in a sample produces x-ray diffraction peaks. The intensities of these peaks are determined by the distribution of the atoms into the lattice. Consequently, the X-ray diffraction pattern is the fingerprint of a material. The measured angles can be converted back to get information about the underlying lattice periodicity based on Equation (S1):

$$d = \frac{\lambda}{2sen(\vartheta)} \quad \text{(S1)}$$

where λ(Å) is the X-ray wavelength, d(Å) is the spacing between lattice planes, and 2θ is the angle of diffraction [287].

A.2. Scanning Electron Microscopy (SEM)

Scanning Electron Microscopy (SEM) is a technique for image generation that, thanks to its operational simplicity, short imaging time, and nanoscale spatial resolution, is now prevalent in many fields of industry and research [288].

The technique makes use of the interactions between electrons and the atoms of the analysed sample. An electrical voltage accelerates the electrons emitted by the source and magnetic lenses are used to focus the beam. Depending on the texture

and composition of the sample, electrons interact differently with it. They can be reflected on the surface or can ionize atoms producing secondary electrons; both secondary and backscattered electrons can be detected to reconstruct the final image of the sample. SEM images represent the morphology of a sample and can also yield, thanks to the large depth of field of the technique, quasi-three-dimensional views of the sample surface; then, SEM is used to obtain a high-resolution picture of surface features. Moreover, the spectroscopic analysis of X-rays produced by the interaction between the incoming electron beam and the sample (carried out by an Energy Dispersive X-Ray Analyzer (EDX or EDA)) allows to obtain information about the distribution of different chemical elements within the sample [289].

A.3. Micro-Raman Spectroscopy

Raman spectroscopy is a spectroscopic non-destructive technique for probing the structure and properties of a wide variety of organic and inorganic materials. This spectroscopy is based on the inelastic scattering of a monochromatic beam that provides a structural fingerprint related to vibrational modes of molecules, rotational and other low-frequency modes of systems [289-291].

Micro-Raman spectroscopy (μRS) involves acquiring spatially resolved Raman spectra by combining the conventional Raman spectrometer with a microscopic tool, typically an optical microscope [292]. Spectral information obtained using conventional Raman spectroscopy is spatially averaged over a large area (~ $1mm^2$) whereas micro-Raman enables the collection of spectral information with submicron lateral and vertical resolution.

With the introduction of commercial micro-Raman instrumentation, this technique has emerged as a powerful and handy analytical tool for the characterization of a wide number of nanostructures over the last decades.

B. Computational approach

To design and discover novel TE materials with high TE performance, computational simulations have nowadays a significant role in projecting syntheses and understanding results. It is possible to predict some useful properties of solids through the simulation of electronic structure by *ab initio* quantum mechanics, using a molecular mechanics approach, or a combination of both (semiempirical methods). The choice of the method depends on the system being analysed and the computational resources available. In particular, *ab initio* methods start from fundamental physical principles to calculate the electronic structure of solids and the properties associated with them. For the study of systems with many electrons, density functional theory (DFT) is often used, which can satisfactorily describe the structure and energy of the orbitals in the case of TMDCs [293,294].

B.1. Density functional theory (DFT)

Nowadays, DFT is a powerful tool for computations of the quantum state of atoms, molecules, and solids and of ab-initio molecular dynamics.

In 1927, after the foundation of quantum mechanics, Thomas and Fermi conceived the first approximate version of the density functional theory [268,296]. Later, using the foundations of quantum mechanics, Hohenberg, Kohn, and Sham developed the quantum ground-state density functional theory, which opened a wide door to applications for realistic physical systems [297,298]. Since then, density functional theory has grown enormously and has become one of the main tools of theoretical physics and molecular chemistry.

In a microscopic system, electron-nuclei, electron-electron, nuclei-nuclei, and electron correlations interaction are described *via* the Schrödinger equation. The Born-Oppenheimer approximation [299,300] assumes that the nuclei of the atoms, molecules, or solids remain fixed and generate a static external potential in which the electrons move. The wave function of a system consisting of N electrons depends, in the Born-Oppenheimer approximation, on 3N spatial coordinates and N spin coordinates. By integrating the square modulus of the wave function on the

N spin coordinates and 3N-3 spatial coordinates, the electron density function is obtained, which therefore depends on a triad of spatial coordinates, as shown in Equation (S2).

$$\rho(r) = N \int dr_2 \dots dr_N d\alpha_1 \dots d\alpha_N \, \Psi^*(r, r_2 \dots r_N;\ \alpha_1 \dots \alpha_N)\, \Psi(r, r_2 \dots r_N;\ \alpha_1 \dots \alpha_N) \quad \text{(S2)}$$

The basic idea of the DFT theory is to refer to the electron density, which is a physically observable quantity, rather than to the polyelectronic wave function, which is an object difficult to manage from a computational point of view. The turning point in this direction was induced by the publication of Hohenberg and Kohn's paper, in which the two theorems were proved [297]:

Theorem 1: Given the electron density function $\rho(r)$ relative to the fundamental level of a gas of interacting electrons in an external potential $v(r)$, a uniqueness relation holds, up to an additive constant, between $\rho(r)$ and the potential $v(r)$.
Therefore, since the Hamiltonian is determined by $v(r)$, there exists a functional $E_V[\rho]=E_0$ which uniquely associates the energy value at the fundamental level with the electron density.
Theorem 2: A universal functional $E_V[\rho]$ exists, valid for any number of particles and for any external potential, whose minimization gives the correct ground state energy value in correspondence with the correct electron density function of the fundamental level.

In the article cited above, Hohenberg and Kohn define the energy functional using Equation (S3):

$$E_V[\rho] = \int v(r)\rho(r)dr + F[\rho] \quad \text{(S3)}$$

The functional $F[\rho]$ can be defined as the sum of a Coulomb term $J[\rho]$, as shown in Equation (S4), and of another universal functional $G[\rho]$ which includes the contributions of exchange, correlation, and kinetic energy.

$$J[\rho] = \iint \frac{\rho(r_1)\rho(r_2)}{r_{12}} dr_1 dr_2 \quad \text{(S4)}$$

The fundamental work of Hohenberg and Kohn was followed by the study of Kohn and Sham [298], who defined the functional *G[ρ]*, as shown in the Equation (S5), and outlined the procedure for electron density calculation.

$$G[\rho] = T_S[\rho] + E_{xc}[\rho] \quad \text{(S5)}$$

$T_S[\rho]$ represents the kinetic energy term of non-interacting electrons' gas, while $E_{xc}[\rho]$ contains the terms of correlation and exchange of an interacting system of electrons.

If *ρ(r)* is a function that varies slowly enough to be considered locally uniform, the functional is defined by Equation (S6).

$$E_{xc}[\rho] = \int \rho(r)\varepsilon_{xc}[\rho(r)]dr \quad \text{(S6)}$$

where $\varepsilon_{xc}[\rho(r)]$ is the exchange and correlation energy *per electron* of an electron gas of uniform density *ρ(r)*.

B.1.1. Exchange-correlation functionals

The central problem of the DFT method is the definition of functionals which adequately describe the exchange-correlation term, $E_{xc}[\rho]$.

As reported in the previous section, Kohn and Sham proposed for this contribution the functional defined in Equation (S6), based on the assumption that locally the function could be assumed as the electron density of a uniform electron charge distribution. Starting from the previous equation, this functional can then be defined using Equation (S7).

$$E_{xc}^{LDA}[\rho] = \int \rho(r)\varepsilon_{xc}[\rho(r)]dr \quad \text{(S7)}$$

Where *LDA* is *Local Density Approximation* [301].Since this approximation has often proved inadequate for the study of molecular systems, the *Generalized Gradient Approximation* (*GGA*) was introduced [244].

In the *GGA* functionals type, in addition to the electron density dependence, also the dependency on its gradient is introduced.

One of the problems of *LDA* and *GGA* is that these functionals tend to overestimate the magnitude of the exchange energy (E_x) of electrons with parallel spins and with a significant overlap of orbitals in the same region of space.

A possible way to overcome this issue could be the use of hybrid functionals. In this case, the trade term is the weighted sum of a Hartree-Fock trade contribution and a trade-correlation DFT term, as shown by Equation (S8).

$$E_{xc} = f E_x^{HF} + (1 - f) E_{xc}^{DFT} \quad \text{(S8)}$$

where *f* is an empirically established coefficient. A functional that provides precise results, similar to more empirical functionals, is the *PBE* functional (Perdew-Burke-Ernzerhof), which is based on the GGA approximation [302]. A modification is the *PBEsol* functional, designed to improve some solid properties such as bond lengths and lattice parameters [245,303].

B.1.2. Hubbard's correction

The approximate exchange-correlation functionals used in modern DFT fail for systems having atoms whose ground state has a partially occupied electronic structure and strongly localized orbitals (*d* or *f* type). In these cases, it may be sufficient to perform a DFT+U calculation. Hubbard's "U" correction accommodates the strong Coulomb interaction of localized electrons and consists of an additive E_U term added to the local and semi-local density functionals, as shown in Equation (S9), derived from the Hubbard Hamiltonian [246].

$$E_{DFT+U} = E_{DFT} + E_U \quad \text{(S9)}$$

B.2. Quantum ESPRESSO

Structural optimizations and energy calculations for this work of thesis were performed using the Quantum ESPRESSO (QE) open-source code suite, developed by *P. Giannozzi et al* in 2001 [241,304], which implements various methods and algorithms aimed at realistic modelling of materials based on density functional theory (DFT). The method is based on density functional theory, density functional perturbation theory, and many-body perturbation theory, in the realm of the plane-wave pseudo-potential and projector-augmented-wave approaches.

Quantum espresso owes its popularity, beside the fact that it is distributed for free, to the wide variety of properties of the matter that can simulate, and to its performance. With QE it is possible to perform different tasks, including ground-state calculations, structural optimization, electrochemistry and special boundary conditions, spectroscopic properties, and quantum transport. Quantum Espresso can be used for any crystalline or supercell structure, both for metals and for insulators. Atomic nuclei can be treated by pseudopotentials of different types: conserving Pseudopotential (NCPP), ultrasoft (USPP), or projector augmented wave (PAW). Also available are several exchange-correlation functionals relating to the local density approximation (LDA) or the generalized gradient approximation (GGA) or advanced functionals introducing Hubbard corrections (U), some meta-GGAs, and hybrid functionals. QE is organized into several code packages including PWscf (Plane-Wave Self-Consistent Field), that consist in a set of programs for electronic structure calculations. The PWscf routines include *projwfc.x* for calculating the density of the occupied states, *bands.x* for calculating the electronic band structure, and *pw.x* which allows to make various calculations. Moreover, it is possible to perform an optimization relative to the atomic positions and lattice cell parameters through the vc-relax calculation, through the Broyden-Fletcher-Goldfarb-Shanno (BFGS) algorithm, or in damped dynamics [305]. Such codes are built around periodic boundary conditions, which allow a simple treatment of infinite crystalline systems.

Another package present in Quantum Espresso is PHonon, which implements the density functional perturbation theory (DFPT) for the calculation of phonons in crystals, based on the information calculated by PWscf.

B.3. VASP

Within this thesis, the VASP package was also used to realize some of our DFT calculations. The Vienna Ab initio Simulation Package (VASP) is a computer program for atomic scale materials modelling from first principles [306-308]. Periodic systems can be built with VASP from unit cells repeated in 3D space. VASP is a package for performing ab initio quantum mechanical calculations using either Vanderbilt pseudopotentials, or the projector augmented wave method and a plane wave basis set. The basic methodology is density functional theory (DFT), but the code also allows the use of post-DFT corrections such as hybrid functionals mixing DFT and Hartree-Fock exchange, many-body perturbation theory, and dynamical electronic correlations.

VASP has four principal input files (POSCAR, POTCAR, INCAR, KPOINT) and three main output files (CONTCAR, OUTCAR, OSZICAR). POSCAR contains the starting lattice geometry and ionic positions. POTCAR is a list of pseudopotentials for each atom in the system. INCAR is the central input file, which includes the majority of keywords for the calculations, like the cut-off energy, the smearing parameters, the convergence parameters, etc. KPOINT file indicates the coordinates and weights of k-points in the Brillouin zone for sampling. In our case, an automatic k-mesh was used. The CONTCAR file is written and renewed after each ionic step. It contains lattice geometry and ionic positions after optimization. It has a similar format as the POSCAR file and is normally written in direct coordinates. The OUTCAR file is the main output file of VASP and includes most output data of the calculation. The OSZICAR file is a simplified version of the OUTCAR file which sums up the information in one line for each electronic step. In this file, iteration count, total energy, and change of total energy can be easily found.

B.4. BoltzTrap

To study thermoelectricity, it is crucial to be able to calculate the transport properties of a system. The BoltzTrap code allows one to compute these transport coefficients with little computational effort [277]. This code uses Fourier expansions to solve the Boltzmann equation in the relaxation time approximation. Band structure interpolation is used to compute the derivatives required to evaluate the transport properties. In BoltzTraP, the relaxation time can be considered independent of temperature and energy. However, it is also possible to implement energy- and temperature-dependent relaxation times corresponding to specific electron scattering processes and thus to calculate their relative transport properties.

Bibliography

1. Perera F, Nadeau K. Climate Change, Fossil-Fuel Pollution, and Children's Health. *N Engl J Med*. 2022; 386; 2303-2314. doi:10.1056/nejmra2117706

2. Curtin J, Mcinerney C, Gallachóir BÓ, Hickey C, Deane P, Deeney P. Quantifying stranding risk for fossil fuel assets and implications for renewable energy investment : A review of the literature. *Renew Sustain Energy Rev*. 2019; 116; 109402. doi:10.1016/j.rser.2019.109402

3. Gustavsson L, Nguyen T, Sathre R, Tettey UYA. Climate effects of forestry and substitution of concrete buildings and fossil energy. *Renew Sustain Energy Rev*. 2021; 136; 110435. doi:10.1016/j.rser.2020.110435

4. Mehmood U. Contribution of renewable energy towards environmental quality: The role of education to achieve sustainable development goals in G11 countries. *Renew Energy*. 2021; 178; 600-607. doi:10.1016/j.renene.2021.06.118

5. Khan K, Su CW, Rehman AU, Ullah R. Is technological innovation a driver of renewable energy? *Technol Soc*. 2022; 70; 102044. doi:10.1016/j.techsoc.2022.102044

6. Olabi AG, Abdelkareem MA. Renewable energy and climate change. *Renew Sustain Energy Rev*. 2022; 158; 112111. doi:10.1016/j.rser.2022.112111

7. Alem A, Kalogiannis T, Mierlo JV, Berecibar M. A comprehensive review of stationary energy storage devices for large scale renewable energy sources grid integration. *Renew Sustain Energy Rev*. 2022; 159; 112213. doi:10.1016/j.rser.2022.112213

8. Liu H, Fu H, Sun L, Lee C, Yeatman EM. Hybrid energy harvesting technology : From materials , structural design , system integration to applications. *Renew Sustain Energy Rev*. 2021; 137; 110473. doi:10.1016/j.rser.2020.110473

9. Zhu J, Zhu M, Shi Q, Wen F, Liu L, Dong B, Haroun A, Yang Y, Vachon P, Guo X, He T, Lee C. Progress in TENG technology — A journey from energy harvesting to nanoenergy and nanosystem. *EcoMat* 2020; 1-45. doi:10.1002/eom2.12058

10. Zou H, Zhao L, Gao Q, Zuo L, Liu F, Tan T. Mechanical modulations for enhancing energy harvesting : Principles , methods and applications. *Appl Energy*. 2019; 255; 113871. doi:10.1016/j.apenergy.2019.113871

11. Ryu H, Yoon H, Kim S. Hybrid Energy Harvesters : Toward Sustainable Energy Harvesting. *Adv. Mater.* 2019; 1802898; 1-19. doi:10.1002/adma.201802898

12. Cabeza LF, Gracia AD, Laura A. Energy & Buildings Integration of renewable technologies in historical and heritage buildings : A review.

Energy Build. 2018; 177; 96-111. doi:10.1016/j.enbuild.2018.07.058

13. Gielen D, Boshell F, Saygin D, Bazilian MD, Wagner N, Gorini R. The role of renewable energy in the global energy transformation. *Energy Strateg Rev*. 2019; 24; 38-50. doi:10.1016/j.esr.2019.01.006

14. Behabtu HA, Messagie M, Coosemans T, Berecibar M. A Review of Energy Storage Technologies' Application Potentials in Renewable Energy Sources Grid Integration. *Sustainability*. 2020; 12; 10511. doi.org/10.3390/su122410511

15. Zhang S, Michorczyk P, Pielichowska K, Pielichowski K. Renewable energy systems for building heating, cooling and electricity production with thermal energy storage. *Renew Sustain Energy Rev* 2022; 165. doi:10.1016/j.rser.2022.112560

16. Mamur H, Faruk Ö, Begum J, Ruhul M, Bhuiyan A. Thermoelectric generators act as renewable energy sources. *Clean Mater*. 2021; 2; 100030. doi:10.1016/j.clema.2021.100030

17. Li C, Jiang F, Liu C, Liu P, Xu J. Present and future thermoelectric materials toward wearable energy harvesting. *Appl Mater Today*. 2019; 15; 543-557. doi:10.1016/j.apmt.2019.04.007

18. Zoui MA, Stocholm JG, Bourouis M. A Review on Thermoelectric Generators. *Energies* 2020; 13; 3606. doi: 10.3390/en13143606

19. Goldsmid H. The physics of thermoelectric energy conversion - Chapter 1: The Seebeck and Peltier effects. Morgan & Claypool Publishers, San Rafael 2017. doi:10.1088/978-1-6817-4641-8ch1

20. Wei J, Yang L, Ma Z, Song P, Zhang M, Ma J. Review of current high-ZT thermoelectric materials. *J Mater Sci*. 2020; 55; 12642-12704. doi:10.1007/s10853-020-04949-0

21. Oliveira AD. Sugarcane technology and research - Chapter 12: Sugarcane Bagasse and Cellulose Polymer Composites. IntechOpen, Rijeja 2017. doi: 10.5772/intechopen.69564

22. Narducci D, Snyder GJ, Fanciulli C. Advances in Thermoelectricity: Foundational Issues, Materials and Nanotechnology. IOS Press, Amsterdam 2021. ISBN: 978-1-64368-172-6

23. Champier D. Thermoelectric generators: A review of applications. *Energy Convers Manag*. 2017; 140; 167-181. doi:10.1016/j.enconman.2017.02.070

24. Volta A. Nuova memoria sull'elettricità animale del Sig. Don Alessandro Volta in alcune lettere al Sig. Ab. Anton Maria Vassalli. *Annali di Chimica e Storia Naturale* 1794; 5; 132–144.

25. Seebeck TJ. Magnetische Polarisation der Metalle und Erze durch Temperatur-Differenz. Abhandlungen der Königlichen Akademie der Wissenschaften zu Berlin 1822; 265–373.

26. Peltier JCA. Nouvelles expériences sur la caloricité des courants électrique. *Annales de Chimie et de Physique*. 1834; 56; 371-386.

27. Thomson W. On a Mechanical Theory of Thermo-Electric Currents. *Proceedings of the Royal Society of Edinburgh*. 1857; 3; 91-98.

28. Ando JOH, Maran ALO, Henao NC. A review of the development and applications of thermoelectric microgenerators for energy harvesting. *Renew Sustain Energy Rev*. 2018; 91; 376-393. doi:10.1016/j.rser.2018.03.052

29. Kumar A, Bano S, Govind B, Bhardwaj A, Bhatt K, Misra DK. A Review on Fundamentals, Design and Optimization to High ZT of Thermoelectric Materials for Application to Thermoelectric Technology. *J Electron Mater*. 2021; 50; 6037-6059. doi:10.1007/s11664-021-09153-7

30. Swarnkar N. Review of Thermoelectric Materials and its Properties with Applications. *J Emerg Technol Innov Res*. 2019; 6; 131-143. ISSN-2349-5162.

31. Zhou X, Yan Y, Lu X, et al. Routes for high-performance thermoelectric materials. *Mater Today*. 2018; 21; 974-988. doi:10.1016/j.mattod.2018.03.039

32. Ashcroft NW, Mermin ND. Solid State Physics. Holt Saunders International Editions, New York 1976. ISBN:9780030839931

33. Zeier WG, Zevalkink A, Gibbs ZM, Hautier G, Kanatzidis MG, Snyder GJ. Thinking Like a Chemist: Intuition in Thermoelectric Materials. *Angew Chemie - Int Ed*. 2016; 55; 6826-6841. doi:10.1002/anie.201508381

34. Gayner C, Kar KK. Recent advances in thermoelectric materials. *Prog Mater Sci*. 2016; 83; 330-382. doi:10.1016/j.pmatsci.2016.07.002

35. Lindsay L. First Principles Peierls-Boltzmann Phonon Thermal Transport: A Topical Review. *Nanoscale Microscale Thermophys Eng*. 2016; 20; 67-84. doi:10.1080/15567265.2016.1218576

36. Gabbana A, Simeoni D, Succi S, Tripiccione R. Relativistic lattice Boltzmann methods: Theory and applications. *Phys Rep*. 2020; 863; 1-63. doi:10.1016/j.physrep.2020.03.004

37. Sootsman JR, Chung DY, Kanatzidis MG. New and old concepts in thermoelectric materials. *Angew Chemie - Int Ed*. 2009; 48; 8616-8639. doi:10.1002/anie.200900598

38. Hamid EM, Shnawah DA, Sabri MFM, Said SBM, Hassan MH, Bashir MBA, Mohamad M. A review on thermoelectric renewable energy: Principle parameters that affect their performance. *Renew Sustain Energy Rev*. 2014; 30, 337-355. doi:10.1016/j.rser.2013.10.027

39. Yang L, Chen ZG, Dargusch MS, Zou J. High Performance Thermoelectric Materials: Progress and Their Applications. *Adv Energy Mater*. 2018; 8; 1-28. doi:10.1002/aenm.201701797

40. Liu W, Hu J, Zhang S, Deng M, Han CG, Liu Y. New trends, strategies and opportunities in thermoelectric materials: A perspective. *Mater Today Phys*. 2017; 1, 50-60. doi:10.1016/j.mtphys.2017.06.001

41. Sun Y, Liu Y, Li R, Li Y, Bai S. Strategies to Improve the Thermoelectric Figure of Merit in Thermoelectric Functional Materials. *Front Chem*. 2022; 10; 1-22. doi:10.3389/fchem.2022.865281

42. Daembkes H. Modulation-doped Field-effect Transistors: Principles, Design, and Technology. IEEE Press: New York 1991. ISBN: 0879422556

43. Dashevsky Z, Shusterman S, Dariel MP, Drabkin I. Thermoelectric efficiency in graded indium-doped PbTe crystals. *J Appl Phys*. 2002; 92; 1425-1430. doi:10.1063/1.1490152

44. Selimefendigil F, Okulu D, Mamur H. Numerical analysis for performance enhancement of thermoelectric generator modules by using CNT–water and hybrid Ag/MgO–water nanofluids. *J Therm Anal Calorim*. 2021; 143; 1611-1621. doi:10.1007/s10973-020-09983-3

45. Zhao LD, Lo SH, Zhang Y, Sun H, Tan G, Uher C, Wolverton C, Dravid VP, Kanatzidis MG. Ultralow thermal conductivity and high thermoelectric figure of merit in SnSe crystals. *Nature*. 2014; 508; 373-377. doi:10.1038/nature13184

46. Yamini SA, Ikeda T, Lalonde A, Pei Y, Dou SX, Snyder GJ. Rational design of p-type thermoelectric PbTe: Temperature dependent sodium solubility. *J Mater Chem A*. 2013; 1; 8725-8730. doi:10.1039/c3ta11654a

47. Li JQ, Li SP, Wang QB, Wang L, Liu FS, Ao WQ. Effect of Ce-doping on thermoelectric properties in PbTe alloys prepared by spark plasma sintering. *J Electron Mater*. 2011; 40; 2063-2068. doi:10.1007/s11664-011-1715-9

48. Pei Y, Lalonde AD, Heinz NA, Iwanaga S,Wang H, Chen L, Snyder GJ. Stabilizing the optimal carrier concentration for high thermoelectric efficiency. *Adv Mater*. 2011; 23; 5674-5678. doi:10.1002/adma.201103153

49. Pei Y, Shi X, Lalonde A, Wang H, Chen L, Snyder GJ. Convergence of electronic bands for high performance bulk thermoelectrics. *Nature*. 2011; 473; 66-69. doi:10.1038/nature09996

50. Pei Y, Wang H, Gibbs ZM, LaLonde AD, Snyder JG. Thermopower enhancement in $Pb_{1-x}Mn_xTe$ alloys and its effect on thermoelectric efficiency. *NPG Asia Mater*. 2012; 4; 1-6. doi:10.1038/am.2012.52

51. Chen CL, Wang TH, Yu ZG, Hutabalian Y, Vankayala RK, Chen CC, Hsieh WP, Jeng HT, Wei DH, Chen YY. Modulation Doping Enables Ultrahigh Power Factor and Thermoelectric ZT in n-Type $Bi_2Te_{2.7}Se_{0.3}$. *Adv Sci*. 2022; 9; 1-12. doi:10.1002/advs.202201353

52. Ren W, Zhu H, Mao J, 1you L, Song S, Tong T, Bao J, Luo J, Wang Z, Ren Z. Manipulation of Ni Interstitials for Realizing Large Power Factor in TiNiSn-Based Materials. *Adv Electron Mater*. 2019; 5; 1-8.

doi:10.1002/aelm.201900166

53. Paul B, Rawat PK, Banerji P. Dramatic enhancement of thermoelectric power factor in PbTe:Cr co-doped with iodine. *Appl Phys Lett*. 2011; 98; 2011-2014. doi:10.1063/1.3603962

54. Gurevich YG, Kaganov MI. Theory of heat conduction in solids. *Zhurnal Eksperimentalnoi i Teoreticheskoi Fiziki*. 1979; 75; 1176-1179.

55. Klemens PG. Heat conduction in solids by phonons. *Thermochim Acta*. 1993; 218; 247-255. doi:10.1016/0040-6031(93)80426-B

56. Wu G., Guo Z., Tan X.,Wang R., Zhang Q., Hu H., Sun P., Wu J., Liu G. Q., Wu J. J. Strengthened phonon scattering and band convergence synergistically realize the high-performance SnTe thermoelectric. *J Mater Chem A.* 2023; 11; 2; 649-656. doi:10.1039/D2TA08600J

57. Nag S, Saini A, Singh R, Kumar R. Influence of vacancy defects on the thermoelectric performance of SnSe sheet. *Phys E Low-Dimensional Syst Nanostructures*. 2021; 134; 114814. doi:10.1016/j.physe.2021.114814

58. Tan G, Shi F, Hao S, et al. Codoping in SnTe: Enhancement of thermoelectric performance through synergy of resonance levels and band convergence. *J Am Chem Soc*. 2015; 137; 5100-5112. doi:10.1021/jacs.5b00837

59. Tan G, Wang S, Tang X. High thermoelectric figure of merit of p-type ternary unfilled skutterudite $FeSb_2Te$ via ge doping. *Sci Adv Mater*. 2013; 5; 1974-1982. doi:10.1166/sam.2013.1665

60. Giaremis S, Kioseoglou J, Desmarchelier P, Tanguy A, Isaiev M, Belabbas I, Komninou P, Termentzidis K. Decorated Dislocations against Phonon Propagation for Thermal Management. *ACS Appl Energy Mater*. 2020; 3; 2682-2694. doi:10.1021/acsaem.9b02368

61. Karthikeyan V, Arava CM, Hlaing MZ, et al. Dislocation-induced ultra-low lattice thermal conductivity in rare earth doped β-Zn_4Sb_3. *Scr Mater*. 2020; 174; 95-101. doi:10.1016/j.scriptamat.2019.08.037

62. Hicks L, Dresselhaus M.S. Thermoelectric figure of merit of a one-dimensional conductor. *Phys Rev B.* 1993; 47; 8-11. doi:10.1103/PhysRevB.47.16631

63. Hicks L, Dresselhaus M.S. Effect of quantum-well structures on the thermoelectric figure of merit. *Phys Rev B.* 1993; 47; 12727. doi:10.1103/ PhysRevB.47.12727.

64. Zlatic V, Hewson AC. Properties and Applications of Thermoelectric Materials - Chapter: Role of Structures on Thermal Conductivity in Thermoelectric Materials. *NATO Science for Peace and Security Series B: Physics and Biophysics.* Springer, Dordrecht 2009. doi: 10.1007/978-90-481-2892-1_2

65. Qiu L, Zhu N, Feng Y, Michaelides EE, Żyła G, Jing D, Zhang X, Norris

PM, Markides CN, Mahian O. A review of recent advances in thermophysical properties at the nanoscale: From solid state to colloids. *Phys Rep*. 2020; 843; 1-81. doi:10.1016/j.physrep.2019.12.001

66. Edvinsson T. Optical quantum confinement and photocatalytic properties in two-, one- and zerodimensional nanostructures. *R Soc Open Sci*. 2018; 5. doi:10.1098/rsos.180387

67. Mao J, Liu Z, Ren Z. Size effect in thermoelectric materials. *npj Quantum Mater*. 2016; 1; 1-9. doi:10.1038/npjquantmats.2016.28

68. Eivari HA, Sohbatzadeh Z, Mele P, Assadi MHN. Low thermal conductivity: fundamentals and theoretical aspects in thermoelectric applications. *Mater Today Energy*. 2021; 21; 100744. doi:10.1016/j.mtener.2021.100744

69. Cai B, Hu H, Zhuang HL, Li JF. Promising materials for thermoelectric applications. *J Alloys Compd*. 2019; 806; 471-486. doi:10.1016/j.jallcom.2019.07.147

70 . Caballero-Calero O, Ares JR, Martín-González M. Environmentally Friendly Thermoelectric Materials: High Performance from Inorganic Components with Low Toxicity and Abundance in the Earth. *Adv Sustain Syst*. 2021; 5. doi:10.1002/adsu.202100095

71. Kruszewski MJ, Ciupinski L, Zybala R. Review of rapid fabrication methods of skutterudite materials. *Mater Today Proc*. 2019; 44; 3475-3482. doi:10.1016/j.matpr.2020.05.808

72. Chen LD, Kawahara T, Tang XF, Goto T, Hirai T. Anomalous barium filling fraction and n-type thermoelectric performance of $BayCo_4Sb_{12}$. *J Appl Phys*. 2001; 90; 1864-1868. doi:10.1063/1.1388162

73. Guo JQ, Geng HY, Ochi T, Suzuki S, Kikuchi M, Yamaguchi Y, Ito S. Development of skutterudite thermoelectric materials and modules. *J Electron Mater*. 2012; 41; 1036-1042. doi:10.1007/s11664-012-1958-0

74. Liu ZY, Zhu JL, Tong X, Niu S, Zhao WY. A review of $CoSb_3$-based skutterudite thermoelectric materials. *J Adv Ceram*. 2020; 9; 647-673. doi:10.1007/s40145-020-0407-4

75. Rogl G, Rogl P. Skutterudites, a most promising group of thermoelectric materials. *Curr Opin Green Sustain Chem*. 2017; 4; 50-57. doi:10.1016/j.cogsc.2017.02.006

76. Nolas GS, Morelli DT, Tritt TM. Skutterudites: a phonon-glass-electron crystal approach to advanced thermoelectric energy conversion applications. *Annu Rev Mater Sci*. 1999; 29; 89-116. doi:10.1146/annurev.matsci.29.1.89

77. Nolas GS, Kaeser M, Littleton IV RT, Tritt TM. High figure of merit in partially filled ytterbium skutterudite materials. *Appl Phys Lett*. 2000; 77; 1855-1857. doi:10.1063/1.1311597

78. Rull-Bravo M, Moure A, Fernández JF, Martín-González M. Skutterudites as thermoelectric materials: revisited. *RSC Adv.* 2015; 5; 52; 41653-41667.

doi: 10.1039/C5RA03942H

79. Sales BC, Mandrus D, Williams RK. Filled Skutterudite Antimonides: A New Class of Thermoelectric Materials. *Science.* 1996; 272; 1325-1328. doi: 10.1126/science.272.5266.1325

80. Zhang H, Ma W, Xie B, Zhang L, Dong S, Fan P, Wang K, Koruza J, Rödel J. $(Na_{1/2}Bi_{1/2})TiO_3$-based lead-free co-fired multilayer actuators with large strain and high fatigue resistance. *J Am Ceram Soc*. 2019; 102; 6147-6155. doi:10.1111/jace.16499

81. Shi X, Salvador JR, Yang J, Wang H. Thermoelectric properties of n-type multiple-filled skutterudites. *J Electron Mater*. 2009; 38; 930-933. doi:10.1007/s11664-008-0650-x

82. Shi X, Yang J, Salvador JR, Chi M, Cho JY, Wang H, Bai S, Yang J, Zhang W, Chen L. Multiple-filled skutterudites: High thermoelectric figure of merit through separately optimizing electrical and thermal transports. *J Am Chem Soc*. 2011; 13; 7837-7846. doi:10.1021/ja111199y

83. Momma K, Ikeda T, Nishikubo K, Takahashi N, Honma C, Takada M, Furukawa Y, Nagase T, Kudoh Y. New silica clathrate minerals that are isostructural with natural gas hydrates. *Nat Commun*. 2011; 2; 196-197. doi:10.1038/ncomms1196

84. Dolyniuk JA, Owens-Baird B, Wang J, Zaikina JV, Kovnir K. Clathrate thermoelectrics. *Mater Sci Eng R Reports*. 2016; 108; 1-46. doi:10.1016/j.mser.2016.08.001

85. Christensen M, Johnsen S, Iversen BB. Thermoelectric clathrates of type i. *Dalt Trans*. 2010; 39; 978-992. doi:10.1039/b916400f

86. Zhang Y, Brorsson J, Qiu R, Palmqvist AEC. Enhanced Thermoelectric Performance of $Ba_8Ga_{16}Ge_{30}$ Clathrate by Modulation Doping and Improved Carrier Mobility. *Adv Electron Mater*. 2021; 7. doi:10.1002/aelm.202000782

87. Anno H, Yamada H, Nakabayashi T, Hokazono M, Shirataki R. Gallium composition dependence of crystallographic and thermoelectric properties in polycrystalline type-I $Ba_8Ga_xSi_{46-x}$ (nominal x=14-18) clathrates prepared by combining arc melting and spark plasma sintering methods. *J Solid State Chem*. 2012; 193; 94-104. doi:10.1016/j.jssc.2012.03.069

88. Yu J, Xing Y, Hu C, Huang Z, Qiu Q, Wang C, Xia K, Wang Z, Bai S, Zhao X, Chen L, Zhu T. Half-Heusler Thermoelectric Module with High Conversion Efficiency and High Power Density. *Adv Energy Mater*. 2020; 10; 39-41. doi:10.1002/aenm.202000888

89. Xing Y, Liu R, Liao J, Zhang Q, Xia X, Wang C, Huang H, Chu J, Gu M, Zhu T, Zhu C, Xu F, Yao D, Zeng Y, Bai S, Uher C, Chen L. High-efficiency half-Heusler thermoelectric modules enabled by self-propagating synthesis and topologic structure optimization. *Energy Environ Sci*. 2019; 12; 3390-3399. doi:10.1039/c9ee02228g

90. Xia K, Hu C, Fu C, Zhao X, Zhu T. Half-Heusler thermoelectric materials. *Appl Phys Lett*. 2021; 118. doi:10.1063/5.0043552

91. Poon SJ. Half Heusler compounds: Promising materials for mid-to-high temperature thermoelectric conversion. *J Phys D Appl Phys*. 2019; 52. doi:10.1088/1361-6463/ab3d71

92. Bos JW. Thermoelectric Energy Conversion. Theories and Mechanisms, Materials, Devices, and Applications - Chapter 2.3: Recent developments in half-Heusler thermoelectric materials. Elsevier, Amsterdam 2021. doi:10.1016/B978-0-12-818535-3.00014-1

93. Kawaharada Y, Kurosaki K, Muta H, Uno M, Yamanaka S. High temperature thermoelectric properties of $CoNb_{1-x}Hf_xSn_{1-y}Sb_y$ half-Heusler compounds. *J Alloys Compd*. 2004; 377; 312-315. doi:10.1016/j.jallcom.2004.02.017

94. Wang SH, Cheng HM, Wu RJ, Chao WH. Structural and thermoelectric properties of HfNiSn half-Heusler thin films. *Thin Solid Films*. 2010; 518; 5901-5904. doi:10.1016/j.tsf.2010.05.080

95. Shutoh N, Sakurada S. Thermoelectric properties of the $Ti_x(Zr_{0.5}Hf_{0.5})_{1-x}NiSn$ half-Heusler compounds. *J Alloys Compd*. 2005; 389; 204-208. doi:10.1016/j.jallcom.2004.05.078

96. Lee PJ, Chao LS, High-temperature thermoelectric properties of $Ti_{0.5}(ZrHf)_{0.5-x}Nb_xNi_{0.9}Pd_{0.1}Sn_{0.98}Sb_{0.02}$ half-Heusler alloys. *J Alloys Compd* 2010; 504; 192-196. doi:10.1016/j.jallcom.2010.05.086.

97. Shi Y, Sturm C, Kleinke H. Chalcogenides as thermoelectric materials. *J Solid State Chem*. 2019; 270; 273-279. doi:10.1016/j.jssc.2018.10.049

98. Qin C, Cheng L, Xiao Y, Wen C, Ge B, Li W, Pei Y. Substitutions and dislocations enabled extraordinary n-type thermoelectric PbTe. *Mater Today Phys*. 2021; 17; 100355. doi:10.1016/j.mtphys.2021.100355

99. Su CH. Design, growth and characterization of PbTe-based thermoelectric materials. *Prog Cryst Growth Charact Mater*. 2019; 65; 47-94. doi:10.1016/j.pcrysgrow.2019.04.001

100. He J, Sootsman JR, Girard SN, Zheng JC, Wen J, Zhu Y, Kanatzidis MG, Dravid VP. On the origin of increased phonon scattering in nanostructured pbte based thermoelectric materials. *J Am Chem Soc*. 2010; 132; 8669-8675. doi:10.1021/ja1010948

101. Xiao Y, Zhao LD. Charge and phonon transport in PbTe-based thermoelectric materials. *npj Quantum Mater*. 2018; 3. doi:10.1038/s41535-018-0127-y

102. Liu HT, Sun Q, Zhong Y, Deng Q, Gan L, Lv FL, Shi XL, Chen ZG, Ang R. High-performance in n-type PbTe-based thermoelectric materials achieved by synergistically dynamic doping and energy filtering. *Nano Energy*. 2022; 91; 106706. doi:10.1016/j.nanoen.2021.106706

103. Chen Y, Hou X, Ma C, Dou Y, Wu W. Review of Development Status of Bi_2Te_3-Based Semiconductor Thermoelectric Power Generation. *Adv Mater Sci Eng*. 2018. doi:10.1155/2018/1210562

104. Mamur H, Bhuiyan MRA, Korkmaz F, Nil M. A review on bismuth telluride (Bi_2Te_3) nanostructure for thermoelectric applications. *Renew Sustain Energy Rev*. 2018; 82; 4159-4169. doi:10.1016/j.rser.2017.10.112

105. Hong M, Chen ZG, Zou J. Fundamental and progress of Bi_2Te_3-based thermoelectric materials. *Chinese Phys B*. 2018; 27. doi:10.1088/1674-1056/27/4/048403

106. Pei J, Cai B, Zhuang HL, Li JF. Bi_2Te_3-based applied thermoelectric materials: Research advances and new challenges. *Natl Sci Rev*. 2020; 7; 1856-1858. doi:10.1093/nsr/nwaa259

107. Saberi Y, Sajjadi SA. A comprehensive review on the effects of doping process on the thermoelectric properties of Bi_2Te_3 based alloys. *J Alloys Compd*. 2022; 904; 163918. doi:10.1016/j.jallcom.2022.163918

108. Tewari A, Dixit S, Sahni N, Bordas SPA. Machine learning approaches to identify and design low thermal conductivity oxides for thermoelectric applications. *Data-Centric Eng*. 2020; 1. doi:10.1017/dce.2020.7

109. Acharya M, Jana SS, Ranjan M, Maiti T. High performance (ZT>1) n-type oxide thermoelectric composites from earth abundant materials. *Nano Energy*. 2021; 84; 105905. doi:10.1016/j.nanoen.2021.105905

110. Boston R, Schmidt WL, Lewin GD, Iyasara AC, Lu Z, Zhang H, Sinclair DC, Reaney IM. Protocols for the fabrication, characterization, and optimization of n-type thermoelectric ceramic oxides. *Chem Mater*. 2017; 29; 265-280. doi:10.1021/acs.chemmater.6b03600

111. Ren GK, Lan J Le, Ventura KJ, Tan X, Lin YH, Nan CW. Contribution of point defects and nano-grains to thermal transport behaviours of oxide-based thermoelectrics. *npj Comput Mater*. 2016; 2; 1-9. doi:10.1038/npjcompumats.2016.23

112. Sun Y, Di CA, Xu W, Zhu D. Advances in n-Type Organic Thermoelectric Materials and Devices. *Adv Electron Mater*. 2019; 5; 1-27. doi:10.1002/aelm.201800825

113. Zeng YJ, Wu D, Cao XH, Zhou WX, Tang LM, Chen KQ. Nanoscale Organic Thermoelectric Materials: Measurement, Theoretical Models, and Optimization Strategies. *Adv Funct Mater*. 2020; 30. doi:10.1002/adfm.201903873

114. Zhang Y, Wang W, Zhang F, Dai K, Li C, Fan Y, Chen G, Zheng Q. Soft Organic Thermoelectric Materials: Principles, Current State of the Art and Applications. *Small*. 2022; 18. doi:10.1002/smll.202104922

115. Deng L, Liu Y, Zhang Y, Wang S, Gao P. Organic Thermoelectric Materials: Niche Harvester of Thermal Energy. *Adv Funct Mater*. 2023; 33.

doi:10.1002/adfm.202210770

116. Zhao Y, Liu L, Zhang F, Di C, Zhu D. Advances in organic thermoelectric materials and devices for smart applications. *SmartMat*. 2021; 2; 426-445. doi:10.1002/smm2.1034

117. Lee S, Kim S, Pathak A, Tripathi A, Qiao T, Lee Y, Lee H, Woo HY. Recent Progress in Organic Thermoelectric Materials and Devices. *Macromol Res*. 2020; 28; 531-552. doi:10.1007/s13233-020-8116-y

118. Li J, Huckleby AB, Zhang M. Polymer-based thermoelectric materials: A review of power factor improving strategies. *J Mater*. 2022; 8; 204-220. doi:10.1016/j.jmat.2021.03.013

119. Yao CJ, Zhang HL, Zhang Q. Recent progress in thermoelectric materials based on conjugated polymers. *Polymers (Basel)*. 2019; 11; 1-19. doi:10.3390/polym11010107

120. Lu Y, Wang JY, Pei J. Strategies to Enhance the Conductivity of n-Type Polymer Thermoelectric Materials. *Chem Mater*. 2019; 31; 6412-6423. doi:10.1021/acs.chemmater.9b01422

121. Wang S, Zuo G, Kim J, Sirringhaus H. Progress of Conjugated Polymers as Emerging Thermoelectric Materials. *Prog Polym Sci*. 2022; 129; 101548. doi:10.1016/j.progpolymsci.2022.101548

122. Wang J, Mu X, Sun M. The thermal, electrical and thermoelectric properties of graphene nanomaterials. *Nanomaterials*. 2019; 9. doi:10.3390/nano9020218

123. Schedin F, Geim AK, Morozov SV, Hill EW, Blake P, Katsnelson MI, Novoselov KS. Detection of individual gas molecules adsorbed on graphene. *Nat Mater*. 2007; 6; 652-655. doi:10.1038/nmat1967

124. Markov M, Zebarjadi M. Thermoelectric transport in graphene and 2D layered materials. *Nanoscale Microscale Thermophys Eng*. 2019; 23; 117-127. doi:10.1080/15567265.2018.1520762

125. Novak TG, Kim J, Kim J, Tiwari AP, Shin H, Song JY, Jeon S. Complementary n-Type and p-Type Graphene Films for High Power Factor Thermoelectric Generators. *Adv Funct Mater*. 2020; 30. doi:10.1002/adfm.202001760

126. Zeng H, Dai J, Yao W, Xiao D, Cui X. Valley polarization in MoS_2 monolayers by optical pumping. *Nat Nanotechnol*. 2012; 7; 490-493. doi:10.1038/nnano.2012.95

127. Ithurria S, Tessier MD, Mahler B, Lobo RPSM, Dubertret B, Efros AL. Colloidal nanoplatelets with two-dimensional electronic structure. *Nat Mater*. 2011; 10; 936-941. doi:10.1038/nmat3145

128. Mak KF, He K, Shan J, Heinz TF. Control of valley polarization in monolayer MoS_2 by optical helicity. *Nat Nanotechnol*. 2012; 7; 494-498. doi:10.1038/nnano.2012.96

129. Jaramillo TF, Jørgensen KP, Bonde J, Nielsen JH, Horch S, Chorkendorff IB. Identification of Active Edge Sites for Electrochemical H_2 Evolution from MoS_2 Nanocatalysts, *Science* 2007; 317; 100-102. doi:10.1126/science.1141483

130. Rapoport L, Bilik Y, Feldman Y, Homyonfer M, Cohen SR, Tenne R. Hollow nanoparticles of WS_2 as potential solid-state lubricants. *Nature*. 1997; 387; 791–793. doi:10.1038/42910

131. Zhang X, Guo Y, Zhou Z, Li Y, Chen Y, Wang J. A general strategy for designing two-dimensional high-efficiency layered thermoelectric materials. *Energy Environ. Sci.*; 2021; 14; 7; 4059-4066 doi:10.1039/D1EE00356A.

132. Kumar R, Singh R. Thermoelectricity and advanced thermoelectric materials - Chapter: Two-dimensional (2D) thermoelectric materials. *Elsevier*, Amsterdam. doi: 10.1016/B978-0-12-819984-8.00006-0

133. Samanta M, Ghosh T, Chandra S, Biswas K. Layered materials with 2D connectivity for thermoelectric energy conversion. *J Mater Chem A*. 2020; 8; 12226-12261. doi:10.1039/d0ta00240b

134. Li D, Gong Y, Chen Y, Lin J, Khan Q, Zhang Y, Li Y, Zhang H, Xie H. Recent Progress of Two-Dimensional Thermoelectric Materials. *Nano-Micro Letters*. 2020. doi:10.1007/s40820-020-0374-x

135. Wang S, Cavin J, Hemmat Z, Kumar K, Ruckel A, Majidi L, Gholivand H, Dawood R, Cabana J, Guisinger N, Klie RF, Khalili-Araghi F, Mishra R, Salehi-Khojin A. Phase-Dependent Band Gap Engineering in Alloys of Metal-Semiconductor Transition Metal Dichalcogenides. *Adv Funct Mater*. 2020; 30. doi:10.1002/adfm.202004912

136. Kistanov AA, Shcherbinin SA, Botella R, Davletshin A, Cao W. Family of Two-Dimensional Transition Metal Dichlorides: Fundamental Properties, Structural Defects, and Environmental Stability. *J Phys Chem Lett* 2022; 13; 2165-2172.doi:10.1021/acs.jpclett.2c00367

137. Chhowalla M, Shin HS, Eda G, Li LJ, Loh KP, Zhang H. The chemistry of two-dimensional layered transition metal dichalcogenide nanosheets. *Nat Chem*. 2013; 5; 263-275. doi:10.1038/nchem.1589

138. Imai H, Shimakawa Y, Kubo Y. Large thermoelectric power factor in TiS_2 crystal with nearly stoichiometric composition. *Phys Rev B - Condens Matter Mater Phys*. 2001; 64; 2-5. doi:10.1103/PhysRevB.64.241104

139. Abbott EE, Kolis JW, Lowhorn ND, Sams W, Rao A, Tritt TM. Thermoelectric properties of doped titanium disulfides. *Appl Phys Lett*. 2006; 88; 1-4. doi:10.1063/1.2217190

140. Conroy LE, Park KC. Electrical properties of the Group IV disulfides, titanium disulfide, zirconium disulfide, hafnium disulfide and tin disulfide. *Inorg Chem* 1968; 7; 459-463. doi:10.1021/ic50061a015

141. Veluswamy P, Subramanian S, Hassan M, Yavuz CT, Ryu HJ, Cho BJ.

Design of low cost, scalable, and high-performance TiS_2 thermoelectric materials via wet ball-milling process. *J Mater Sci Mater Electron*. 2022; 33; 8822-8832. doi:10.1007/s10854-021-06914-2

142. Chen K, Song M, Sun YY, Xu H, Qi DC, Su Z, Gao X, Xu Q, Hu J, Zhu J, Zhang R, Wang J, Zhang L, Cao L, Han Y, Xiong Y. Defects controlled doping and electrical transport in TiS_2 single crystals. *Appl Phys Lett*. 2020; 116; 1-6. doi:10.1063/5.0005170

143. Wilson JA, Yoffe AD. The transition metal dichalcogenides discussion and interpretation of the observed optical, electrical and structural properties. *Adv Phys*. 1969; 18; 193-335. doi:10.1080/00018736900101307

144. Kratzer P, Neugebauer J. The basics of electronic structure theory for periodic systems. *Front Chem*. 2019; 7. doi:10.3389/fchem.2019.00106

145. Chhowalla M, Liu Z, Zhang H. Two-dimensional transition metal dichalcogenide (TMD) nanosheets. *Chem Soc Rev*. 2015; 44; 2584-2586. doi:10.1039/c5cs90037a

146. Yuan H, Wang H, Cui Y. Two-dimensional layered chalcogenides: From rational synthesis to property control via orbital occupation and electron filling. *Acc Chem Res*. 2015; 48; 81-90. doi:10.1021/ar5003297

147. Zhang RZ, Wan CL, Wang YF, Koumoto K. Titanium sulphene: Two-dimensional confinement of electrons and phonons giving rise to improved thermoelectric performance. *Phys Chem Chem Phys*. 2012; 14; 15641-15644. doi:10.1039/c2cp42949g

148. Özbal G, Senger RT, Sevik C, Sevinçli H. Ballistic thermoelectric properties of monolayer semiconducting transition metal dichalcogenides and oxides. *Phys Rev B*. 2019; 100; 1-10. doi:10.1103/PhysRevB.100.085415

149. Dryfe RAW. 2D transition metal chalcogenides and van der Waals heterostructures: Fundamental aspects of their electrochemistry. *Curr Opin Electrochem*. 2019; 13; 119-124. doi:10.1016/j.coelec.2018.11.021

150. Novoselov KS, Geim AK, Morozov SV, Jiang D, Katsnelson MI, Grigorieva IV, Dudonos SV, Firsov AA. Two-dimensional gas of massless Dirac fermions in graphene. *Nature*. 2005; 438; 197-200. doi:10.1038/nature04233

151. Yang D, Frindt RF. Li-intercalation and exfoliation of WS_2. *J Phys Chem Solids*. 1996; 57; 1113-1116. doi:10.1016/0022-3697(95)00406-8

152. Nicolosi V, Chhowalla M, Kanatzidis MG, Strano MS, Coleman JN. Liquid exfoliation of layered materials. *Science.* 2013; 340. doi:10.1126/science.1226419

153. Jung Y, Zhou Y, Cha JJ. Intercalation in two-dimensional transition metal chalcogenides. *Inorg Chem Front*. 2016; 3; 452-463. doi:10.1039/c5qi00242g

154. Zhou J, Lin Z, Ren H, Duan X, Shakir I, Huang Y, Duan X. Layered Intercalation Materials. *Adv Mater*. 2021; 33; 1-23.

doi:10.1002/adma.202004557

155. Stark MS, Kuntz KL, Martens SJ, Warren SC. Intercalation of Layered Materials from Bulk to 2D. *Adv Mater*. 2019; 31; 1-47. doi:10.1002/adma.201808213

156. Cui H, Guo Y, Ma W, Zhou Z. 2D Materials for Electrochemical Energy Storage: Design, Preparation, and Application. *ChemSusChem*. 2020; 13; 1155-1171. doi:10.1002/cssc.201903095

157. Yang B, Tamirat AG, Bin D, Yao Y, Lu H, Xia Y. Regulating Intercalation of Layered Compounds for Electrochemical Energy Storage and Electrocatalysis. *Adv Funct Mater.* 2021; 31; 2104543. doi: 10.1002/adfm.202104543

158. Kim JY, Park J, Kang SH, Jung S, Shin DO, Lee MJ, Oh J, Kim KM, Zausch J, Lee YG, Lee YM. Revisiting TiS_2 as a diffusion-dependent cathode with promising energy density for all-solid-state lithium secondary batteries. *Energy Storage Mater*. 2021; 41; 289-296. doi:10.1016/j.ensm.2021.06.005

159. Trevey JE, Stoldt CR, Lee SH. High Power Nanocomposite TiS_2 Cathodes for All-Solid-State Lithium Batteries. *J Electrochem Soc*. 2011; 158; A1282. doi:10.1149/2.017112jes

160. Chung SH, Manthiram A. A Li_2S-TiS_2-Electrolyte Composite for Stable Li_2S-Based Lithium–Sulphur Batteries. *Adv Energy Mater*. 2019; 9; 1-9. doi:10.1002/aenm.201901397

161. Tchitchekova DS, Ponrouch A, Verrelli R, Broux T, Frontera C, Sorrentino A, Barde F, Biškup N, Arroyo-de Dompablo ME, Palacin MR. Electrochemical Intercalation of Calcium and Magnesium in TiS_2: Fundamental Studies Related to Multivalent Battery Applications. *Chem Mater*. 2018; 30; 847-856. doi:10.1021/acs.chemmater.7b04406

162. Tian R, Wan C, Wang Y, Wei Q, Ishida T, Yamamoto A, Tsuruta A, Shin W, Li S, Koumoto K. A solution-processed TiS_2/organic hybrid superlattice film towards flexible thermoelectric devices. *J Mater Chem A*. 2017; 5; 564-570. doi:10.1039/c6ta08838d

163. Du Y, Xu J, Paul B, Eklund P. Flexible thermoelectric materials and devices. *Appl Mater Today*. 2018; 12; 366-388. doi:10.1016/j.apmt.2018.07.004

164. Wan C, Wang Y, Wang N, Norimatsu W, Kusunoki M, Koumoto K. Development of novel thermoelectric materials by reduction of lattice thermal conductivity. *Sci Technol Adv Mater*. 2010; 11. doi:10.1088/1468-6996/11/4/044306

165. Liang J, Yin S, Wan C. Hybrid Thermoelectrics. *Annu Rev Mater Res.* 2020; 50; 1; 319-344. doi:10.1146/annurev-matsci-082319-111001

166. Wan C, Gu X, Dang F, Itoh T, Wang Y, Sasaki H, Kondo M, Koga K, Yabuki K, Snyder GJ, Yang R, Koumoto K. Flexible n-type thermoelectric materials by organic intercalation of layered transition metal dichalcogenide TiS_2. *Nat*

Mater. 2015; 14; 622-627. doi:10.1038/nmat4251

167. Wan C, Tian R, Kondou M, Yang R, Zong P, Koumoto K. Ultrahigh thermoelectric power factor in flexible hybrid inorganic-organic superlattice. *Nat Commun*. 2017; 8. doi:10.1038/s41467-017-01149-4

168. Ferhat S, Domain C, Vidal J, Noël D, Ratier B, Lucas B. Flexible thermoelectric device based on $TiS_2(HA)_x$ n-type nanocomposite printed on paper. *Org Electron*. 2019; 68; 256-263. doi:10.1016/j.orgel.2019.02.031

169. Liu Y, Wang W, Yang J, Li S. Recent Advances of Layered Thermoelectric Materials. *Adv Sustain Syst*. 2018; 2; 1-15. doi:10.1002/adsu.201800046

170. Jin H, Li J, Iocozzia J, Zeng X, Wei PC, Yang C, Li N, Liu Z, He JH, Zhu T, Wang J, Lin Z, Wang S. Hybrid Organic-Inorganic Thermoelectric Materials and Devices. *Angew Chem Int Ed*; 2019. doi:10.1002/anie.201901106

171. Zhang P, Deng B, Sun W, Zheng Z, Liu W. Fiber-based thermoelectric materials and devices for wearable electronics. *Micromachines*. 2021; 12; 1-15. doi:10.3390/mi12080869

172. Suarez F, Nozariasbmarz A, Vashaee D, Öztürk MC. Designing thermoelectric generators for self-powered wearable electronics. *Energy Environ Sci*. 2016; 9; 2099-2113. doi:10.1039/c6ee00456c

173. Shi XL, Chen WY, Zhang T, Zou J, Chen ZG. Fiber-based thermoelectrics for solid, portable, and wearable electronics. *Energy Environ Sci.*; 2021; 14; 729-764. doi:10.1039/D0EE03520C,

174. Nozariasbmarz A, Collins H, Dsouza K, Polash M, Hosseini M, Hylard M, Liu J, Malhorta A, Ortiz F, Mohaddes F, Ramesh V, Sargolzaeiaval Y, Snouwaert N, Ozturk M, Vashaee D. Review of wearable thermoelectric energy harvesting: From body temperature to electronic systems. *Appl Energy*. 2020; 258; 114069. doi:10.1016/j.apenergy.2019.114069

175. Koumoto K, Tian R, Yang R, Wan C. Inorganic/organic hybrid superlattice materials. *Mater Asp Thermoelectr*. 2016; 501-518. doi:10.1201/9781315197029

176. Rietveld HM. The Rietveld method. *Phys Scr*. 2014; 89. doi:10.1088/0031-8949/89/9/098002

177. Young RA. The Rietveld Method. Oxford University Press, Oxford, England 1993. doi:10.1017/S0885715600019497

178. Tassone F, Mauri F, Car R. Acceleration schemes for ab initio molecular-dynamics simulations and electronic-structure calculations. *Phys Rev B Condens Matter* 1994; 50; 10561-10573. doi: 10.1103/PhysRevB.50.10561

179. Woods N. On the Nature of Self-Consistency in Density Functional Theory. *arXiv* 2018. doi: 10.48550/arXiv.1803.01763

180. Wang L, Wang G, Duan Z, Lou H, Sun M. Optimizing the Topology of

Bayesian Network Classifiers by Applying Conditional Entropy to Mine Causal Relationships Between Attributes. *IEEE Access*. 2019; 7; 134271-134279. doi:10.1109/ACCESS.2019.2940879

181. Aarons J, Sarwar M, Thompsett D, Skylaris CK. Perspective : Methods for large-scale density functional calculations on metallic systems. *J Chem Phys* 2016; 145; 220901. doi:10.1063/1.4972007

182. Umrigar C, Ellis DE, Wang D, Krakauer H, Posternak M. Band structure, intercalation, and interlayer interactions of transition-metal dichalcogenides: TiS_2 and $LiTiS_2$. *Phys Rev B* 1982; 26; 4935-4950. doi: 10.1103/physrevb.26.4935

183. Reshak AH. Copper-Intercalated TiS_2 : Electrode Materials for Rechargeable Batteries as Future Power Resources. *J Phys Chem A.* 2009; 2; 1635-1645. doi: 10.1021/jp810242w

184. Wilson AJC. Imperfections in the structure of cobalt II . Mathematical treatment of proposed structure. *Proc R Soc Lond* 1942; A180; 277-285. doi: 10.1098/rspa.1942.0040

185. Jagodzinski H. Eindimensionale Fehlordnung in Kristallen und ihr Einfluss auf die Röntgeninterferenzen. II. Berechnung der fehlgeordneten dichtesten Kugelpackungen mit Wechselwirkungen der Reichweite 3. *Acta Cryst* 1949; 2; 208-214. doi:10.1107/S0365110X49000564

186. Hosemann R. Die parakristalline Feinstruktur naturlicher und synthetischer Eiweisse. Visuelles Naherungsverfahren zur Bestimmung der Schwankungstensoren von Gitterzellen, *Acta Cryst* 1951; 4; 520-530. doi: 10.1107/S0365110X51001744

187. Ranjan P, Gaur S, Yadav H, Urgunde AB, Singh V, Patel A. 2D materials : increscent quantum flatland with immense potential for applications. *Nano Converg*. 2022; 9; 26. doi:10.1186/s40580-022-00317-7

188. Novoselov KS, Geim SV, Morozov SV, Jiang D, Zhang Y, Dubonos SV, Grigorieva IV, Firsov AA. Electric Field Effect in Atomically Thin Carbon Films. *Science.* 2004; 306; 666-669. doi:10.1126/science.1102896

189. Li X, Chen C, Yang Y, Lei Z, Xu H. 2D Re-Based Transition Metal Chalcogenides : Progress , Challenges , and Opportunities. *Adv Sci.* 2020; 7; 2002320. doi:10.1002/advs.202002320

190. Snure M, Motala MJ, Prusnick TA, Smith EM, Moore D, Muratore C, Vangala SR, Glavin NR. Two step synthesis of ultrathin transition metal tellurides. *J Vac Sci Technol.* 2022; A40; 042202. doi: 10.1116/6.0001893

191. Xu R, Zou X, Liu B, Cheng H. Computational design and property predictions for two-dimensional nanostructures. *Mater Today.* 2018; 21; 391-418. doi:10.1016/j.mattod.2018.03.003

192. Xiong L, Wang K, Li D, Luo X, Weng J, Liu Z, Zhang H. Research progress on the preparations, characterizations and applications of large scale 2D

transition metal dichalcogenides films. *FlatChem*. 2020; 21; 100161. doi:10.1016/j.flatc.2020.100161

193. Upadhyay SN, Akash J, Satrughna K, Pakhira S. Recent advancements of two-dimensional transition metal dichalcogenides and their applications in electrocatalysis and energy storage. *Emergent Mater.* 2021; 4; 951-970. doi: 10.1007/s42247-021-00241-2

194. Bertoldo FF, Unocic RR, Lin Y-C, Sang X, Puretzky AA, Yu Y, Miakota DI, Rouleau CM, Schou J, Thygesen KS, Geohegan DB, Canulescu S. Intrinsic Defects in MoS_2 Grown by Pulsed Laser Deposition : From Monolayers to Bilayers. *ACS Nano.* 2021; 15; 2858-2868. doi:10.1021/acsnano.0c08835

195. Cowie M, Plougmann R, Benkirane Y, Schué L, Schumacher Z, Grütter P. How high is a $MoSe_2$ monolayer?, *Nanotechnology.* 2021; 33; 12; 125706. doi: 10.1088/1361-6528/ac40bd

196. Yang D, Sandoval SJ, Divigalpitiya WMR, Irwin JC, Frindt RF. Structure of single-molecular-layer MoS_2. *Phys Rev B* 1991; 43; 12053-12056. doi: 10.1103/physrevb.43.12053

197. Yang D, Frindt RF. Powder x-ray diffraction of turbostratically stacked layer systems. *J Mater Res.* 1996; 11; 1733-1738. doi: 10.1557/jmr.1996.0217

198. Pakharukova VP, Yatsenko D, Gerasimov EY, Bukhtiyarova GA, Tsybulya S V. A Total Scattering Debye Function Analysis : Effective Approach for Structural Studies of Supported MoS_2 -based Hydrotreating Catalysts. *Ind Eng Chem Res.* 2020; 59; 10914-10922. doi:10.1021/acs.iecr.0c01254

199. Frey GL, Tenne R, Matthews MJ, Dresselhaus MS, Dresselhaus G. Raman and resonance Raman investigation of MoS_2 nanoparticles. *Phys Rev B.* 2000; 60; 2883-2892. doi:10.1103/PhysRevB.60.2883

200. Niefiend F, Djamil J, Bensch W, Srinivasan BR, Sinev I, Grünert W, Deng M, Kienle L, Lotnyk A, Mesch MB, Senker J, Dura L, Beweries T. Room temperature synthesis of an amorphous MoS_2 based composite stabilized by N-donor ligands and its light-driven photocatalytic hydrogen production. *RSC Adv.* 2015; 5; 67742-67751. doi:10.1039/C5RA14438H

201. Bekx-Schürmann S, Mangelsen S, Breuninger P, Antoni H, Schürmann U, Kienle L, Muhler M, Bensch W, Grünert W. Morphology, microstructure, coordinative unsaturation, and hydrogenation activity of unsupported MoS_2: How idealized models fail to describe a real sulfide material. *Appl Catal B.* 2020; 266; 118623. doi:10.1016/j.apcatb.2020.118623

202. Sanikop R, Sudakar C. Tailoring magnetically active defect sites in Tailoring Magnetically-Active Defect Sites in MoS_2 Nanosheets for Spintronics Applications. *ACS Appl Nano Mater.* 2020; 3; 1; 576-587. doi:10.1021/acsanm.9b02121

203. Novoselov KS, Jiang D, Schedin F, Booth TJ, Khotkevich VV, Morozov SV, Geim AK. Two-dimensional atomic crystals. *PNAS.* 2005; 102; 10451-

10453. doi: 10.1073/pnas.0502848102

204. Sanikop R, Budumuru AK, Gautam S, Chae KH, Sudakar C. Robust Ferromagnetism in Li-Intercalated and -Deintercalated MoS_2 Nanosheets: Implications for 2D Spintronics. *ACS Appl Nano Mater.* 2020; 3; 12; 11825-11837. doi:10.1021/acsanm.0c02349

205. Phalswal P, Khanna PK, Rubahn, HG, Mishra YK. Nanostructured molybdenum dichalcogenides: a review , *Mater Adv.* 2022; 3; 14; 5672-5697. doi: 10.1039/D2MA00150K

206. Joensen P, Frindt RF, Morrison SR. Single layer MoS_2. *Mat Res Bull.* 1986; 21; 457-461. doi: 10.1016/0025-5408(86)90011-5

207. Joensen P, Crozier ED, Alberding N, Frindt RF. A study of single-layer and restacked MoS_2, by x-ray diffraction and x-ray absorption spectroscopy. *J Phys C: Solid State Physics*. 1987; 20; 4043. doi: 10.1088/0022-3719/20/26/009

208. Gordon RA, Yang D, Crozier ED, Jiang DT, Frindt RF. Structures of exfoliated single layers of WS_2, MoS_2, and $MoSe_2$ in aqueous suspension. *Phys Rev B.* 2002; 65; 125407. doi:10.1103/PhysRevB.65.125407

209. Petkov V, Billinge SJL, Heising J, Kanatzidis MG. Application of Atomic Pair Distribution Function Analysis to Materials with Intrinsic Disorder . Three-Dimensional Structure of Exfoliated-Restacked WS_2 : Not Just a Random Turbostratic Assembly of Layers. *J Am Chem Soc.* 2000; 122; 11571-11576. doi: 10.1021/ja002048i

210. Mangelsen S, Srinivasan BR, Schürmann U, Kienle L, Näther C, Bensch W. Nanostructured tungsten sulfides: insights into precursor decomposition and the microstructure using X-ray scattering methods. *Dalton Trans.* 2019; 48; 1184-1201. doi:10.1039/c8dt04205e

211. Pallellappa C, Ghosh S, Rovinsky L, Livneh T, Zak A. Solving the "MoS_2 Nanotubes" Synthetic Enigma and Elucidating the Route for Their Catalyst-Free and Scalable Production. *ACS Nano.* 2020; 14; 3; 3004-3016. doi:10.1021/acsnano.9b07866

212. Kisała J, Ferraria AM, Mitina N, Cieniek B, Krzemiński P, Pogocki D, Nebesnyi R, Zaichenko O, Bobitski Y. Photocatalytic activity of layered MoS2 in the reductive degradation of bromophenol blue, *RSC Adv.* 2022; 12; 35; 22465-22475. doi: 10.1039/D2RA03362C

213. Sreedhara MB, Sinha SS, Zak A, Yadgarov L, Tenne R. Nanotubes and fullerene-like nanoparticles from layered transition metal dichalcogenides : Why do they form and what is their significance ? *Z Anorg Allg Chem.* 2022; 648; e202200128. doi:10.1002/zaac.202200128

214. Constantinescu G, Kuc A, Heine T. The Stacking in Bulk and Bilayer Hexagonal Boron Nitride. *Phys Rev Lett.* 2013; 111; 036104. doi:10.1103/PhysRevLett.111.036104

215. He J, Hummer K, Franchini C. Stacking effects on the electronic and optical properties of bilayer transition metal. *Phys Rev B.* 2014; 89; 075409. doi:10.1103/PhysRevB.89.075409

216. Bampoulis P, Sotthewes K, Siekman MH, Zandvliet HJW. Local Conduction in $Mo_xW_{1-x}Se_2$: The Role of Stacking Faults, Defects and Alloying. *ACS Appl Mater Interface.* 2018; 10; 15; 13218-13225. doi:10.1021/acsami.8b01506

217. Schonfeld B, Huang JJ, Moss SC. Anisotropic Mean-Square Displacements (MSD) in Single Crystals of 2H- and 3R-MoS_2. *Acta Cryst.* 1983; B39; 404-407. doi: 10.1107/s01008768183002645

218. Kakinoki J, Komura Y. Diffraction by a One-Dimensionally Disordered Crystal . I . The Intensity Equation. A*cta Cryst.* 1965; 19; 137-147. doi:10.1107/S0365110X65002888

219. Gilbert B. Finite size effects on the real-space pair distribution function of nanoparticles research papers. *J Appl Cryst.* 2008; 41; 554-562. doi:10.1107/S0021889808007905

220. Hosemann R, Bagchi SN. The Interference Theory of Ideal Paracrystals. *Acta Cryst.* 1952; 5; 612-614. doi:10.1107/S0365110X52001702

221. Ruland W. X-ray Studies on the Structure of Graphitie Carbons. *Acta Cryst.* 1965; 18; 992-996. doi:10.1107/S0365110X65002414

222. Longo A, Martorana A. Distorted f.c.c. arrangement of gold nanoclusters : a model of spherical particles with microstrains and stacking faults. *J Appl Cryst.* 2008; 41; 446-455. doi:10.1107/S0021889808004846

223. Longo A, Sciortino L, Giannici F, Martorana A. Crossing the boundary between face-centred cubic and hexagonal close packed : the structure of nanosized cobalt is unraveled by a model accounting for shape , size distribution and stacking faults , allowing simulation of XRD , XANES and EXAFS. *J Appl Cryst.* 2014; 47; 1-7. doi:10.1107/S1600576714015970

224. Longo A, Giannici F, Sciortino L, Martorana A. A real-space approach to the analysis of stacking faults in close-packed metals: G(r) modelling and Q-space feedback. *Acta Cryst A.* 2020; 76; 84-91. doi: 10.1107/S2053273319014578

225. Cervellino A, Giannini C, Guagliardi A. On the Efficient Evaluation of Fourier Patterns for Nanoparticles and Clusters. *J Comput Chem.* 2006; 27; 995-1008. doi:10.1002/jcc.20407

226. James F, Roos M. Minuit - A system for function minimization and analysis of the parameter errors and correlations. *Comput Phys Commun.* 1975; 10; 343-367. doi: 10.1016/0010-4655(75)90039-9

227. Petkov V, Billinge SJL, Larson P, Mahanti S, Vogt T, Rangan K, Kanatzidis M. Structure of nanocrystalline materials using atomic pair distribution function analysis: Study of $LiMoS_2$. *Phys Rev B.* 2002; 65; 3-6.

doi:10.1103/PhysRevB.65.092105

228. Kakinoki J. Diffraction by a one-dimensionally disordered crystal. II. Close-packed structures. *Acta Cryst.* 1967; 23; 875-885. doi:10.1107/S0365110X67003974

229. Acerce M, Voiry D, Chhowalla M. Metallic 1T phase MoS_2 nanosheets as supercapacitor electrode materials. *Nat Nanotechnol.* 2015; 10; 313-318. doi:10.1038/nnano.2015.40

230. Wang D, Zhang X, Bao S, Zhang Z, Fei H, Wu Z. Phase engineering of a multiphasic 1T/2H MoS_2 catalyst for highly efficient hydrogen evolution. *J Mater Chem A.* 2017; 5; 2681-2688. doi:10.1039/C6TA09409K

231. Stavrou M, Chazapis N, Nikoli E, Arenal R, Tagmatarchis N, Couris S. Crystalline Phase Effects on the Nonlinear Optical Response of MoS_2 and WS_2 Nanosheets: Implications for Photonic and Optoelectronic Applications. *ACS Appl Nano Mater.* 2022; 5; 16674-16686. doi:10.1021/acsanm.2c03709

232. Parilla PA, Dillon AC, Parkinson BA, Jones KM, Alleman J, Riker G, Ginley DS, Heben MJ. Formation of Nanooctahedra in Molybdenum Disulfide and Molybdenum Diselenide Using Pulsed Laser Vaporization. *J Phys Chem B.* 2004; 108; 20; 6197-6207. doi: 10.1021/jp036202+

233. Geng X, Jiao Y, Han Y, Mukhopadhyay A, Yang L. Freestanding Metallic 1T MoS_2 with Dual Ion Diffusion Paths as High Rate Anode for Sodium-Ion Batteries. *Adv Funct Mater.* 2017; 27; 1702998; doi:10.1002/adfm.201702998

234. Ding W, Hu L, Dai J, Tang X, Wei R, Sheng Z, Liang C, Shao D, Song W, Liu Q, Chen M, Zhu X, Chou S, Zhu X, Chen Q, Sun Y, Dou SX. Highly Ambient-Stable 1T-MoS_2 and 1T-WS_2 by Hydrothermal Synthesis under High Magnetic Fields. *ACS Nano.* 2019; 13; 1694-1702. doi:10.1021/acsnano.8b07744

235. Lince JR, Hilton R, Bommannavar S. EXAFS of sputter-deposited MoS_2, films. *Thin solid films.* 1995; 264; 120-134. doi: 10.1016/0040-6090(95)06607-1

236. Tang J, Wei Z, Wang Q, Wang Y, Han B, Li X, Huang B, Liao M, Liu J, Li N, Zhao Y, Shen C, Guo Y, Bai X, Gao P, Yang W, Chen L, Wu K, Yang R, Shi D, Zhang G. In Situ Oxygen Doping of Monolayer MoS_2 for Novel Electronics. *Small.* 2020; 16; 2004276. doi:10.1002/smll.202004276

237. Prouzet E, Heising J, Kanatzidis MG. Structure of Restacked and Pillared WS_2 : An X-ray Absorption Study. *Chem Mater.* 2003; 15; 412-418

238. Trost BM. Atom Economy - A Challenge for Organic Synthesis: Homogeneous Catalysis Leads the Way. *Angew Chemie Int Ed.* 1995; 34; 259-281. doi:10.1002/anie.199502591

239. Coelho AA. TOPAS and TOPAS-Academic: An optimization program

integrating computer algebra and crystallographic objects written in C++: An. *J Appl Cryst.* 2018; 51; 210-218. doi:10.1107/S1600576718000183

240. Giannozzi P, Baroni S, Bonini N, Calandra M, Car R, Cavazzoni C, Ceresoli D, Chiarotti GL, Cococcioni M, Dado I, Dal Corso A, De Gironcoli S, Fabris S, Fratesi G, Gebauer R, Gerstmann U, Goufoussin C, Kokalj A, Lazzeri M, Martin-Samos L, Marzari N, Mauri F, Mazzarello R, Paolini S, Pasquarello A, Pauletto L, Sbraccia C, Scandolo S, Sclauzero G, Seitsonen AP, Smogunov A, Umari P, Wentzcovitch RM. QUANTUM ESPRESSO: A modular and open-source software project for quantum simulations of materials. *J Phys Condens Matter*. 2009; 21. doi:10.1088/0953-8984/21/39/395502

241. Prandini G, Marrazzo A, Castelli IE, Mounet N, Marzari N. Precision and efficiency in solid-state pseudopotential calculations. *Npj Comput Mater*. 2018; 4; 1. doi:10.1038/s41524-018-0127-2

242. Lejaeghere K, Bihlmayer G, Björkman T, et al. Reproducibility in density functional theory calculations of solids. *Science.* 2016; 351. doi:10.1126/science.aad3000

243. Perdew JP, Burke K, Ernzerhof M. Generalized gradient approximation made simple. *Phys Rev Lett.* 1996; 77; 3865-3868. doi:10.1103/PhysRevLett.77.3865

244. Perdew JP, Ruzsinszky A, Csonka GI, Vydrov OA, Scuseria GE, Constantin LA, Zhou X, Burke K. Restoring the Density-Gradient Expansion for Exchange in Solids and Surfaces. *Phys Rev Lett.* 2008; 100; 13; 136406. doi: 10.1103/physrevlett.100.136406

245. Hubbard J. Electron correlations in narrow energy bands. *Proc R Soc Lond.* 1963; A276238–257. doi: 10.1098/rspa.1963.0204

246 Allouche A. Software News and Updates Gabedit - A Graphical User Interface for Computational Chemistry Softwares. *J Comput Chem.* 2012; 32; 174-182. doi:10.1002/jcc.21759

247. Grimme S, Antony J, Ehrlich S, Krieg H. A consistent and accurate ab initio parametrization of density functional dispersion correction (DFT-D) for the 94 elements H-Pu. *J Chem Phys.* 2010; 132. doi:10.1063/1.3382344

248. Bunn CW. The crystal structure of long-chain normal paraffin hydrocarbons. The “shape” of the <CH_2 group. *Trans Faraday Soc.* 1939; 35; 482-491. doi: 10.1039/tf9393500482

249. Mikuriya M, Taniguchi K, Koyama Y, Watanabe H, Yoshioka D, Mitsuhashi R, Asato E. Crystal Structure of S_8 Molecule from Thiourea. *X-ray Struct Anal Online.* 2020; 36; 1-2. doi:10.2116/xraystruct.36.1

250. Grey IE, Bordet P, Wilson NC. Structure of the amorphous titania precursor phase of N-doped photocatalysts. *RSC Adv.* 2021; 11; 8619-8627. doi:10.1039/d0ra08886b

251. Lin C, Zhu X, Feng J, Wu C, Hu S, Peng J, Guo Y, Peng L, Zhao J, Huang J, Yang J, Xie Y. Hydrogen-incorporated TiS_2 ultrathin nanosheets with ultrahigh conductivity for stamp-transferrable electrodes. *J Am Chem Soc*. 2013; 135; 5144-5151. doi:10.1021/ja400041f

252. Dużyńska A, Judek J, Wilczyński K, Zberecki K, Łapińska A, Wróblewska A, Zdrojek M. Temperature-induced phonon behavior in titanium disulfide (TiS_2) nanosheets. *J Raman Spectrosc.* 2019; 50; 1114-1119. doi:10.1002/jrs.5637

253. Sherrell PC, Sharda K, Grotta C, Ranalli J, Sokolikova MS, Pesci FM, Palczynski P, Bemmer VL, Mattevi C. Thickness-Dependent Characterization of Chemically Exfoliated TiS_2 Nanosheets. *ACS Omega*. 2018; 3; 8655-8662. doi:10.1021/acsomega.8b00766

254. Shima T, Luo G, Hu S, Luo Y, Hou Z. Experimental and Computational Studies of Dinitrogen Activation and Hydrogenation at a Tetranuclear Titanium Imide/Hydride Framework. *J Am Chem Soc.* 2019; 141; 2713-2720. doi:10.1021/jacs.8b13341

255. Tang W, Sanville E, Henkelman G. A grid-based Bader analysis algorithm without lattice bias. *J Phys Condens Matter.* 2009; 21. doi:10.1088/0953-8984/21/8/084204

256. Henkelman G, Arnaldsson A, Jónsson H. A fast and robust algorithm for Bader decomposition of charge density. *Comput Mater Sci.* 2006; 36; 354-360. doi:10.1016/j.commatsci.2005.04.010

257. Wang Z, Jin J, Zheng Y, Zhang X, Zhu Z, Zhou Y, Cui X, Li J, Shang M, Zhao X, Liu S, Tai Q. Achieving efficient and stable perovskite solar cells in ambient air through non-halide engineering. *Adv Energy Mater.* 2021; 11; 2102169. doi:10.1002/aenm.202102169

258. Wang Y, Yang L, Shi X, Chen L, Dargusch MS, Zou J, Chen ZG. Flexible Thermoelectric Materials and Generators : Challenges and Innovations. *Adv Mater.* 2019; 31; 1807916; 1-47. doi:10.1002/adma.201807916

259. Pallecchi I, Manca N, Patil B, Pellegrino L, Marré D. Review on thermoelectric properties of transition metal dichalcogenides. *Nano Futures.* 2020; 2399-1984. doi: 10.1088/2399-1984/ab92f4

260. Guilmeau E, Bréard Y, Maignan A, Guilmeau E, Bre Y. Transport and thermoelectric properties in Copper intercalated TiS_2 chalcogenide. *Appl Phys Lett.* 2011; 99; 052107. doi:10.1063/1.3621834

261. Barbier T, Guilmeau E, Kockelmann W, Powell AV. The impact of charge transfer and structural disorder on the thermoelectric properties of cobalt intgercalated TiS_2. *J Mater Chem C.* 2016; 4; 1871-1880. doi:10.1039/C5TC04217H

262. Wang L, Zhang Z, Geng L, Yuan T, Liu Y, Guo J, Fang L, Qiu J, Wang S. Solution-printable fullerene/TiS_2 organic/inorganic hybrids for high-performance flexible n-type thermoelectrics. *Energy Environ Sci.* 2018; 11;

1307-1317. doi:10.1039/C7EE03617E

263. Dahn JR, Mckinnon WR, Haering RR, Buyers WJL, Powell BM. Structure determination of Li_xTiS_2 by neutron diffraction. *Can J Phys.* 1980; 58; 207-213. doi: 10.1139/p80-033

264. Beaumale M, Barbier T, Bréard Y, Guelou G, Powell AV, Vaqueiro P, Guilmeau E. Electron doping and phonon scattering in $Ti_{1+x}S_2$ thermoelectric compounds. *Acta Mater.* 2017; 78; 86-92. doi: 10.1016/j.actamat.2014.06.032

265. Pandey C, Ahmed G, Sharma R, Sharma Y. Ab initio study of anisotropic properties in isomorphic TiX_2 (X = S, Se, Te). *Int J Quantum Chem.* 2020; 121; e26575. doi:10.1002/qua.26575

266. Glebko N, Aleksandrova I, Tewari GC, Tripathi S, Karppinen M, Karttunen AJ. Electronic and Vibrational Properties of TiS_2, ZrS_2, and HfS_2 : Periodic Trends Studied by Dispersion-Corrected Hybrid Density Functional Methods. *J Phys Chem C.* 2018; 122; 47; 26835-26844. doi:10.1021/acs.jpcc.8b08099

267. Fang CM, De Groot RA, Haas C. Bulk and surface electronic structure of 1T-TiS_2 and 1T-$TiSe_2$. *Phys Rev B.* 1997; 56; 4455-4463. doi: 10.1103/physrevb56.4455

268. Wang H, Qiu Z, Xia W, Ming C, Han Y, Cao L, Lu J, Zhang P, Zhang S, Xu H, Sun YY. Semimetal or Semiconductor: The Nature of High Intrinsic Electrical Conductivity in TiS_2. *J Phys Chem Lett.* 2019; 10; 22; 6996-7001. doi: 10.1021/acs.jpclett.9b02710

269. Ricci M, Ambrosetti A, Silvestrelli PL. Improving the Description of Interlayer Bonding in TiS_2 by Density Functional Theory. *J Phys Chem C.* 2020; 124; 50; 27592-27603. doi:10.1021/acs.jpcc.0c09460

270. Yuhara J, Isobe N, Nishino K, Fujii Y, Chan LH, Araidai M, Nakatake M. Morphology and Electronic Structure of Sn-Intercalated TiS_2 (0001) Layers. *J Phys Chem C.* 2019; 123; 26; 22293-22298. doi:10.1021/acs.jpcc.9b05492

271. Pawula F, Daou R, Hébert S, Lebedev O, Maignan A, Subedi A, Kakefuda Y, Kawamoto N, Bada T, Mori T. Anisotropic thermal transport in magnetic intercalates Fe_xTiS_2. *Phys Rev B.* 2019; 99; 085422. doi:10.1103/PhysRevB.99.085422

272. Qian X, Gu X, Yang R. Nano Energy Thermal conductivity modeling of hybrid organic-inorganic crystals and superlattices. *Nano Energy.* 2017; 41; 394-407. doi:10.1016/j.nanoen.2017.09.047

273. Lagaly G. Intercalation of alkylamines with different types of layered compounds. *Solid State Ion.* 1986; 22; 43-51. doi: 10.1016/0167-2738(86)90057-3

274. Jeong S, Yoo D, Ahn M, Mirò P, Heine T, Cheon J. Tandem intercalation strategy for single-layer nanosheets as an effective alternative to

conventional exfoliation processes. *Nat Commun.* 2015; 6; 1-7. doi:10.1038/ncomms6763

275. Kresse G, Furthmuller J. Efficient iterative schemes for ab initio total-energy calculations using a plane-wave basis set. *Phys Rev B.* 1996; 54; 16; 11169-11186. doi: 10.1103/physrevb54.11169

276. Pack JD, Monkhorst HJ. Special points for Brillouin-zone integrations. *Phys Rev B.* 1977; 16; 4; 1748-1749. doi: 10.1103/physrevb.16.1748

277. Madsen GKH, Singh DJ. BoltzTraP. A code for calculating band-structure dependent quantities. *Comput Phys Commun.* 2006; 175; 67-71. doi: 10.1016/j.cpc.2006.03.007

278. Lucovsky G, White RM, Benda JA, Revelli JF. Infrared-Reflectance Spectra of Layered Group-IV and Group-VI Transition-Metal Dichalcogenides. *Phys Rev B.* 1973; 7; 3859—3870. doi: 10.1103/physrevb.7.3859

279. Sharma Y, Shukla S, Dwivedi S, Sharma R. Transport properties and electronic structure of intercalated compounds $MTiS_2$ (M = Cr, Mn and Fe). *Adv Mater Lett.* 2015; 6; 294-300. doi:10.5185/amlett.2015.5608

280. Guilmeau E, Maignan A, Wan C, Koumoto K. On the effects of substitution, intercalation, non-stoichiometry and block layer concept in TiS_2 based thermoelectrics. *Phys Chem Chem Phys.* 2015; 17; 24541-24555. doi:10.1039/C5CP01795E

281. Zhang RZ, Wan CL, Wang YF, Koumoto K. Titanium sulphene: two-dimensional confinement of electrons and phonons giving rise to improved thermoelectric performance. *Phys Chem Chem Phys.* 2012; 14; 45; 15641-15644. doi: 10.1039/c2p42949g

282. Mak KF, Lee C, Hone J, Shan J, Heinz TF. Atomically Thin MoS_2 : A New Direct-Gap Semiconductor. *Phys Rev. Lett.* 2010; 105; 136805. doi:10.1103/PhysRevLett.105.136805

283. Kuc A, Zibouche N, Heine T. Influence of quantum confinement on the electronic structure of the transition metal sulfide TS_2. *Phys Rev B.* 2011; 83; 245213. doi:10.1103/PhysRevB.83.245213

284. Dresselhaus BMS, Chen G, Tang MY, Yang RG, Lee H, Wang DZ, Ren ZF, Fleurial JP, Gogna P. New Directions for Low-Dimensional Thermoelectric Materials. *Adv Mater.* 2007; 19; 1043-1053. doi:10.1002/adma.200600527

285. Ursi F, Virga S, Garc G, Masciocchi N, Martorana A, Giannici F. Long-Term Stability of TiS_2 – Alkylamine Hybrid Materials. *Materials.* 2022; 15; 8297. doi: 10.3390/ma15238297

286. Koumoto K., Tian R., Yang R., Wan C. Materials Aspect of Thermoelectricity - Chapter 18: Inorganic/Organic Hybrid Superlattice Materials. 2016. doi: 10.1201/9781315197029-19

287. Bunaciu AA, Udriştioiu EG, Aboul-Enein HY. X-ray diffraction: instrumentation and applications. *Crit Rev Anal Chem.* 2015; 45; 289-99.

doi: 10.1080/10408347.2014.949616

288. Vernon-Parry K. Scanning electron microscopy: An introduction. *III-Vs Rev*. 2000; 13; 40–44. doi: 10.1016/s0961-1290(00)80006-x

289. Cardell C, Guerra I. An overview of emerging hyphenated SEM-EDX and Raman spectroscopy systems: Applications in life, environmental and materials sciences. *Trends Anal Chem.* 2016; 77; 156-166. doi:10.1016/j.trac.2015.12.001

290. Mulvaney SP, Keating CD. Raman spectroscopy. *Anal Chem.* 2000; 72; 145R-157R. doi: 10.1021/a10000155

291. Kumar CSSR. Raman Spectroscopy for Nanomaterials Characterization. Springer, Berlin Heidelberg 2012. doi: 10.1007/978-3-642-20620-7

292. Sandoval SJ. Micro-Raman spectroscopy : a powerful technique for materials research. *Microelectron J.* 2000; 31; 419-427. doi: 10.1016/s0026-2692(00)00011-2

293. Kryachko ES, Lude EV. Density functional theory: foundations reviewed. *Phys Rep.* 2014; 544; 123-239. doi:10.1016/j.physrep.2014.06.002

294. Duong DL, Burghard M, Schön JC. Ab initio computation of the transition temperature of the charge density wave transition in $TiSe_2$. *Mater Sci.* 2015; 1-29. doi: 10.48550/arXiv.1508.00823

295. Iqbal MA, Asharaf N, Shahid W, Afzal D, Idrees F, Ahmad R. Fundamentals of Density Functional Theory: Recent Developments, Challenges and Future Horizons. In: D. Glossman-Mitnik, Ed., Density Functional Theory - Recent Advances, New Perspectives and Applications. *IntechOpen*. 2022. doi:10.5772/intechopen.99019

296. Kohn W, Becke AD, Parr RG. Density Functional Theory of Electronic Structure. *J Phys Chem.* 1996; 100; 31; 12974-12980. doi:10.1021/jp960669l

297. P. Hohenberg, W. Kohn. Inhomogeneous Electron Gas. *Phys Rev.* 1964; 136; B864-B871. doi: 10.1103/PhysRev.136.B864

298. Kohn W, Sham LJ. Self-Consistent Equations Including Exchange and Correlation Effects. *Phys Rev.* 1965; 140; A1133. doi:10.1103/physrev.140.a1133

299. Woolley RG, Sutcliffe BT. Molecular structure and the born-Oppenheimer approximation. *Chem Phys Lett.* 1977; 45; 393-398. doi:10.1016/0009-2614(77)80298-4

300. Essen H. The Physics of the Born-Oppenheimer Approximation. *Int J Quantum Chem.* 1977; 12; 721-735. doi:10.1002/qua.560120410

301. Jones RO, Gunnarsson O. The Density Functional Formalism, Its Applications and Prospects. *Rev Modern Phys.* 1989; 61; 3; 689-746. doi:10.1103/RevModPhys.61.689

302. Peverati R, Truhlar DG. Improving the Accuracy of Hybrid Meta-GGA Density Functionals by Range Separation. *J Phys Chem Lett.* 2011; 2, 21, 2810-2817. doi: 10.1021/jz202170d

303. Zhang GX, Reilly AM, Tkatchenko A, Scheffler M. Performance of various density-functional approximations for cohesive properties of 64 bulk solids. *New J Phys.* 2018; 20; 063020. doi: 10.1088/i367-2630/aac7f0

304. Giannozzi P, Baseggio O, Bonfà P, Brunato D, Car R, Carnimeo I, Cavazzoni C, De Gironcoli S, Delgas P, Ruffino FF, Ferretti A, Marzari N, Timrov I, Urru A, Baroni S. Quantum ESPRESSO toward the exascale. *J Chem Phys.* 2020; 152; 154105. doi:10.1063/5.0005082

305. Yuan G, Wei Z, Lu X. A BFGS trust-region method for nonlinear equations. *Computing.* 2011; 92; 317-333. doi:10.1007/s00607-011-0146-z

306. Hafner R. Ab-Initio Simulations of Materials Using VASP : Density-Functional Theory and Beyond. *J Comput Chem.* 2008; 29; 2044-78. doi:10.1002/jcc.21057

307. Sun G, Kürti J, Rajczy P, Kertesz M, Hafner J, Kresse G. Performance of the Vienna ab initio simulation package (VASP). *J Mol Struct.* 2003; 624; 37-45. doi: 10.1016/s0166-1280(02)00733-9

308. Hafner J. Materials simulations using VASP - a quantum perspective to materials science. *Comp Phys Commun.* 2007; 177; 6-13. doi:10.1016/j.cpc.2007.02.045